EFFECTS OF Ca^{2+} AND Zr^{4+} DOPING ON THE THERMOPHYSICAL PROPERTIES OF $LaNbO_4$

By

DANIEL ROBERT LOWRY

Bachelor of Science in Materials Science and Engineering

University of Illinois Urbana-Champaign

Urbana, Illinois

2009

Submitted to the Faculty of the
Graduate College of the
Oklahoma State University
in partial fulfillment of
the requirements for
The Degree of
MASTER OF SCIENCE
December, 2015

EFFECTS OF Ca^{2+} AND Zr^{4+} DOPING ON THE THERMOPHYSICAL PROPERTIES OF $LaNbO_4$

Thesis Approved:

Dr. Pankaj Sarin

Thesis Adviser

Dr. Raj N. Singh

Dr. James E. Smay

ACKNOWLEDGEMENTS

It is my pleasure to thank everyone who has helped make this thesis possible. My deepest thanks to my parents for everything they have given and fostering in me a drive to learn, improve, and succeed, and my sister for always challenging me as only a sibling can. To the Jons Pipe shop family a special appreciation for the endless encouragement to continue learning. My sincere gratitude to Dr. Waltraud Kriven and her research group at the University of Illinois for the opportunity to share their beamtime at NSLS and produce the data key to this thesis. I would like to thank my advisor Dr. Pankaj Sarin for his guidance in my time at Oklahoma State University. With his guidance, I was able to define this study and make it my own. Lastly, I would like to thank my committee members, Dr. Raj N. Singh, and Dr. James E. Smay for their guidance and feedback.

I would like to acknowledge the national laboratory facilities used in the completion of this thesis, NSLS at Brookhaven National Lab and APS at Argonne National Lab. Use of the National Synchrotron Light Source, Brookhaven National Laboratory, was supported by the U.S. Department of Energy, Office of Science, Office of Basic Energy Sciences, under Contract No. DE-AC02-98CH10886. Use of the Advanced Photon Source was supported by the U. S. Department of Energy, Office of Science, Office of Basic Energy Sciences, under Contract No. DE-AC02-06CH11357.

Name: Daniel Robert Lowry

Date of Degree: December, 2015

Title of Study: EFFECTS OF Ca^{2+} AND Zr^{4+} DOPING ON THE THERMOPHYSICAL PROPERTIES OF $LaNbO_4$

Major Field: Materials Science and Engineering

Abstract: Lanthanum Niobate ($LaNbO_4$) doped with acceptor ions, specifically calcium (Ca^{2+}) is a potential material for proton conducting solid oxide fuel cells (PC-SOFCs). The proton conductivity of this material has been studied with promising results. Optimal proton conductivity in $LaNbO_4$ for PC-SOFC applications is in the high temperature tetragonal phase (*t*-$LaNbO_4$), which transforms to a monoclinic structure (*m*-$LaNbO_4$) on cooling below ~500°C. The large change in coefficient of thermal expansion (CTE) between the high and low temperature phases of $LaNbO_4$, however, is a key limitation in processing dense microstructures of electrolyte membranes. As the CTE for *t*-$LaNbO_4$ is approximately half of that for *m*-$LaNbO_4$ the selection of interconnect materials for PC-SOFCs is a challenge. This study seeks to understand how doping $LaNbO_4$ with aliovalent ions influences the CTE and the phase transformation temperature. Part one of this study was focused on understanding how Ca^{2+} doping alters the evolution of the CTE. Part two of this study explores the inclusion of Zr^{4+} in the structure to decrease the transformation temperature from monoclinic to tetragonal phase. High temperature x-ray diffraction (HTXRD) was used to understand how these dopants influence the crystal structure, the phase transformation temperature, and the thermal expansion behavior of $LaNbO_4$.

TABLE OF CONTENTS

LIST OF TABLES

LIST OF FIGURES

CHAPTER 1.

LITERATURE REVIEW

Proton conducting solid oxide fuel cells (PC-SOFCs) are of particular interest for energy generation using hydrocarbon fuels. PC-SOFCs offer some distinct advantages when compared with oxide ion conducting SOFCs, which include (a) potential for lowering the operation temperatures, as proton conduction in oxides generally has lower activation energy than oxygen ion conduction; (b) higher CH_4 conversion because of direct proton (hydrogen) removal at the anode; (c) higher carbon coking resistance because of unfavorable Boudouard Reaction[1]; and (d) no dilution of fuel with moisture as water is formed at the cathode.[2, 3, 4] Perovskite-type cerates and zirconates of barium (Ba) have been extensively researched as proton conducting oxides.[5, 6, 7, 8, 9, 10, 11, 12] The main drawback in the use of barium cerates is poor chemical stability and formation of electronic species under reducing conditions.[12] The chemical stability of doped barium zirconates is far greater.[13, 14, 15] Although there is high intrinsic proton mobility in $BaZrO_3$, which is cubic at room temperature,[16, 17] the conductivity of polycrystalline

---

[1] Boudard Reaction: the reduction of carbon dioxide by hot carbon,[1] $CO_2 + C \rightarrow 2CO$.

samples is often significantly lower than the bulk because of large grain boundary resistance.

Acceptor-doped rare-earth orthoniobates and orthotantalates of general formula $RE_{1-x}A_xMO_4$ (where RE = La, Gd, Nd, Tb, Er or Y; M = Nb or Ta; A = Ca, Sr or Ba; and x = 0.01–0.05) have been evaluated for their proton conducting properties.[18] Of the compositions investigated so far, $La_{0.99}Ca_{0.01}NbO_{4-\delta}$ has been reported to have the highest conductivity.[19, 20, 21, 22] In general, La-containing niobates have higher proton mobilities than other RE-containing phases, consistent with their larger lattice volumes. Conductivity values measured for optimally doped niobates are of the order of 10^{-3} S cm^{-1} at 950°C,[23] and suggest that a fuel cell containing a few microns thick electrolyte layer may achieve reasonable area-specific power densities.[18] Fabrication and stability of such thin but dense electrolyte layers of $LaNbO_4$ have their associated challenges, and require a deeper understanding of the thermo-physical properties

1.1 Polymorphism in rare-earth niobates

The rare-earth niobates ($LnNbO_4$, Ln = La–Lu, and Y) are known to undergo a reversible, pure ferroelastic phase transition from a high-temperature paraelastic, scheelite-type (tetragonal, I41/a) to a ferroelastic, fergusonite-type (monoclinic, I2/a) structure at low temperatures.[24, 25, 26, 27, 28, 29, 30] During the transformation which, is known to occur at approximately 500° C, [31, 32, 33] the tetragonal *a* axis becomes the monoclinic *a*, the tetragonal *b* becomes the monoclinic *c*, and the tetragonal *c* becomes the monoclinic *b*, this is shown in Figure 1-1. Atomic position for the atoms in both the monoclinic, space group I2/a and ICSD#20406, and tetragonal, space group I4/a and ICSD#37138, phases of $LaNbO_4$ are presented in Figure 1-2 The ferroelastic phase is essentially a monoclinically distorted, scheelite-like structure.[26, 29] The second order transformation is described by a series of successive states which are energetically favorable to the previous state and progresses without a nucleation event.[34] The monoclinic distortion is progressively reduced with increasing temperature and the structure reversibly transforms into the paraelastic tetragonal structure with no volume change at transformation.[26, 29] This is unlike the case with zirconia which experiences a significant increase in volume at transformation, 4-5% when cooling from the tetragonal to the monoclinic phase.[35, 36] With no discontinuity in volume change at transformation it is likely that a thin film of $LaNbO_4$ will maintain structural integrity. The structural phase transition however, induces a lattice distortion which produces considerable macroscopic spontaneous strains (ε^s). In ferroelastic materials, spontaneous strains are typically in the range of 0.1%–3.0%. $LaNbO_4$ was reported to have a large room temperature spontaneous strain of 7.06% associated with the phase transition when no external force fields are applied.[31, 37] This large strain is a concern for the processing of thin films necessary for the electrolyte membrane of the PC-SOFC device. Tailoring the crystal structure through the use of dopants is an area of interest in order to decrease the lattice distortion so that at low temperatures the monoclinic structure is less strained, one way to achieve this would be to stabilize the tetragonal phase at low temperature.

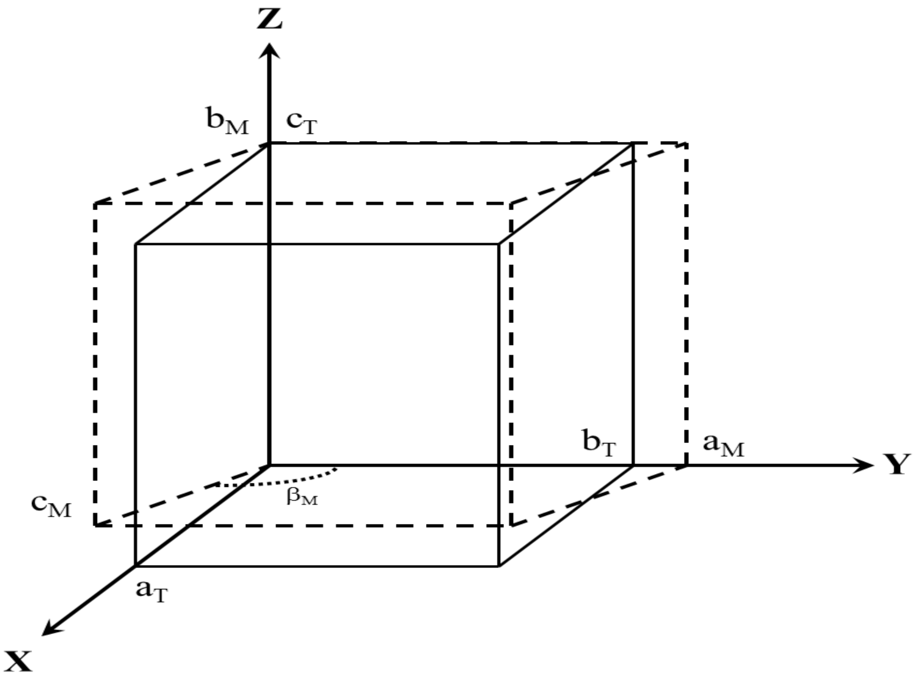

Figure 1-1: Lattice parameter relationship between the high temperature tetragonal phase (solid) and the low temperature monoclinic phase (dashed) of $LaNbO_4$.[31]

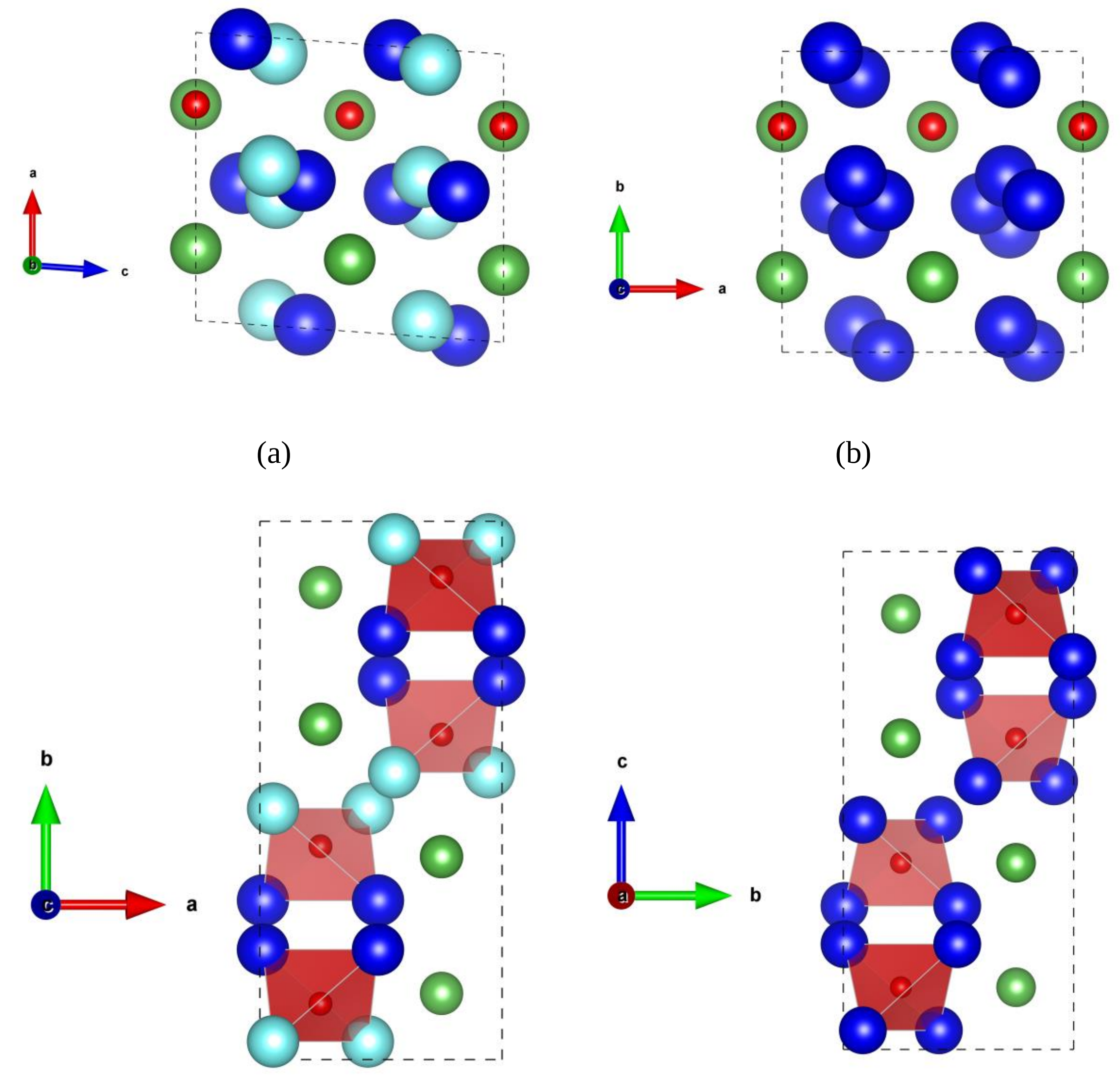

(a) (b)

(c) (d)

Figure 1-2: Unit cells for *m*-$LaNbO_4$ (a and c), and *t*-$LaNbO_4$ (b and d), tetragonal structure stable above 500°C.[38] The spheres represent the atomic species as such; green is La^{3+}, red is Nb^{5+}, and the two shades of blues are O^{2-}. In *m*-$LaNbO_4$ the two shades of blue represent energetically different O^{2-}. Figures c and d display the NbO_4 tetrahedra.[39]

1.2 Proton conductivity in rare-earth niobates

Proton conduction in $LaNbO_4$ is facilitated by creation of oxygen vacancy point defects by substitution of an acceptor dopant, such as Ca^{2+}, on the lanthanum site equation (1.1).

$$2CaO + Nb_2O_5 = 2Ca_{La}' + 2Nb_{Nb}^{x} + V_O^{\cdot\cdot} + 7O_O^{x} \tag{1.1}$$

These oxygen vacancies have been found to be independent of temperature and the ambient partial pressure of oxygen when the dopant concentration is below the solubility limits for the crystal. Proton conductivity in $LaNbO_4$ improves with increase in the acceptor dopant concentration.[23] $LaNbO_4$ compositions containing calcium as a dopant-cation represent the highest conductivity in oxides without barium or strontium. This makes $LaNbO_4$ an interesting candidate for use in CO_2 containing atomspheres.[18, 23]

Operation conditions for $LaNbO_4$ devices dictate how well they will operate. Proton conductivity in the rare earth niobates, as a function of temperature, is very similar to what has been observed in oxides and phosphates that have been acceptor doped.[9, 40, 41, 42] However, the rare earth niobates have an advantage over the phosphates for proton conduction. As the radius of the rare earth cation increases the hydration enthalpy decreases in the niobates while it increases in the phosphates.[43] At high temperatures in oxidizing environments this material is a p-type semiconductor with increasing total conductivity as the partial pressure of oxygen is increased.[23] However, in highly reducing atmospheres, which is the target environment for PC-SOFCs and at temperatures below 1100°C the conductivity is dominated by protons, see Figure 1-3, making the material an n-type semiconductor.[23, 42] In the wet atmospheres, i.e. under higher water vapor pressure, the created oxygen vacancies become hydroxide defects by hydration. When this occurs the electro neutrality condition can be approximated by equation (1.2).[23, 42]

$$2[V_O^{\cdot\cdot}] + [OH_O^{\cdot}] = [Ca'_{La}] \tag{1.2}$$

In addition to the promise for sufficient proton conductivity, $LaNbO_4$ also has the lowest transformation temperature amongst all rare earth orthoniobates.[30] This is due to lanthanum having the largest ionic radii of the rare earth elements and with the large ionic radius which decreases lattice energy thus decreasing the transformation temperature. Additionally, it has been shown that proton conductivity decreases as the radius of the rare earth cation increases, see Figure 1-4.[18] This observation in addition to the lowest transformation temperature makes $LaNbO_4$ a very interesting candidate for proton conducting applications.

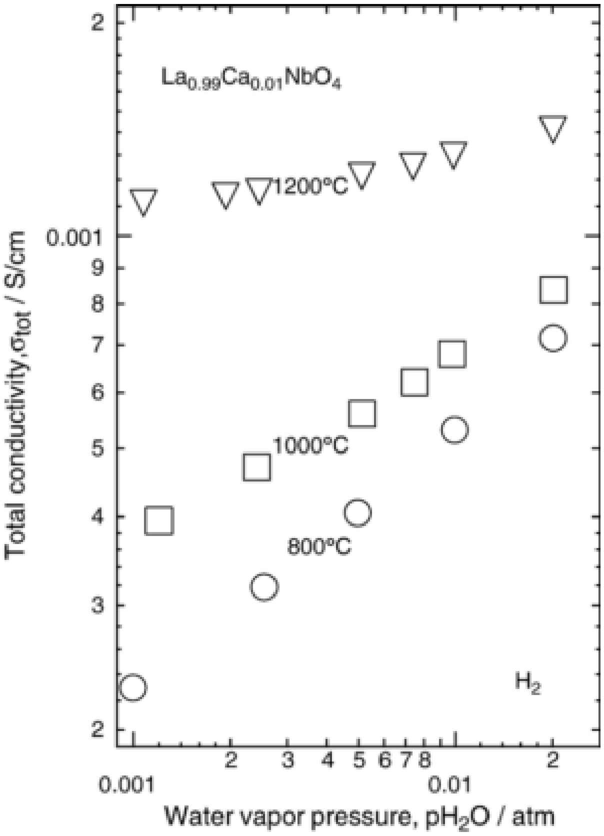

Figure 1-3: Total conductivity of 1% Ca^{2+} doped $LaNbO_4$ as a function of the partial pressure of H_2 with essentially constant oxygen pressure.[23]

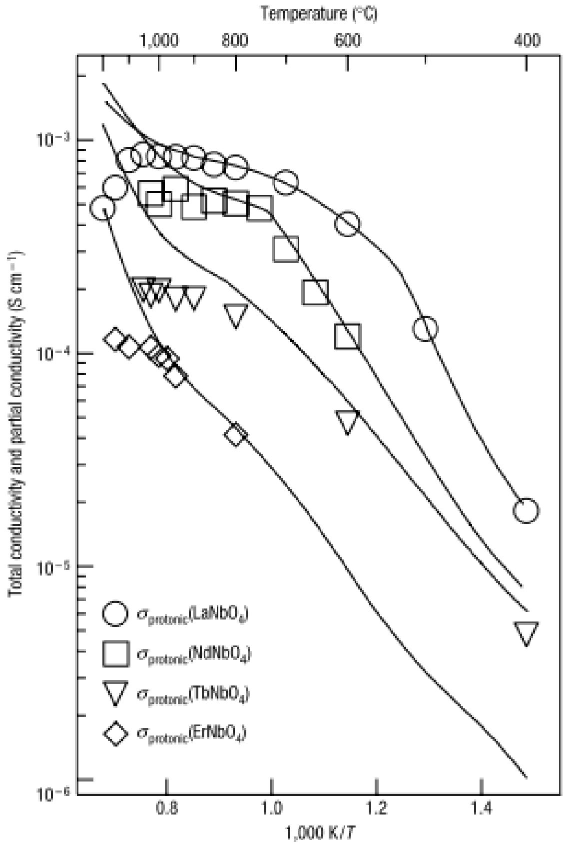

Figure 1-4: Total a.c. conductivity for $RENbO_4$ doped with 1% Ca^{2+} as measured in wet H_2 atmosphere.[18]

While both the monoclinic and tetragonal phases of $LaNbO_4$ have been shown to be proton conducting, the higher activation energy of the monoclinic phase is undesirable.[18, 23] Decreasing the operation temperatures of fuel cell devices to intermediate temperatures (250°C to 550°C) is an active area of research which promises increased device lifetimes and reduced manufacturing and operating costs.[44, 45] One possible route to achieving this objective in $LaNbO_4$ based PC-SOFC devices is by stabilizing the parent tetragonal crystal phase to lower temperatures. This hypothesis is consistent with decreased proton conductivity observed in orthorhombic strontium cerate ($SrCeO_3$) when compared to the cubic structure.[46] Energetically different oxygen sites in the orthorhombic structure of $SrCeO_3$ present an uneven energy hypersurface for proton transport, as well as bias rotational diffusion, resulting in an increase in activation energy for proton transfer.[46] In the case of rare-earth orthoniobates and tantalates, the scheelite-type (or tetragonal) phase has significantly lower activation energy for proton migration (0.52 – 0.62 eV) than the fergusonite-type (monoclinic) phase.[18, 23] A lower transformation temperature will also facilitate processing of stable and dense thin films by minimizing spontaneous strains that often result in twinned microstructures. In general, the phase transformation temperature (T_{tr}) increases with decreasing rare-earth cation size (and consequently unit cell volume) within the temperature range 500–830°C for the rare-earth niobates and is considerably higher for the isostructural tantalates (1300–1450°C).[30] Shian *et al.* have reported that doping $YTaO_4$ with up to 20 mol% of Zr^{4+}resulted in a decrease in the T_{tr}, from approximately 1426°C to about 821°C, as a linear function of dopant concentration, Figure 1-5.[47]

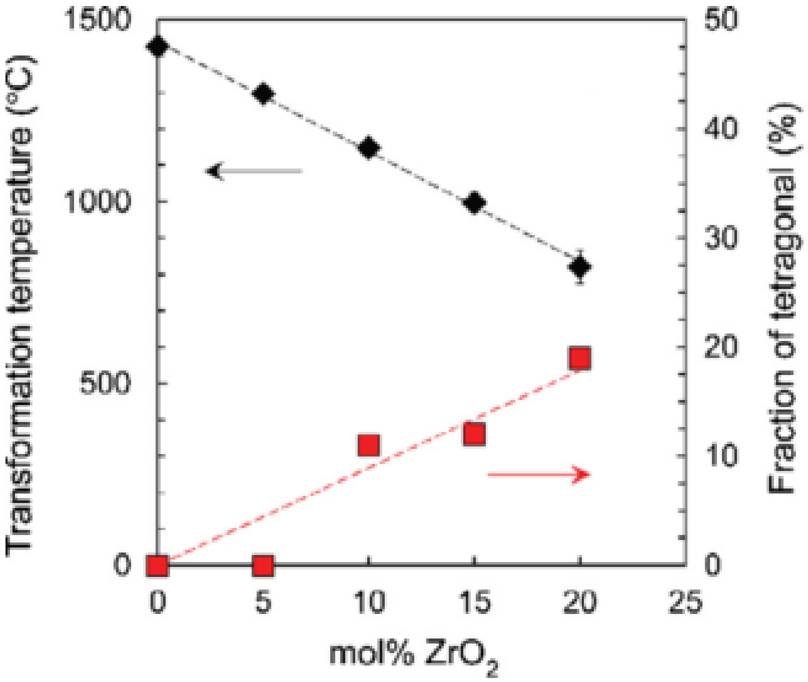

Figure 1-5: Decrease in *m*- to *t*-$YTaO_4$ transformation temperature as a function of Zr^{4+} dopant concentration.[47]

In addition to lowering the phase transformation temperature as a means to improve $LaNbO_4$ for proton conducting applications, it is also desirable to attain the optimal oxygen to oxygen distance. This optimal distance has been identified as approximately 2.5 Å, as determined by the oxygen to hydrogen bond being 1 Å in length and the distance to the next nearest oxygen position to the hydrogen being 1.5 Å.[19] The creation of oxygen defects occurs across neighboring NbO_4 tetrahedra.[40, 41] Additionally, in the tetragonal phase all the oxygen positions are energetically equivalent whereas in the monoclinic phase there are two energetic oxygen positions which decreases the conductivity efficiency, this is shown in Figure 1-6. Fjeld (2010) reported the preferred proton sites in both the tetragonal and monoclinic phase as determined by the site energy.

In *t*-LaNbO$_4$ the ‘a’ site is preferential to the ‘b’ as the site energy is 0.13 eV lower, see Figure 1-6(a). Due to the two positions in *m*-LaNbO$_4$, denoted by the red and blue boxes in Figure 1-6(b), there is an additional conductivity site. For monoclinic the possible sites as denoted by a′, b′, and c′ with the b′ site having an energy 0.41 eV higher than a′, and the c′ site having energy 0.77 eV greater than the a′ site. As the site energy increases the activation energy for proton conduction also increases, therefore the lower the energy the more preferred that path is for conduction. The mechanism for transport of the proton defect has a principal feature of rotational diffusion towards a neighboring oxide ion, this is shown for BaCeO$_3$ in Figure 1-7. [3]

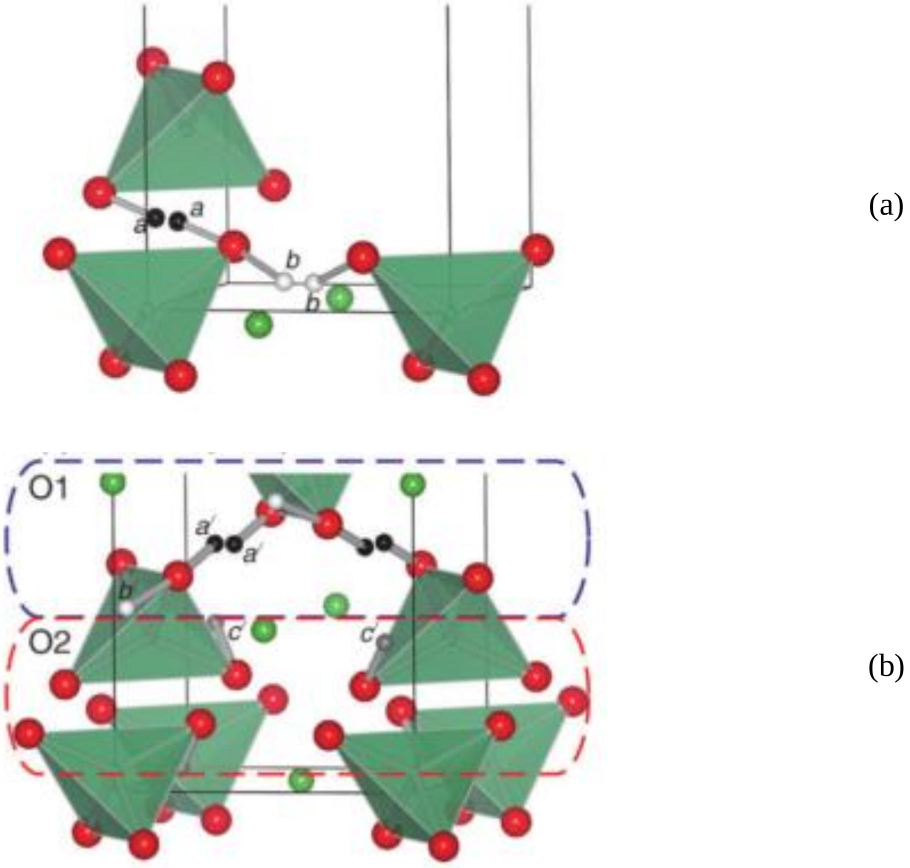

Figure 1-6: Calculated stable sites for a proton in (a) *t*-LaNbO$_4$ and (b) *m*-LaNbO$_4$. Black, white, and grey spheres represent proton positions in each phase.[19]

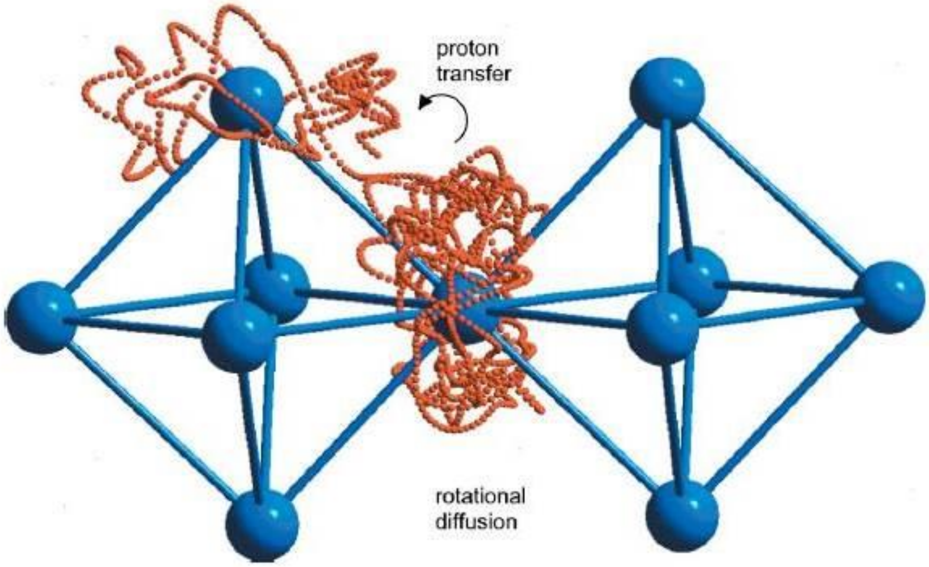

Figure 1-7: Proton transfer path model around oxygen atoms in $BaCeO_3$ showing rotational diffusion and proton transfer.[3]

To produce a PC-SOFC using acceptor doped $LaNbO_4$ presents its own challenges. Since $LaNbO_4$ is a line compound with small changes in composition producing phases with different stoichiometry and crystal structure, Figure 1-8. When the La^{3+} to Nb^{5+} ratio deviates from 1 then either the La_3NbO_7 or $LaNb_3O_9$ phases will be present. Of these the La_3NbO_7 phase has similar conductivity properties to $LaNbO_4$, while the Nb^{5+} rich phase has much higher electronic conductivity.[42, 48, 49] Based on the proton conductivity values achieved with this material the membrane thickness required to produce acceptable power density must be on the micron scale.[23] To produce these thin membranes the grain boundaries need to be minimized as they decrease conductivity.[42]

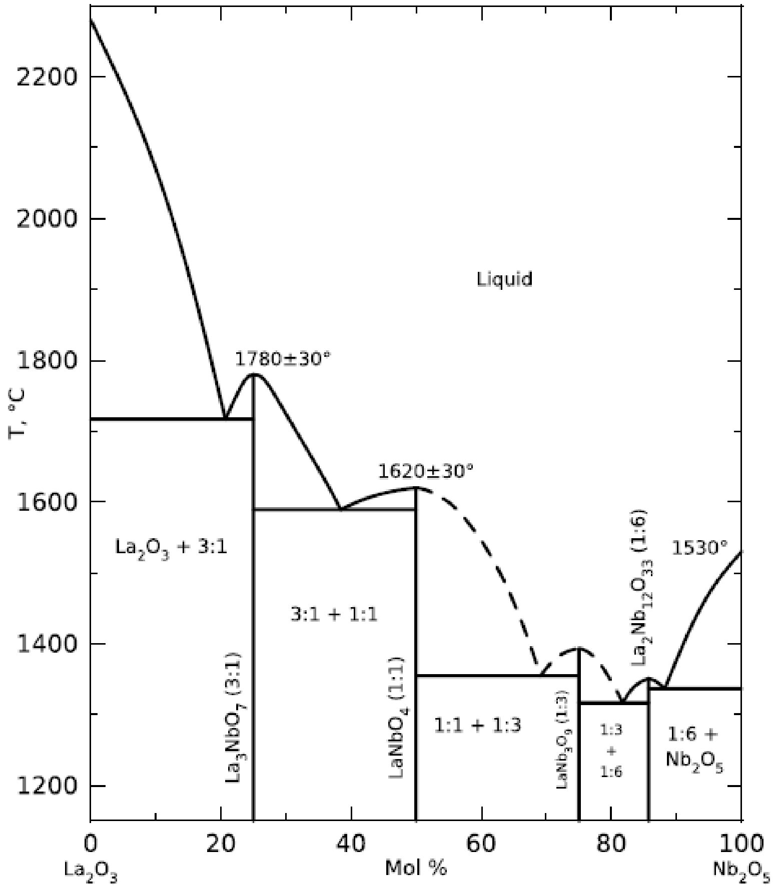

Figure 1-8: Phase diagram for La_2O_3 and Nb_2O_5.[50]

Another issue to consider in the production of PC-SOFCs using $LaNbO_4$ membranes is the change in coefficient of thermal expansion (CTE) between the monoclinic and tetragonal phases. The CTE for *m*-$LaNbO_4$ has been reported as being approximately $17.7x10^{-6}$ /K while the tetragonal CTE is approximately half of that, $7.8x10^{-6}$ /K, at the phase transformation.[33, 51, 52] The large change in CTE has made the identification of suitable interconnects difficult and as such is an interesting problem to address. However, an area of interest with these materials is still the thermal expansion behavior. Furthermore, due to low symmetry of the monoclinic phase the thermal expansion in the phase is highly anisotropic leading to concerns for the microstructure as neighboring grains are not likely to be aligned thus as they expand with temperature stress would be introduced into the microstructure. However, in the tetragonal phase this is less of a concern as the increased symmetry in the crystal corresponds to a significant decrease in anisotropy, ~95% decrease in anisotropy at transformation as determined in this study. Understanding the thermal expansion of $LaNbO_4$ and being able to tailor this through the addition of dopants is important for the selection of electrode materials for fuel cells.[42]

CHAPTER 2.

OBJECTIVES

The goal of this study is to investigate how specific dopants alter the thermophysical properties of $LaNbO_4$. Acceptor doping of this material has been shown to improve the proton conductivity properties, which is important for device efficiency, yet the effects of these dopants on the crystallographic properties are not well understood presently. The approach taken in this two part study was to first understand how Ca^{2+} dopants influence the thermal expansion behavior of $LaNbO_4$, and second to determine if the phase transformation temperature could be modified by Zr^{4+} doping similar to what has been shown for the $YTaO_4$ system. Synthesized powders of $LaNbO_4$ compositions with varied dopant concentrations, were first characterized for their composition, morphology, and thermodynamic stability, and subsequently studied by in situ HTXRD to elucidate corresponding crystal structure and changes occurring at high temperatures. Accordingly, the objectives of this research are:

Objective 1: Understand the effect of Ca^{2+} on the phase transformation and thermal expansion properties of $LaNbO_4$

The most promising conductivity for acceptor doped $LaNbO_4$ has been shown for 1 mol% Ca^{2+} doping. Improved understanding of the thermal expansion properties and associated anisotropy is important to guide the development of thin dense membranes for any PC-SOFC device based on these material systems.

Objective 2: Explore the addition of Zr^{4+} to lower the temperature for the tetragonal to monoclinic phase transformation in $LaNbO_4$

The primary focus was on evaluating the influence of dopant ion concentration on the crystal structure and phase transformation characteristics of $LaNbO_4$. In addition, any change in thermal expansion property and anisotropy was also examined.

CHAPTER 3.

MATERIALS AND METHODS

3.1 Synthesis

Powders of the compositions to be studied were produced using the stearic entrapment method of synthesis.[53] This method of synthesis has been shown to produce homogeneous single phase mixed oxide ceramic powders of precise composition due to the atomic level mixing of the precursors. For these studies commercially available precursors were sourced from Sigma Aldrich (St. Louis, MO, USA). The precursors used were niobium(V) chloride ($NbCl_5$), lanthanum(III) nitrate hexahydrate ($La(NO_3)_3 \cdot 6H_2O$), calcium(II) nitrate tetrahydrate ($Ca(NO_3)_2 \cdot 4H_2O$), barium(II) nitrate ($Ba(NO_3)_2$), strontium(II) nitrate ($Sr(NO_3)_2$), zirconium(IV) oxynitrate hydrate ($ZrO(NO_3)_2 \cdot xH_2O$), and polyethylene glycol (PEG, Mn=300). The hydration of $ZrO(NO_3)_2 \cdot xH_2O$ was determined by thermogravimetric analysis (TGA) using a STA449 F1 Jupiter (Netzsch Instruments, Selb, Germany) by heating a known quantity of the precursor to 1500°C to fully convert to zirconium dioxide (ZrO_2). Taking the one to one mole ratio of ZrO_2 to the precursor $ZrO(NO_3)_2 \cdot xH_2O$ it was possible to determine the precise moles of hydration.

The strength of using the stearic entrapment method of synthesis is that the precursor materials are homogenously mixed into solution using ethanol as the solvent. Once the stoichiometric amount of each precursor was dissolved in ethanol PEG was added to the solution using a cation valence charge to monomer molar ratio of 4 to determine the amount of organic needed. The organic component serves to act as a molecular net to catch and evenly distribute the cations. After the addition of PEG, the solution was mixed at ambient temperature for at least one hour, following which the solution was heated while constantly stirring until the ethanol had evaporated. At this point the entire vessel was placed in a drying oven at 120°C for 10 hours to remove any residual ethanol. Following the overnight drying the crust was ground using an agate mortar and pestle to a fine powder. Finally, the ground powder was calcined in alumina crucibles at 1200°C for 3 hours using a Carbolite calcination furnace (Carbolite Limited, Hope, UK) to produce the desired oxide powders. The calcined powders were reground and sieved through a -325 mesh sieve in order to use only powders with a particle size less than 45 μm for characterization and analysis.

3.2 Characterization

3.2.1 DSC/TGA/C_P

Produced powders were characterized with a STA449 F1 Jupiter to verify the removal of all organic and volatile phases during the calcination step as well as to confirm any detectable phase transformation events. These measurements were completed using Al_2O_3 crucibles (AdValue Technology, Tucson, AZ) and a heating rate of 10°C per minute to 1500°C and cooling back to room temperature at the same rate in a silicon carbide furnace. The sample was heated in air using a flow rate of 70 cm^3/minute to ensure the removal of any volatile compounds from the furnace.

Specific heat measurements were also conducted on the synthesized powders. For these measurements the sample was heated from 50°C to 800°C and cooled back to 100°C at a rate of 20°C/min. This procedure was repeated twice and the sample was held isothermally for 20 minutes between each heating and cooling segment. For specific heat analysis, datasets were acquired using platinum crucibles and a platinum furnace. Prior to analysis of the ceramic powders, a baseline and a standard run were established using the same parameters. the standard run was completed using a sapphire disk supplied with the instrument. The experimental measurements used a disk of the ceramic powder pressed uniaxially with a 20-ton hydraulic press (Carver, Inc., Wabash, IN) to similar thickness as the sapphire standard. The sample pellets were not heat treated prior to testing.

3.2.2 (HT)XRD

The XRD (Bruker AXS D8 Discover, Madison, WI) was used to verify the crystalline phase composition of the powders. The diffractometer is equipped with a curved crystal monochromator and Cu K_α radiation (λ = 1.54Å) source. The diffraction data was collected over a 2θ range of 15° to 85° with a step size of 0.01° using a GADDS area detector. Each scan consisted of 7 frames with a 50% overlap between frames to maximize resolution; each frame was collected for 180 seconds.

High temperature in situ powder diffraction datasets were collected at beamline X14A at the National Synchrotron Light Source (NSLS) at Brookhaven National Laboratory (Upton, NY). These measurements were made using a quadrupole lamp furnace[54] (QLF), Figure 3-1 to Figure 3-3, and x-rays of wavelength λ = 0.7796 Å. High resolution XRD datasets were collected over a 2θ range of 5° to 45° using a silicon strip position detector. Quartz capillaries (Charles Supper Company, Inc., Natick, MA) were used to load samples of ceramic powder that had been ground to less than 44µm and mixed with approximately 15 weight percent platinum powder (Sigma-Aldrich, St. Louis, MO). The loaded capillaries were then set in an Al_2O_3 tube which was mounted on the goniometer and positioned in the QLF hot zone. Samples were heated from 20°C to 1050°C (set-point) with 2 minute holds prior to pattern acquisition to allow for thermal acquisition. The samples were rotated at 60 rpm during diffraction data collection

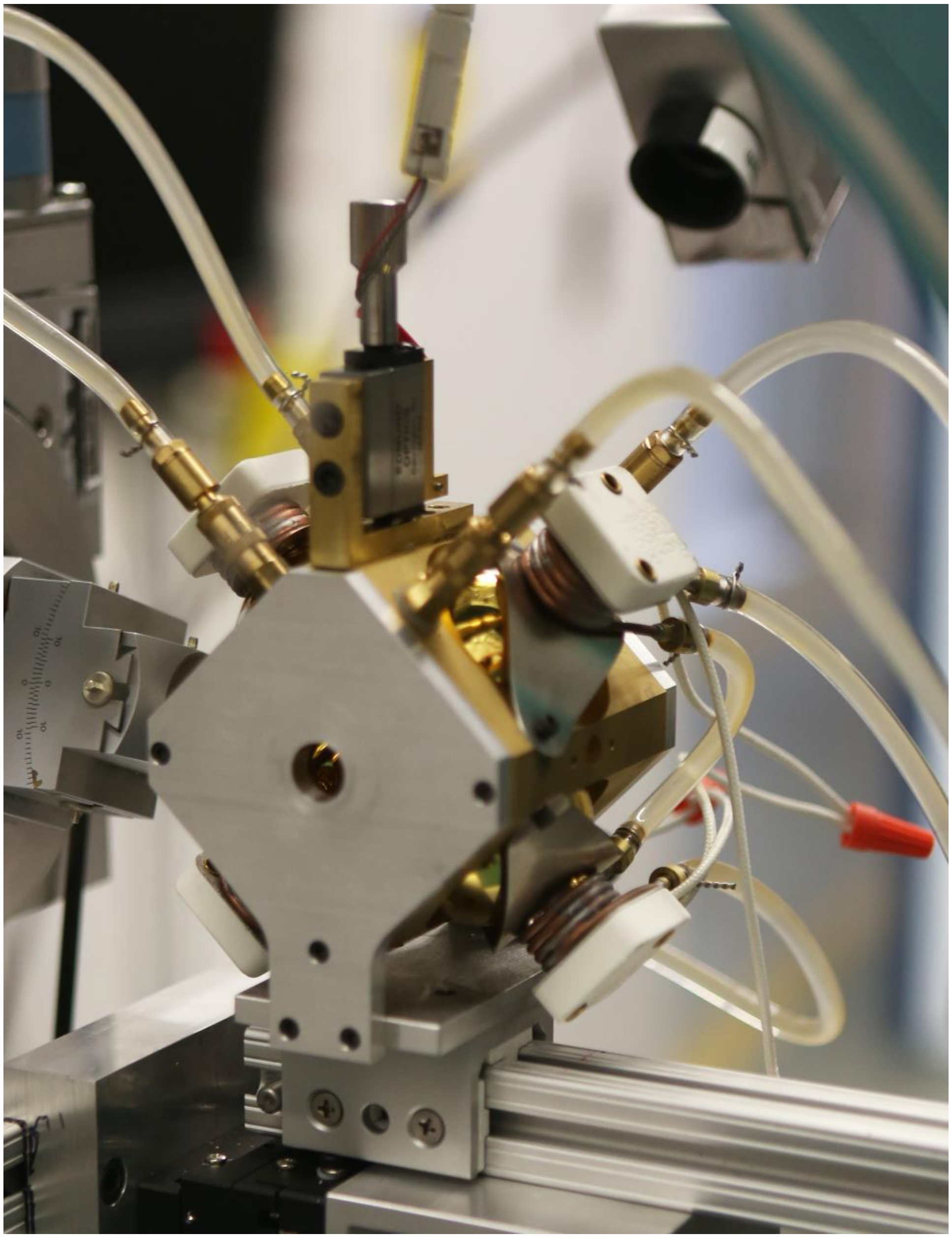

Figure 3-1: QLF mounted on diffractometer at 33-BM-C, Advanced Photon Source, Argonne National Laboratory. Picture taken from beam side of furnace with the detector in the background.

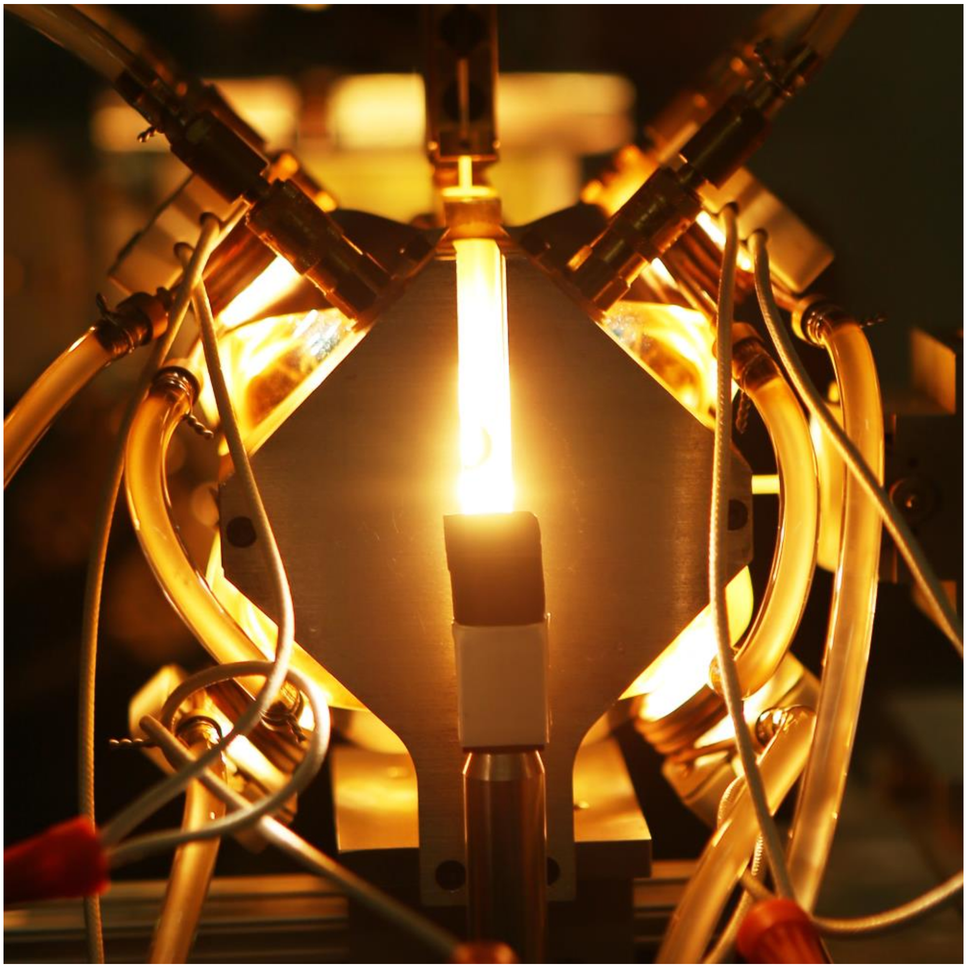

Figure 3-2: QLF in operation at 1200°C.

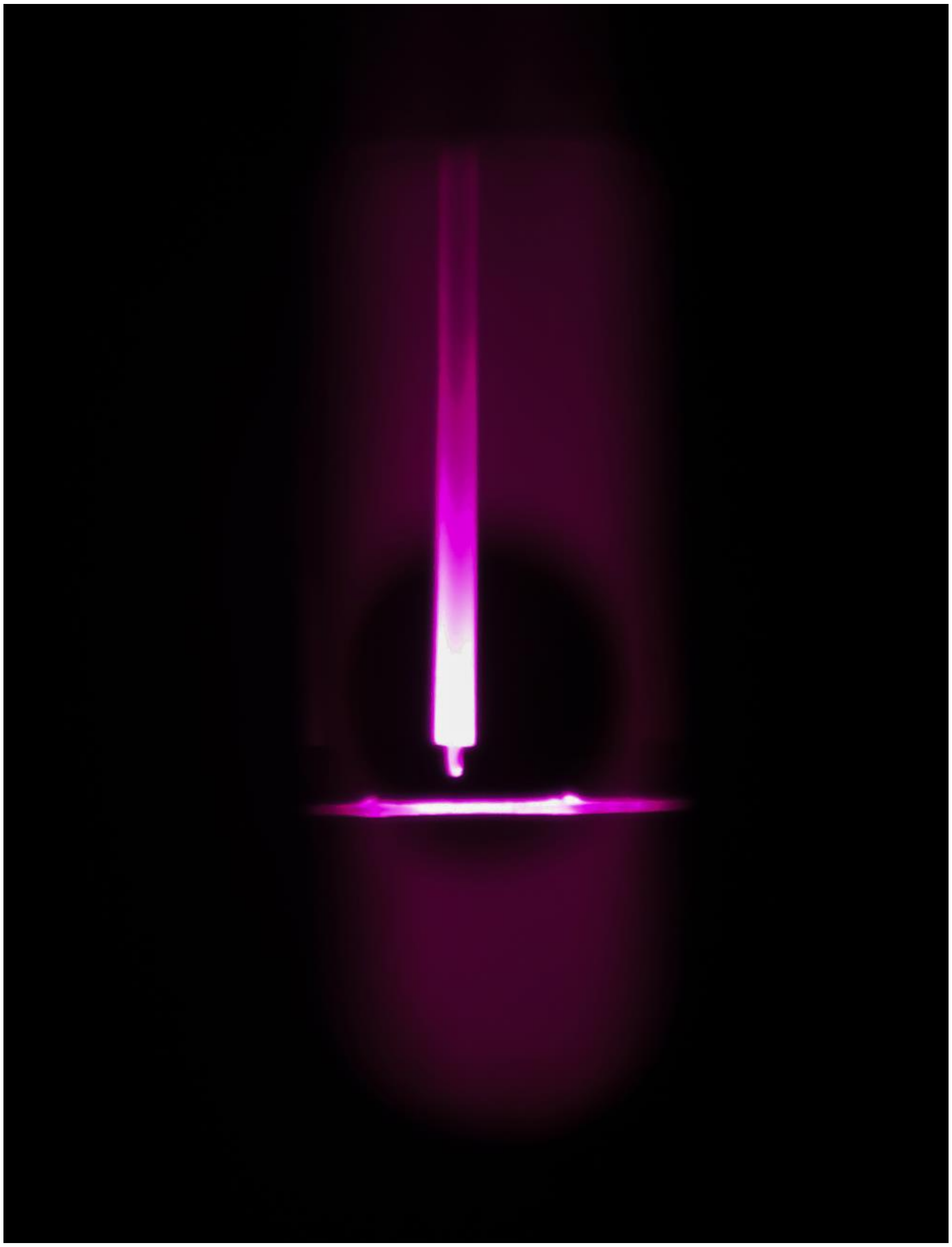

Figure 3-3: Typical powder diffraction sample used with the QLF, quartz capillary is loaded with powder, inserted horizontally inside the furnace, and rotated during XRD data collection.

3.2.3 SEM/EDS

A Hitachi S-4800 field emission scanning electron microscope (FE-SEM) coupled with an Oxford Instruments (Tubney Woods, Abingdon, Oxon, UK) energy dispersive spectroscopy (EDS) silicon drift detector was used to determine the elemental composition and distribution in the microstructure. EDS analysis was completed using the AZtec software package with internal calibrations. Elemental maps were acquired using an accelerating voltage of 30 keV at a working distance of 15mm. Samples for EDS were prepared by uniaxial pressing of the powder into a pellet followed by sintering at 1150°C for 5 hours, this did not produce fully dense samples but was satisfactory for the intended analysis.

3.3 Analytical methods

3.3.1 Rietveld Refinements

The Rietveld method was used to refine unit cell lattice parameters for each composition from the HTXRD datasets.[55] Refinement of the collected HTXRD datasets, Figure 3-4, was completed using GSAS[56] with EXPGUI[57] and Jade 2010 (MDI Inc., Livermore CA). The Rietveld refinement method allows for the determination of a specific phase's properties in the material regardless of the presence of any secondary phases in the studied sample. Quantitative results of interest from the refinements for this study included unit cell parameters, and the evolution of planar d-spacing as a function of temperature for use in the analysis of thermal expansion behavior. The refinement of the powder diffraction data was also used to quantify the amount of phases present in the material other than the expected $LaNbO_4$ and Pt. This was especially useful in the zirconium doped series to determine the amount of zirconium in the structure based on the phase fraction of zirconia (ZrO_2) determined by whole pattern fitting.

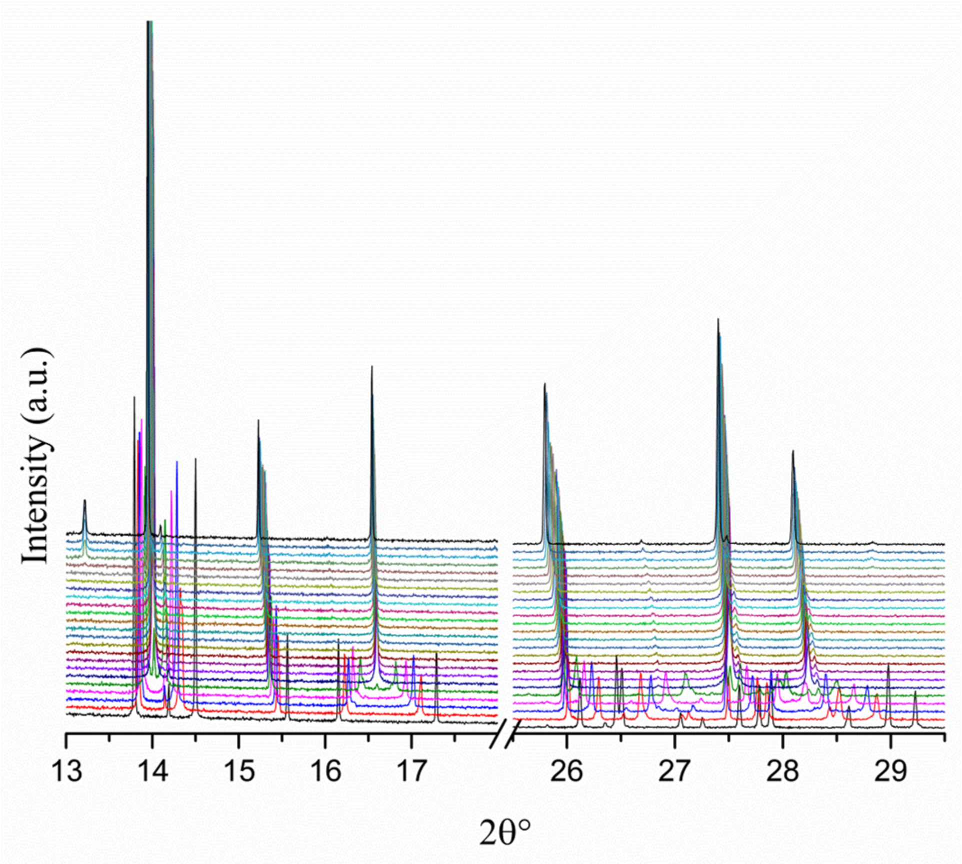

Figure 3-4: In situ HTXRD dataset collected for $LaNbO_4$ demonstrating the convergence of peaks in the monoclinic phase to the tetragonal phase, sample temperature increasing from 30°C (bottom) to 1095°C (top).

Wavelength of the synchrotron radiation was determined through refinement of LaB_6 standard powder (SRM660a) collected at room temperature at the beginning and end of the experiment. The LaB_6 powder was from the National Institute of Standards and Technology (NIST, Gaithersburg, MD) and has known lattice parameter, a_{LaB_6}= 4.1569 Å. Using GSAS we are able to determine the precise wavelength used at the beamline facility, for this study the wavelength was λ = 0.7796 Å. Refinement of the included platinum powder for the high temperature datasets is completed in order to determine the sample temperature for each collection. The platinum serves as an internal thermocouple and the change in the lattice parameter, due to thermal expansion, is used to determine the sample temperature.[58]

3.3.2 Spontaneous Strain

Spontaneous strain is a construct of the lattice strain in the low temperature phase with respect to the parent phase, the parent phase is assumed to be strain free throughout the temperature range.[59] In order to determine this we treat determine the strain tensor values from the refined lattice parameters keeping in mind that the strain tensor, which is second rank, of the monoclinic system for the orientation states S_1 and S_2 are:

$$\varepsilon(S_1) = \begin{pmatrix} e_{11} & e_{12} & 0 \\ e_{21} & e_{22} & 0 \\ 0 & 0 & e_{33} \end{pmatrix} \tag{3.1}$$

$$\varepsilon(S_2) = R\varepsilon(S_2)R^T \tag{3.2}$$

where, R and R^T are the 90° rotation matrix and the corresponding transpose matrix. Strain tensor components are calculated from the monoclinic unit cell parameters and the extrapolated tetragonal unit cell parameters. These extrapolated values are determined by applying a linear fit to the tetragonal unit cell parameters, and calculating what the tetragonal unit cell parameters would be in the temperature range where only the monoclinic phase is present. The strain tensor values in terms of the unit cell parameters given as:[60]

$$e_{11} = \frac{c_M \sin\beta_M^*}{a_T} - 1 \tag{3.3}$$

$$e_{22} = \frac{a_M}{b_T} - 1 \tag{3.4}$$

$$e_{33} = \frac{b_M}{c_T} - 1 \tag{3.5}$$

$$e_{12} = e_{21} = -\frac{1}{2}\left[\frac{c_M cos\beta_M^*}{a_T}\right] \tag{3.6}$$

where, β_M^* is the beta angle in reciprocal space. As stated before a_M, b_M, and c_M are the unit cell parameters for the monoclinic phase, and a_T, b_T, and c_T are the tetragonal unit cell dimensions. Due to symmetry the e_{13}, e_{31}, e_{23}, and e_{32} are zero.[60] The strain tensor for any given state (S_i) of the possible q orientation sites, is given as:

$$\varepsilon^S(S_1) = \varepsilon(S_i) - \frac{1}{q}\sum_{k=1}^{q} \varepsilon(S_k) \tag{3.7}$$

In which $\varepsilon(S_i)$ is the strain tensor for the specific state defined previously by equation (3.1). For the ferroelastic transformation in the $LaNbO_4$ system the strain tensors for the 2 possible orientation states are defined as:[59]

$$\varepsilon^S(S_1) = \begin{pmatrix} -\varepsilon_{11}^S & \varepsilon_{12}^S & 0 \\ \varepsilon_{12}^S & \varepsilon_{11}^S & 0 \\ 0 & 0 & 0 \end{pmatrix} \tag{3.8}$$

$$\varepsilon_{11}^S = \frac{1}{2}(e_{11} - e_{22}) \tag{3.9}$$

$$\varepsilon_{12}^S = e_{12} \tag{3.10}$$

$$\varepsilon^S(S_2) = -\varepsilon^S(S_1) \tag{3.11}$$

After determining the spontaneous strain of the two possible states we can then determine the magnitude of spontaneous strain in the system at any temperature below the transformation temperature. The instantaneous measure of spontaneous strain is defined as:

$$(\varepsilon^S)^2 = 2[(\varepsilon_{11}^S)^2 + (\varepsilon_{12}^S)^2] \tag{3.12}$$

From the literature, it is known that pure $LaNbO_4$ has a spontaneous strain value ranging from 6.93% to 7.06%.[31, 33, 37] These values are considerably larger than the typical 3% maximum spontaneous strain observed in ferroelastic materials. Despite the much larger spontaneous strain values present in $LaNbO_4$ the transformation from monoclinic to tetragonal is maintained as a continuous second order transformation.

The change in the spontaneous strain in the system can also be used to determine the transformation temperature from the HTXRD datasets. Determining the transformation temperature by this method eliminates experimental error present in other methods, specifically the use of specific heat to determine the transformation temperature. As such specific heat (C_P) measurements were critical to this study. Specific heat measurements were used to determine transformation temperatures based on dopant concentration in the $LaNbO_4$ lattice. This is possible due to the second order nature of the transformation from monoclinic to tetragonal. As this transformation is reversible the measurement could be repeated to ensure reproducibility. Since the transformation is second order a single step change in the specific heat data is expected at the transformation temperature.[24, 33] The use of the spontaneous strain data to determine the true transformation temperature is necessary as structural changes can contribute to the specific heat of the material.[61] From an analytical standpoint, another drawback of using specific heat to determine transformation is the uncertainty of where the onset of the step change truly occurs. This is due to the sensitivity of the instrument and defining at which point in the step should be used as the determining feature for transformation, in this study the onset of the step change was defined as the transformation temperature.

Since spontaneous strain is determined by the lattice parameter values of the unit cell it is a measure free from sample processing limitations. As such, the spontaneous strain data can be treated with Landau theory to verify the characteristics of the phase transformation in a ferroelastic transformation. A power law fitting of the spontaneous strain data corresponding to a second order Landau fitting function can be used to calculate the temperature of the monoclinic to tetragonal phase transformation. To accurately determine the transformation temperature in this way any temperatures where the monoclinic and tetragonal phases coexisted were ignored. It was observed that the upper limit for pure monoclinic phase was approximately 460°C and the lower limit for the pure tetragonal phase was approximately 530°C. The relationship between spontaneous strain and the transformation temperature is given by::

$$\varepsilon^S = k\left[1 - \frac{T}{T_{tr}}\right]^{\eta} \tag{3.13}$$

where, ε^s is the spontaneous strain, k is a proportionality constant, T is the temperature in K, T_{tr} is the transformation temperature in K, and η is the Landau critical exponent. In the above expression ε^s and T are the experimentally determined parameters, while k, T_{tr}, and η are variables to be determined by fitting.

3.3.3 Thermal expansion tensor matrix

Thermal expansion of the present phases was determined using the Coefficient of Thermal Expansion Analysis Suite[62] (CTEAS) developed at the University of Illinois-Urbana-Champaign. This software is an elegant way to calculate the thermal expansion properties from lattice parameter changes and the subsequent changes in planar d-spacing. CTEAS produces the complete representation of thermal expansion in the form of the thermal expansion tensor. From the tensor elements, it is possible to determine the eigenvalues and eigenvectors. This approach is much more precise than determination of CTE through dilatometry in that it eliminates error due to porosity and microcracking. By averaging the eigenvalues the linear thermal expansion is determined which can be compared to the one determined through the dilatometric measurement.

The coefficient of thermal expansion is represented by a symmetric second rank tensor. Due to crystal symmetry the monoclinic system (α_M) has four unique tensor components, α_{11}, α_{22}, α_{33}, and α_{13}, while the tetragonal system (α_T) has 2 unique tensor components, $\alpha_{11}=\alpha_{22}$, and α_{33}. In both crystal systems there are tensor components equal to zero, α_{12} and α_{23} for the monoclinic system, and all the off diagonal tensor values are zero for the tetragonal phase, this is shown in equations (3.14) - (3.16).

$$\alpha_{ij} = \begin{bmatrix} \alpha_{11} & \alpha_{12} & \alpha_{13} \\ \alpha_{12} & \alpha_{22} & \alpha_{23} \\ \alpha_{13} & \alpha_{23} & \alpha_{33} \end{bmatrix} \tag{3.14}$$

$$\alpha_M = \begin{bmatrix} \alpha_{11} & 0 & \alpha_{13} \\ 0 & \alpha_{22} & 0 \\ \alpha_{13} & 0 & \alpha_{33} \end{bmatrix} \tag{3.15}$$

$$\alpha_T = \begin{bmatrix} \alpha_{11} & 0 & 0 \\ 0 & \alpha_{11} & 0 \\ 0 & 0 & \alpha_{33} \end{bmatrix} \tag{3.16}$$

The direction cosines are used to solve the expansion tensor values by the relationship:

$$\alpha_{hkl} = \frac{1}{d_{hkl}} \frac{dd_{hkl}}{\mathrm{d}T} \tag{3.17}$$

Moreover, in terms of CTE tensor elements it is:

$$\alpha_{hkl} = \alpha_{11}X^2 + \alpha_{22}Y^2 + \alpha_{33}Z^2 + 2\alpha_{12}XY + 2\alpha_{23}YZ + 2\alpha_{13}XZ \tag{3.18}$$

Where X, Y, and Z are the direct cosines corresponding to the orthonormal coordinate system and relating the specific plane to the crystallographic axes. These cosines are defined as:

$$X = \frac{h\left(\frac{1}{asin\beta}\right) + l\left(\frac{-cos\beta}{csin\beta}\right)}{|H_{hkl}|} \tag{3.19}$$

$$Y = \frac{k}{b|H_{hkl}|} \tag{3.20}$$

$$Z = \frac{l}{c|H_{hkl}|} \tag{3.21}$$

$$|H_{hkl}| = \frac{1}{d_{hkl}} \tag{3.22}$$

The orientation of the orthogonal axes of the CTE tensor with respect to the crystallographic axes follows the IEEE recommendations.[63]

3.3.4 Plane of zero thermal expansion

A CTE tensor with two positive and one negative eigenvalues, as in the case of the *m*-LaNbO$_4$ phases, mandates a unique direction (or plane normal) with zero thermal expansion (ZTE). Taking equation (3.23), and setting α′ to zero results in equation (3.24), which can be used to determine the θ and ϕ angles which give the direction of a plane with zero thermal expansion.

$$\alpha'_{ij} = \lambda_3 cos^2(\varphi)sin^2(\theta) + \lambda_1 sin^2(\varphi)sin^2(\theta) + \lambda_2 cos^2(\theta) \tag{3.23}$$

$$tan^2(\theta) = \frac{-\lambda_2}{\lambda_3 cos^2(\varphi) + \lambda_1 sin^2(\varphi)} \tag{3.24}$$

Where λ_i are the thermal expansion eigenvalues, θ is the elevation angle, and ϕ is the azimuthal angle in the orthonormal coordinates. For a given set of eigenvalues there are limits on θ and ϕ. For example, the right side of this equation must be a positive term, to satisfy this condition the denominator must have a negative value. Using the eigenvalues for pure *m*-LaNbO$_4$, from 200°C to 500°C in 50°C steps, the only values of ϕ , which satisfy the condition for a plane of zero CTE, are presented in Figure 3-5. In Figure 3-5(a) only the regions under the green line represent possible angles. In Figure 3-5(b) the same values of ϕ are possible. We also see that there are limits on the values of θ, mainly we see that θ cannot be 0° which means the plane of zero CTE will not be along the *b* axis and θ cannot be 90° indicating that the plane will not be in the *ac* plane of the crystal. Figure 3-5(b) also demonstrates that the conditions for the plane of zero CTE have the same symmetry operations as the monoclinic crystal; there is a twofold rotation axis and a mirror plane.

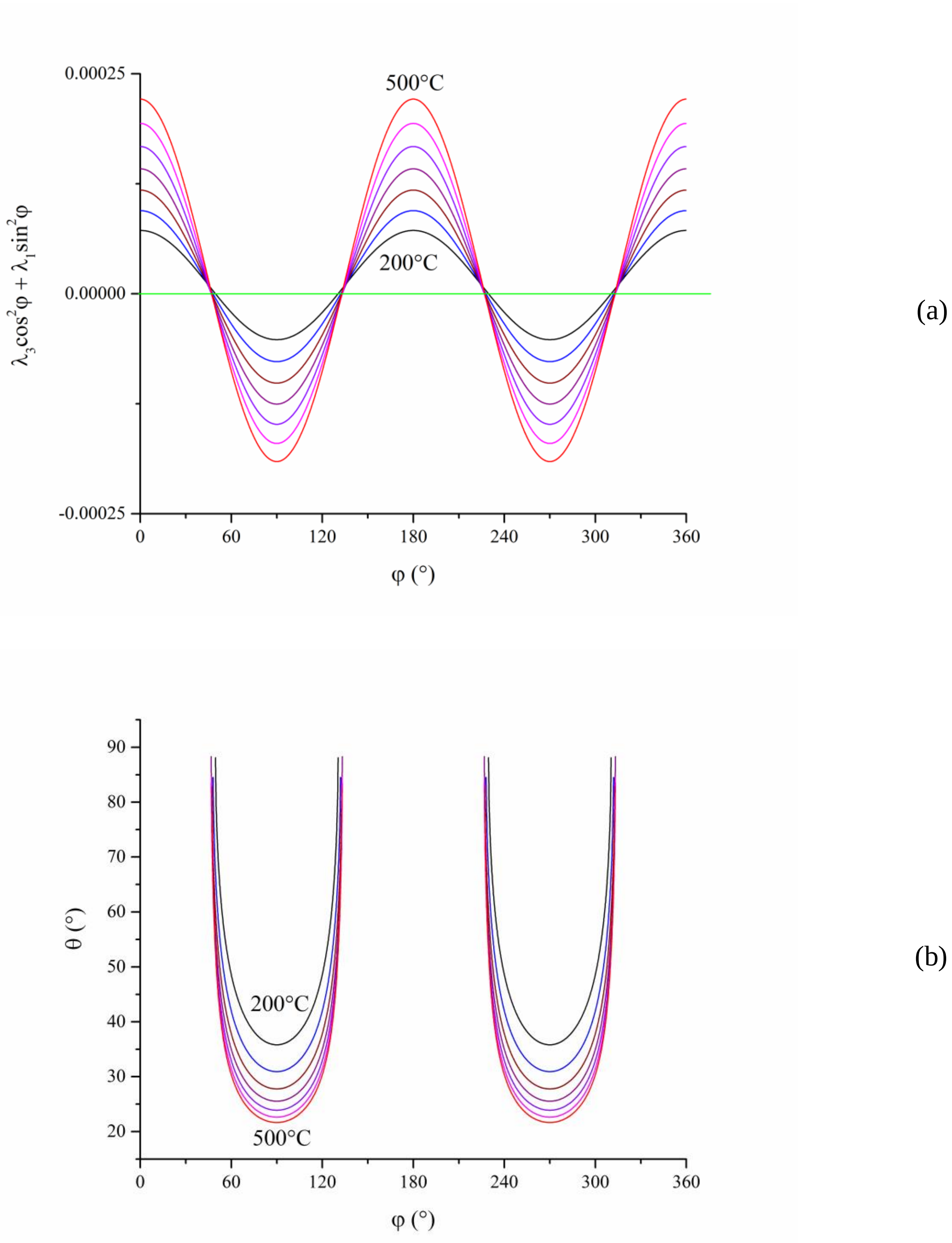

Figure 3-5: Thermal expansion direction angles for *m*-$LaNbO_4$ that satisfy the condition for zero CTE.

Once the direction of this plane in reference to the orthonormal coordinate system has been determined, a system of equations can be designed to relate the thermal expansion coordinates to the unit cell coordinate system. These equations are derived from equation (3.25), which gives the angle between two crystal planes in the monoclinic crystal.[64]

$$\cos(\varphi) = \frac{d_1 d_2}{sin^2(\beta)}\left(\frac{h_1 h_2}{a^2} + \frac{k_1 k_2 sin^2(\beta)}{b^2} + \frac{l_1 l_2}{c^2} - \frac{(l_1 h_2 + l_2 h_1)\cos(\beta)}{ac}\right) \tag{3.25}$$

In order to determine how the plane of zero thermal expansion in the spherical coordinate system corresponds to the crystallographic axes, geometric relationships were developed, Figure 3-6.

By applying these trigonometric relationships to the calculated direction angles θ and ϕ and the refined lattice parameters we are able to determine the (hkl) values for the plane of zero thermal expansion for any composition and temperature for which high temperature diffraction data has been collected. The determination of these (hkl) indices is completed using the system of equations (3.26) to (3.28), in which the equation has been derived from equation (3.25), with respect to the (100), (010), and (001) plane respectively. In these equations the values for *a, b, c,* and *β* are the unit cell parameters determined by Rietveld analysis of the HTXRD data, while θ and ϕ are determined from the eigenvalues using equation (3.24). In the solution *d* is set to 1 since the d-spacing term acts as a scalar and a different value would give a parallel plane as the solution.

$$\frac{\sin(\theta)}{\cos(\beta - \varphi)} = \left(\frac{d}{\sin^2(\beta)}\right) * \left(\frac{h}{a} - \frac{lcos(\beta)}{c}\right) \tag{3.26}$$

$$\cos(\theta) = d\left(\frac{k_2}{b}\right) \tag{3.27}$$

$$\sin(\theta)\cos(\varphi) = \left(\frac{d}{\sin^2(\beta)}\right) * \left(\frac{l}{c} - \frac{hcos(\beta)}{a}\right) \tag{3.28}$$

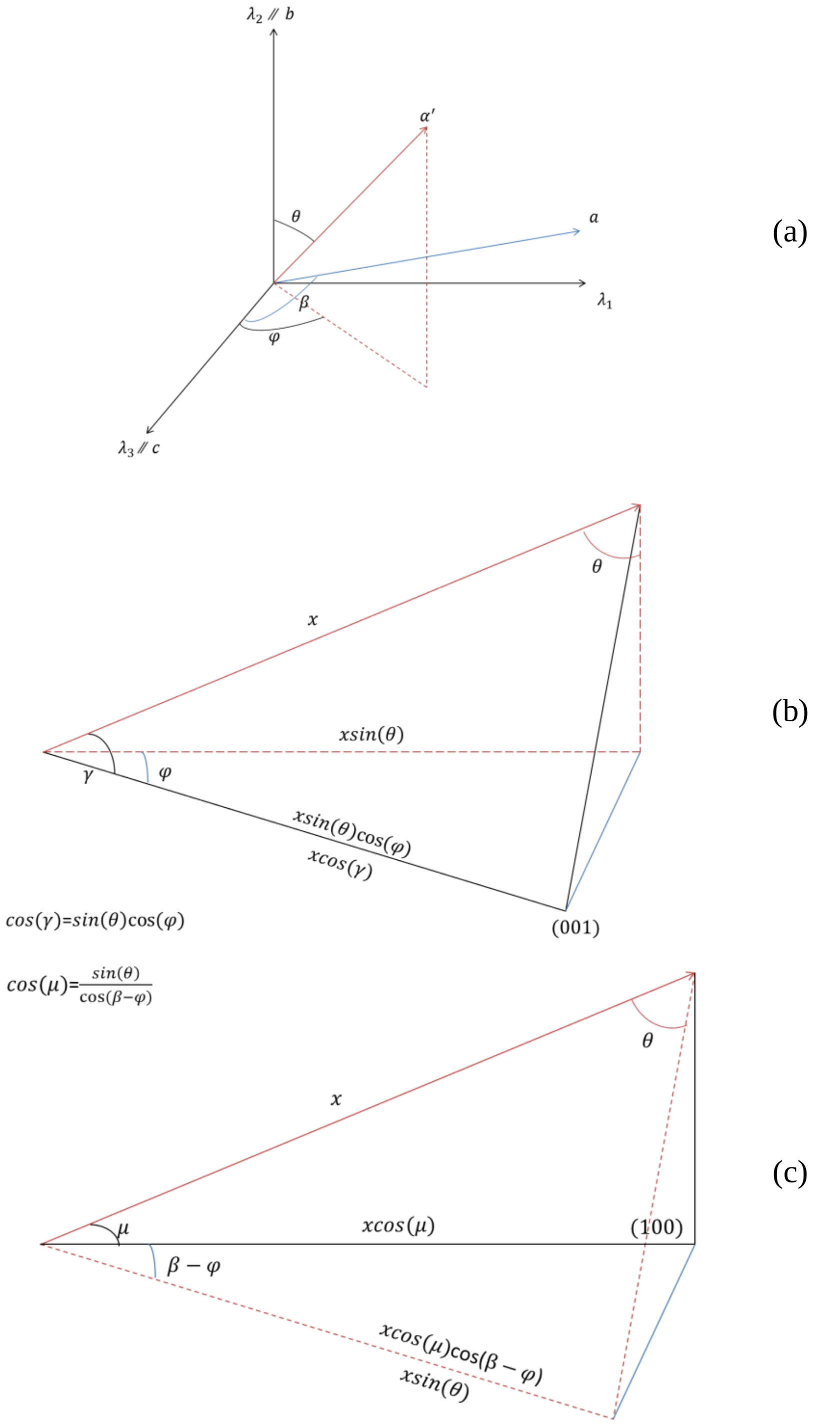

Figure 3-6: Geometric relationships between thermal expansion direction in spherical coordinates to the crystal coordinate system. (a) Orientation relationship between the two coordinate systems showing alignment of specific eigenvectors to the b and c axes with the third eigenvector in the ac plane. (b) and (c) show the trigonometric relationships derived to solve the direction of the plane of zero thermal expansion in unit cell.

CHAPTER 4.

EFFECT OF Ca^{2+} ON THE THERMAL EXPANSION OF $LaNbO_4$

4.1 Introduction

The most promising composition for acceptor doped $LaNbO_4$ proton conduction has been shown for 1 mol% Ca^{2+}. The purpose of this study is to understand how Ca^{2+} doping modifies the thermal expansion behavior of this material. Understanding thermal expansion is important since the anisotropic nature of the monoclinic crystal is mirrored in the thermal expansion. High anisotropy can lead to processing issues for the required thin membranes needed for SOFC devices. Additionally, minimizing crystal anisotropy will make the material more conducive to proton conduction. By knowing how different dopant concentrations modify this anisotropy the processing steps needed for these thin film membranes can be developed.

Compositions of $LaNbO_4$ doped with 0.5 mol%, 1.0 mol%, 1.5 mol%, and 2.0 mol% Ca^{2+}, were synthesized using the stearic entrapment method. After synthesis the powders were characterized for phase composition and distribution of the dopant ion. Room temperature XRD patterns of the powders, Figure 4-1, were analyzed for composition and from which it was determined that the powders were single phase. Lattice parameters were determined through Rietveld refinement of the XRD datasets using EXPGUI and GSAS.[55, 56, 57] For the present phases ICSD#20406, ICSD#37138, and ICSD#52250 were used for *m*LaNbO$_4$, *t*-LaNbO$_4$, and platinum respectively. For *m*- and *t*LaNbO$_4$ the crystal information file (cif) was modified to reflect the Ca^{2+} dopant. Additionally, DSC and STA measurement confirmed that no additional weight loss was experienced and that no phase transformation occurred that would be identified by the DSC measurement. The *m* → *t* phase transformation is second order and requires measurement of the specific heat capacity for identification. Finally, elemental distribution was qualitatively measured by EDS of multiple samples, with specific focus on the distribution of Ca^{2+}, Figure 4-2 and Figure 4-3 demonstrate the even distribution of calcium in the microstructure.

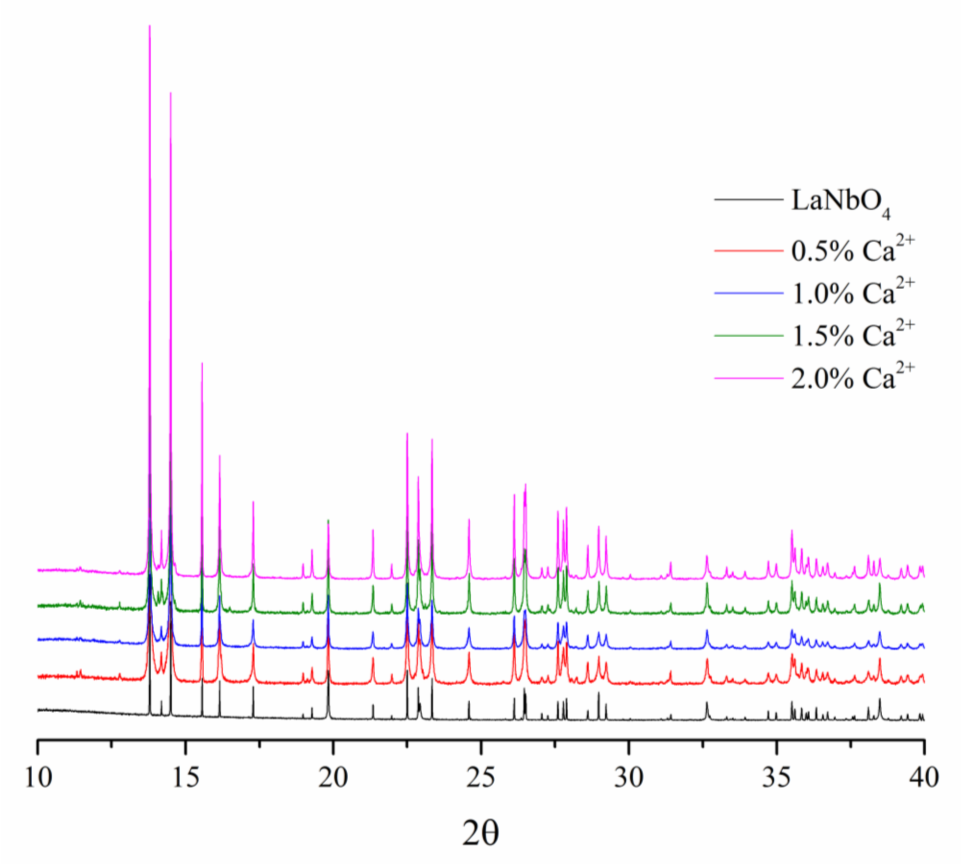

Figure 4-1: Room temperature XRD data sets for Ca^{2+} doped LaNbO$_4$.

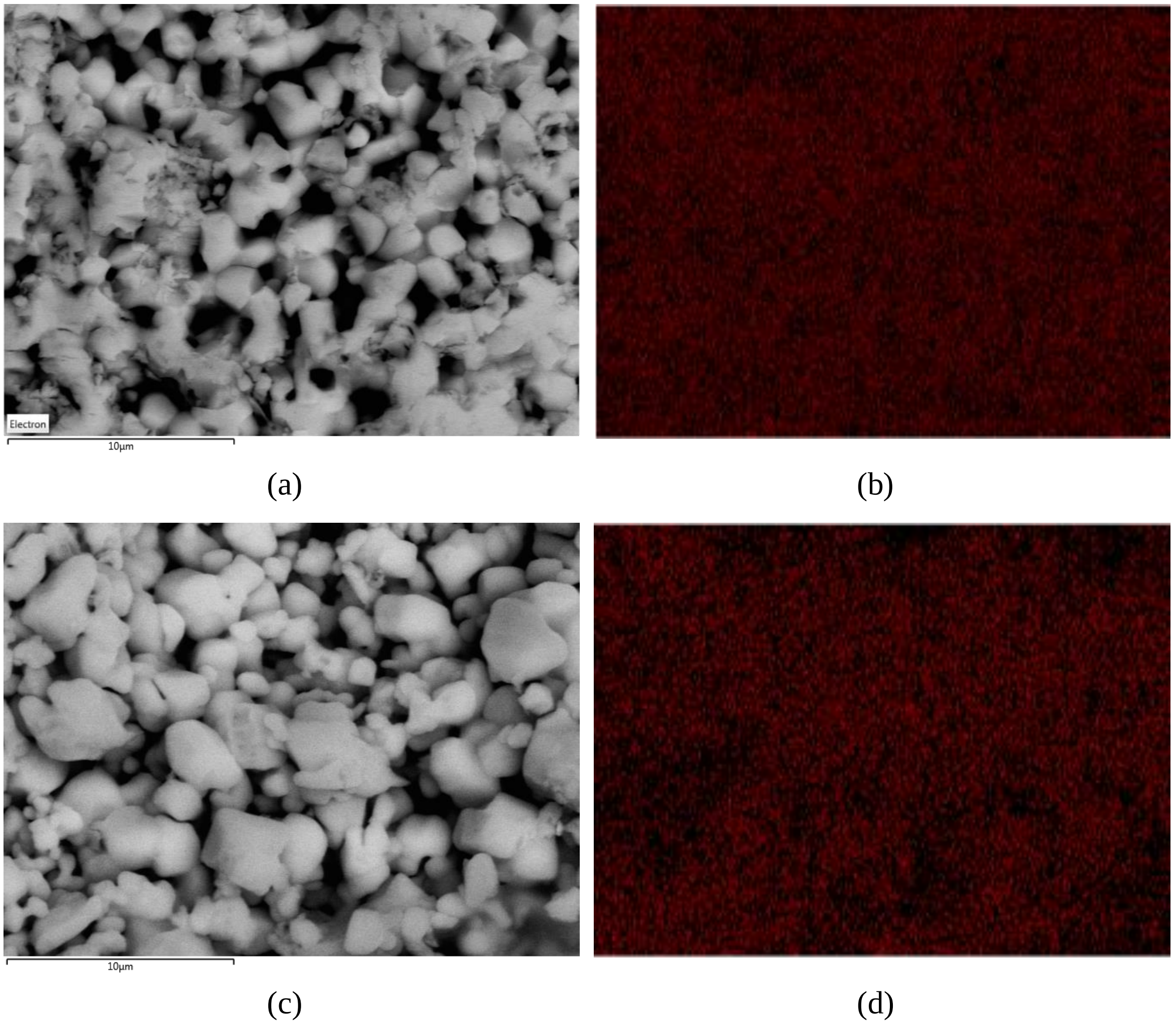

(a) (b)

(c) (d)

Figure 4-2: Elemental maps for Ca^{2+} dopant distribution in $LaNbO_4$, (a) and (c) are backscattered electron micrographs for 0.5%, and 1.0% Ca^{2+} respectively and (b) and (d) are the Ca^{2+} elemental maps for the respective concentrations.

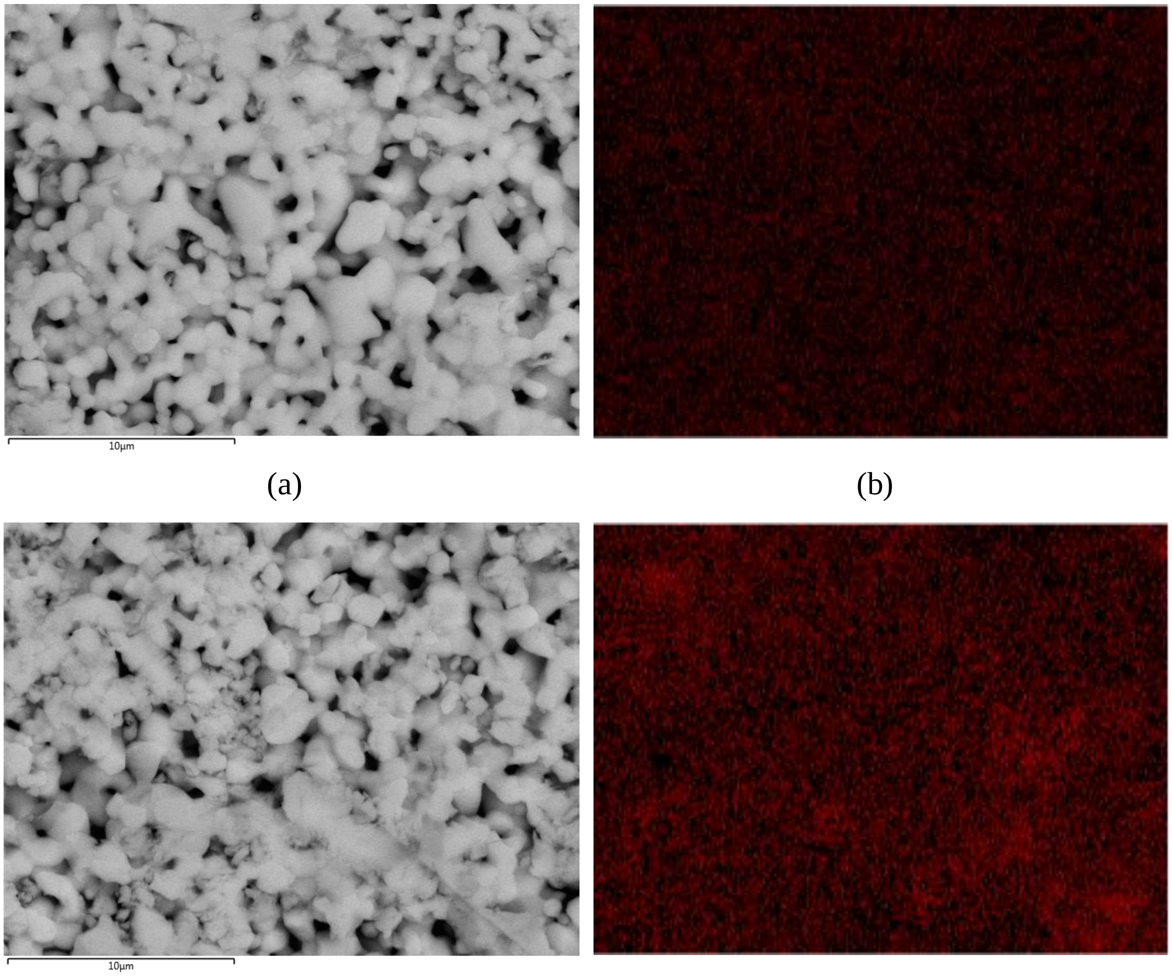

(a) (b)

(c) (d)

Figure 4-3: Elemental maps for Ca^{2+} dopant distribution in $LaNbO_4$, (a) and (c) are backscattered electron micrographs for 1.5%, and 2.0% Ca^{2+} respectively and (b) and (d) are the Ca^{2+} elemental maps for the respective concentrations.

4.2 Thermal expansion in *m*-$LaNbO_4$

The effect of Ca^{2+} doping on the monoclinic to tetragonal transformation was also studied by HTXRD. Diffraction patterns were collected at discrete set point temperatures from 20°C to 1200°C in order to observe the phase composition and determine the lattice parameters for the monoclinic and tetragonal phases as a function of temperature. The HTXRD data sets were refined using the Rietveld method to determine the lattice parameters at each temperature; this is presented in Figure 4-4.

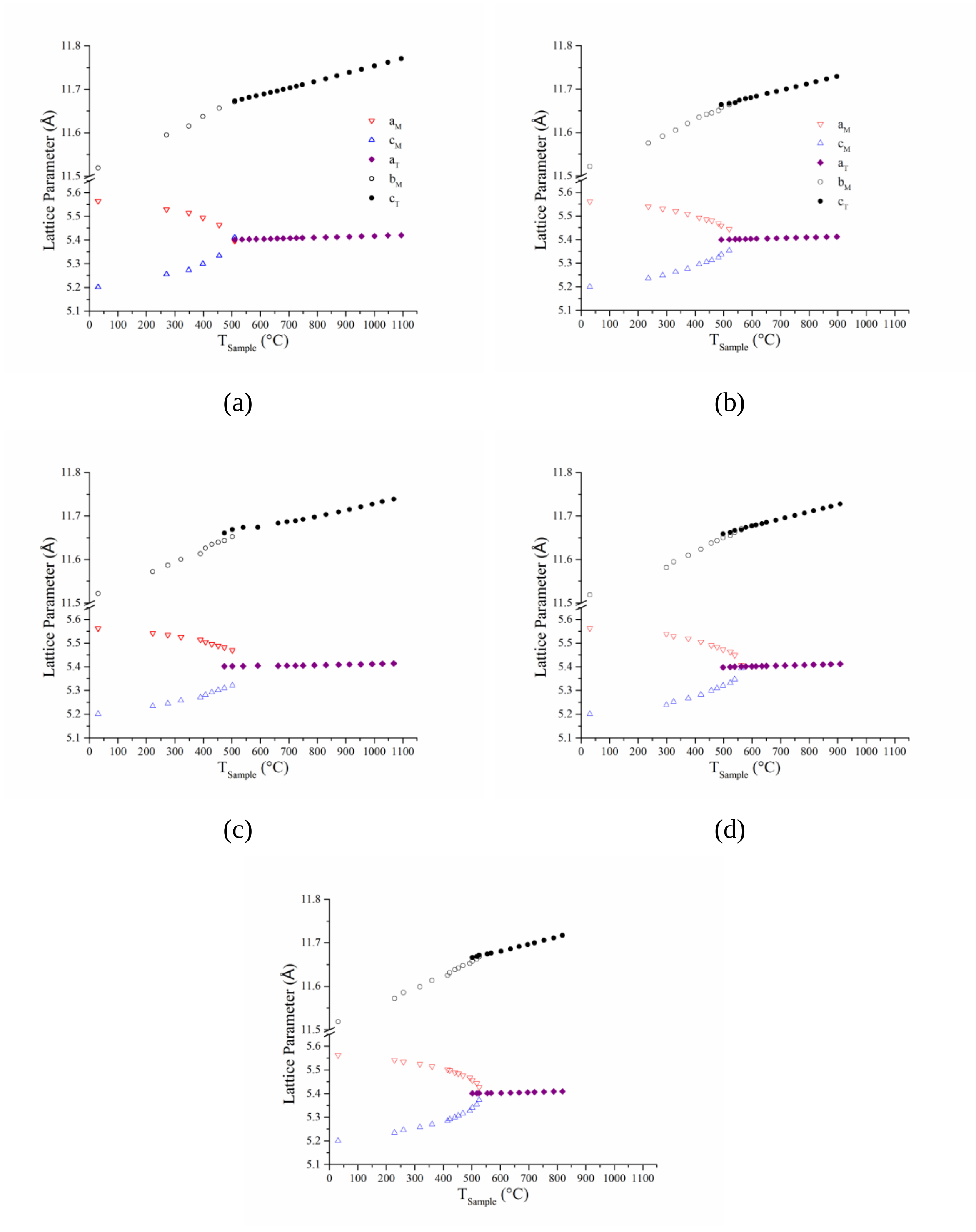

(a) (b)

(c) (d)

(e)

Figure 4-4: Unit cell lattice parameters for Ca^{2+} doped $LaNbO_4$ determined by Rietveld refinement of HTXRD datasets. Plots correspond as follows; (a) $LaNbO_4$ (b) 0.5% Ca^{2+}, (c) 1.0% Ca^{2+}, (d) 1.5% Ca^{2+}, and (e) 2.0% Ca^{2+}.

The thermal expansion in m-LaNbO$_4$ is highly anisotropic due to low crystal symmetry. In order to fully understand the coefficient of thermal expansion (CTE) properties the determination of the thermal expansion tensor matrix and the subsequent diagonalization of this matrix to produce the thermal expansion eigenvalues was completed using CTEAS and HTXRD datasets. The anisotropic CTE contributes to complications in the use of polycrystalline LaNbO$_4$ for PC-SOFC devices since the neighboring grains of the bulk layer will expand and contract relative to grain orientation resulting in microstructure stress. In order to improve the structural stability of the membrane a detailed understanding of thermal expansion is necessary.

The monoclinic LaNbO$_4$ thermal expansion tensor matrix elements are presented in Table 4-1. The tensor elements relate to the unit cell such that α_{11}, α_{33}, and α_{13} are in the *ac* plane while α_{22} lies along the monoclinic *b* axis. Due to the crystal symmetry α_{22} is the sole expansion component along b_M.

To describe the anisotropy of thermal expansion the aspherism index was determined from the CTE tensor values. This index quantifies the amount of thermal expansion anisotropy and was calculated using equations (4.1) to (4.3).[65]

$$A = \frac{2}{3} * \sqrt{1 - \frac{3i_2}{i_1^2}} \tag{4.1}$$

$$i_1 = \alpha_{11} + \alpha_{22} + \alpha_{33} \tag{4.2}$$

$$i_2 = \alpha_{11}\alpha_{22} + \alpha_{22}\alpha_{33} + \alpha_{11}\alpha_{33} - \alpha_{13}^2 \tag{4.3}$$

Where A is the aspherism coefficient, i_1 is the first invariant of the CTE tensor, i_2 is the second invariant of the CTE tensor, and α_{ij} are the thermal expansion tensor components. It should be noted that the first invariant (i_1) of the tensor represents volume thermal expansion.

Once the aspherism index for each composition was determined, we see that *A* increases as the monoclinic phase approaches transformation. This signifies that the thermal expansion becomes more anisotropic until the point where it transforms into the higher symmetry tetragonal phase.[66] A discontinuous change in *A* is expected to occur at a phase transformation. The thermal expansion behavior of the tetragonal phase will be addressed in the following section. Table 4-2 presents the aspherism index and volume thermal expansion for each composition. From this table we can see how the inclusion of Ca^{2+} into the structure decreases the CTE anisotropy, in all doped compositions the aspherism index is less than that of the pure $LaNbO_4$ sample. The inclusion of calcium is able to alter the nature of the thermal expansion such that it is less anisotropic which should lead to less thermal stress buildup in the microstructure as a result of thermal cycling. By decreasing the amount of stress in the microstructure this may be a preferred method of preserving the structural integrity of the electrolyte in a PC-SOFC. Figure 4-5, which presents *A* graphically, serves to reinforce the significant change in anisotropy for each composition. Doping with 1 mol% Ca^{2+} decreased *A* the most significantly and all other concentrations lowered *A* below the value seen for pure $LaNbO_4$. What is interesting to note regarding the pure $LaNbO_4$ data is that *A* peaks and then begins to decrease at about 475°C, while the doped compositions continue to increase through the temperature range and approach a maximum prior to transformation.

T	**LaNbO$_4$**				**0.5 mol% Ca^{2+}**				**1.0 mol% Ca^{2+}**				**1.5 mol% Ca^{2+}**				**2.0 mol% Ca^{2+}**			
	α_{11}	α_{13}	α_{22}	α_{33}	α_{11}	α_{13}	α_{22}	α_{33}	α_{11}	α_{13}	α_{22}	α_{33}	α_{11}	α_{13}	α_{22}	α_{33}	α_{11}	α_{13}	α_{22}	α_{33}
°C	10^{-5} /°C				10^{-5} /°C				10^{-5} /°C				10^{-5} /°C				10^{-5} /°C			
200	-2.71	4.98	2.72	4.69	-2.30	4.35	2.47	4.15	-2.16	4.08	2.37	3.90	-1.48	3.40	2.27	3.21	-1.92	3.94	2.48	3.72
225	-3.63	5.81	2.74	5.48	-2.73	4.75	2.48	4.57	-2.49	4.38	2.39	4.19	-2.17	4.08	2.33	3.84	-2.59	4.60	2.50	4.36
250	-4.56	6.64	2.77	6.30	-3.16	5.16	2.50	4.99	-2.81	4.67	2.41	4.49	-2.85	4.76	2.39	4.49	-3.26	5.23	2.52	4.98
275	-5.47	7.47	2.79	7.14	-3.59	5.56	2.52	5.42	-3.13	4.96	2.43	4.80	-3.54	5.43	2.45	5.16	-3.93	5.87	2.54	5.63
300	-6.38	8.28	2.82	8.01	-4.01	5.97	2.53	5.86	-3.46	5.25	2.45	5.11	-4.22	6.10	2.51	5.84	-4.59	6.49	2.56	6.28
325	-7.28	9.09	2.84	8.91	-4.44	6.37	2.55	6.32	-3.77	5.54	2.47	5.43	-4.90	6.78	2.57	6.55	-5.25	7.11	2.58	6.96
350	-8.16	9.88	2.86	9.84	-4.85	6.75	2.57	6.77	-4.09	5.82	2.49	5.76	-5.57	7.43	2.63	7.26	-5.90	7.73	2.60	7.66
375	-9.04	10.68	2.89	10.81	-5.27	7.15	2.58	7.26	-4.41	6.10	2.51	6.09	-6.23	8.08	2.70	8.00	-6.55	8.33	2.61	8.38
400	-9.90	11.45	2.91	11.81	-5.68	7.53	2.60	7.75	-4.72	6.38	2.53	6.43	-6.89	8.72	2.76	8.77	-7.17	8.90	2.63	9.09
425	-10.75	12.21	2.94	12.85	-6.09	7.91	2.62	8.25	-5.03	6.65	2.55	6.78	-7.54	9.36	2.82	9.56	-7.82	9.52	2.65	9.89
450	-11.58	12.96	2.96	13.94	-6.48	8.29	2.63	8.77	-5.33	6.92	2.56	7.13	-8.18	9.99	2.88	10.38	-8.45	10.11	2.67	10.69
475	-12.39	13.69	2.99	15.07	-6.88	8.65	2.65	9.30	-5.63	7.19	2.58	7.49	-8.81	10.60	2.94	11.22	-9.07	10.69	2.69	11.51
500	-13.18	14.41	3.01	16.24	-7.26	9.01	2.66	9.84	-5.93	7.45	2.60	7.87	-9.43	11.21	3.00	12.09	-9.67	11.25	2.71	12.36
525	-13.95	15.11	3.04	17.47	-7.64	9.37	2.68	10.40	-6.22	7.71	2.62	8.24	-10.04	11.80	3.06	13.00	-10.26	11.80	2.73	13.23

Table 4-1: CTE tensor values for the monoclinic phase of pure and Ca^{2+} doped LaNbO$_4$ compositions.

T	**$LaNbO_4$**		**0.5 mol% Ca^{2+}**		**1.0 mol% Ca^{2+}**		**1.5 mol% Ca^{2+}**		**2.0 mol% Ca^{2+}**	
°C	**A**	**β** (10^{-5} /°C)	**A**	**β** (10^{-5} /°C)	**A**	**β** (10^{-5} /°C)	**A**	**β** (10^{-5} /°C)	**A**	**β** (10^{-5} /°C)
200	1.55	4.70	1.47	4.32	1.45	4.10	1.22	4.00	1.33	4.28
225	1.88	4.59	1.62	4.32	1.57	4.09	1.48	4.01	1.58	4.27
250	2.21	4.51	1.77	4.33	1.69	4.09	1.74	4.03	1.83	4.25
275	2.55	4.46	1.92	4.35	1.81	4.09	1.99	4.08	2.08	4.24
300	2.86	4.45	2.06	4.38	1.93	4.10	2.22	4.14	2.32	4.25
325	3.16	4.47	2.18	4.43	2.03	4.12	2.44	4.23	2.54	4.29
350	3.41	4.54	2.30	4.49	2.14	4.15	2.63	4.33	2.74	4.35
375	3.63	4.65	2.41	4.57	2.24	4.19	2.80	4.47	2.92	4.44
400	3.79	4.82	2.51	4.67	2.32	4.24	2.93	4.63	3.07	4.55
425	3.90	5.04	2.59	4.78	2.40	4.29	3.04	4.83	3.19	4.72
450	3.95	5.32	2.65	4.92	2.48	4.36	3.11	5.07	3.28	4.90
475	3.96	5.66	2.70	5.07	2.54	4.44	3.16	5.35	3.34	5.13
500	3.92	6.07	2.74	5.25	2.60	4.54	3.18	5.66	3.37	5.40
525	3.85	6.55	2.76	5.44	2.64	4.64	3.17	6.02	3.37	5.70

Table 4-2: Calculated aspherism index (A) and volume thermal expansion (β) for pure and Ca^{2+} doped *m*-$LaNbO_4$.

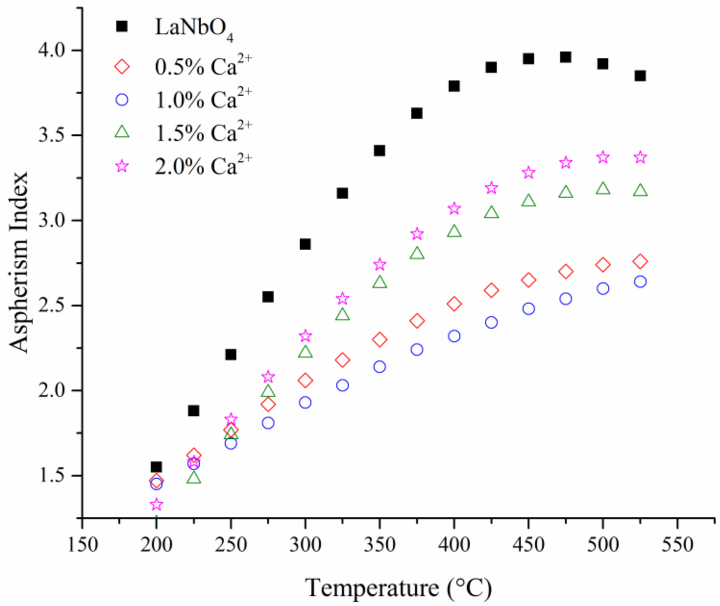

Figure 4-5: Aspherism index for each composition plotted as a function of temperature.

To further understand the thermal expansion it is necessary to determine the principal directions of maximum thermal expansion, this is accomplished by diagonalization of the tensor matrix resulting in the three CTE eigenvalues (λ_i). These eigenvalues represent the thermal expansion coefficient values in three mutually perpendicular directions; the eigenvalues for each composition are presented in Table 4-3. Comparing the eigenvalues of the doped compositions to the pure gives a better idea of how doping the structure modifies the thermal expansion properties.

The change in eigenvalue due to composition is treated the same as the tensor elements. With respect to expansion in the *ac* plane, the increased magnitude of eigenvalues 1 and 3 at 525°C compared to 200°C has been decreased from 384.1% and 327.3% respectively for pure LaNbO$_4$ to 259.1% and 226.9% for the 0.5% Ca^{2+}, 226.8% and 194.6% for the 1.0% Ca^{2+}, 459.6% and 360.0% for the 1.5% Ca^{2+}, and 384.4% and

315.5% for the 2.0% Ca^{2+} compositions. In the samples doped with 0.5 mol% and 1 mol% Ca^{2+} the change in thermal expansion has been decreased significantly, while the 2 mol% Ca^{2+} sample exhibited negligible change in expansion, and for the 1.5 mol% doped composition the magnitude of expansion increased for the first and third eigenvalues. Even with the varied amounts of change in the eigenvalues what remained consistent throughout the doped compositions was that both eigenvalues have an overall lower magnitude than that found in the pure sample, indicating that thermal expansion in samples containing calcium is decreased, and reinforces the conclusions reached on analysis of the tensor matrix.

When looking at the second eigenvalue, which corresponds to the *b* axis the composition with 1.5 mol% Ca^{2+} differs from all other compositions studied in that it has a much larger increase in expansion from low to high temperature, 134.8% as seen in Figure 4-6(b). Even with the increased thermal expansion in this direction until ~500°C the magnitude of expansion is lower than that in the pure system, and for all other compositions the magnitude of expansion is less that in pure $LaNbO_4$ throughout the entire temperature range. Thermal expansion in all directions was minimized most successfully for the composition containing 1 mol% Ca^{2+}. Volume CTE (β) is a useful property to show the combined effect of the eigenvalues, Table 4-2. Analysis of β further reinforces that doping $LaNbO_4$ with 1 mol% Ca^{2+} produces the most desirable thermal expansion behavior in the monoclinic phase. Looking at the two extreme temperatures reported it is shown that at 200°C the doped composition has a bulk thermal expansion that is ~13% lower than for the pure composition, and at 500°C, β is ~19% lower.

Using the thermal expansion eigenvalues it is possible to plot a three dimensional representation of the thermal expansion ellipsoid by using equation (4.4), and ranging both θ and ϕ from 0° to 360°.

$$\alpha'_{11} = (\lambda_1 cos^2\phi + \lambda_2 sin^2\phi)sin^2\theta + \lambda_3 cos^2\theta \tag{4.4}$$

Where α' is the value of thermal expansion in an arbitrary direction, λ_i are the thermal expansion eigenvalues determined from the tensor matrix, θ is the elevation angle in spherical coordinates, and ϕ is the azimuthal angle. Plotting equation (4.4) with the eigenvalues for pure $LaNbO_4$ at 200°C and 500°C produces the three dimensional thermal expansion ellipsoid, Figure 4-7. More useful than comparing the 3D ellipsoids of each composition is to look at 2D cross sections, this was done in 100°C steps in order to visualize the difference in thermal expansion of the *ac* plane.

T	**LaNbO$_4$**				**0.5 mol% Ca^{2+}**				**1.0 mol% Ca^{2+}**				**1.5 mol% Ca^{2+}**				**2.0 mol% Ca^{2+}**			
	λ_1	**λ_2**	**λ_3**	**λ_{avg}**	**λ_1**	**λ_2**	**λ_3**	**λ_{avg}**	**λ_1**	**λ_2**	**λ_3**	**λ_{avg}**	**λ_1**	**λ_2**	**λ_3**	**λ_{avg}**	**λ_1**	**λ_2**	**λ_3**	**λ_{avg}**
°C	10^{-5} /°C				10^{-5} /°C				10^{-5} /°C				10^{-5} /°C				10^{-5} /°C			
200	-5.22	2.72	7.20	1.57	-4.48	2.47	6.34	1.44	-4.22	2.37	5.95	1.37	-3.27	2.27	4.99	1.33	-3.94	2.48	5.75	1.43
225	-6.46	2.74	8.31	1.53	-5.07	2.48	6.91	1.44	-4.65	2.39	6.36	1.36	-4.23	2.33	5.90	1.34	-4.88	2.50	6.65	1.42
250	-7.71	2.77	9.45	1.50	-5.66	2.50	7.49	1.44	-5.09	2.41	6.77	1.36	-5.19	2.39	6.83	1.34	-5.80	2.52	7.53	1.42
275	-8.94	2.79	10.6	1.49	-6.24	2.52	8.08	1.45	-5.52	2.43	7.19	1.36	-6.15	2.45	7.77	1.36	-6.71	2.54	8.42	1.41
300	-10.1	2.82	11.7	1.48	-6.82	2.53	8.67	1.46	-5.95	2.45	7.60	1.37	-7.09	2.51	8.72	1.38	-7.62	2.56	9.31	1.42
325	-11.3	2.84	12.9	1.49	-7.39	2.55	9.27	1.48	-6.37	2.47	8.03	1.37	-8.05	2.57	9.70	1.41	-8.52	2.58	10.2	1.43
350	-12.5	2.86	14.2	1.51	-7.95	2.57	9.87	1.50	-6.79	2.49	8.46	1.38	-8.96	2.63	10.6	1.44	-9.40	2.60	11.1	1.45
375	-13.7	2.89	15.4	1.55	-8.51	2.58	10.5	1.52	-7.21	2.51	8.89	1.40	-9.88	2.70	11.6	1.49	-10.2	2.61	12.1	1.48
400	-14.8	2.91	16.7	1.61	-9.06	2.60	11.1	1.56	-7.61	2.53	9.33	1.41	-10.7	2.76	12.6	1.54	-11.0	2.63	13.0	1.52
425	-15.9	2.94	18.0	1.68	-9.59	2.62	11.7	1.59	-8.02	2.55	9.77	1.43	-11.6	2.82	13.6	1.61	-11.9	2.65	14.0	1.57
450	-17.0	2.96	19.3	1.77	-10.1	2.63	12.4	1.64	-8.41	2.56	10.2	1.45	-12.5	2.88	14.7	1.69	-12.8	2.67	15.0	1.63
475	-18.0	2.99	20.7	1.89	-10.6	2.65	13.0	1.69	-8.80	2.58	10.6	1.48	-13.3	2.94	15.7	1.78	-13.6	2.69	16.0	1.71
500	-19.0	3.01	22.1	2.02	-11.1	2.66	13.7	1.75	-9.19	2.60	11.1	1.51	-14.2	3.00	16.8	1.89	-14.4	2.71	17.0	1.80
525	-20.0	3.04	23.5	2.18	-11.6	2.68	14.3	1.81	-9.56	2.62	11.5	1.55	-15.0	3.06	17.9	2.01	-15.1	2.73	18.1	1.90

Table 4-3: CTE eigenvalues for *m*-LaNbO$_4$ representing magnitudes of maximum thermal expansion and the linear CTE.

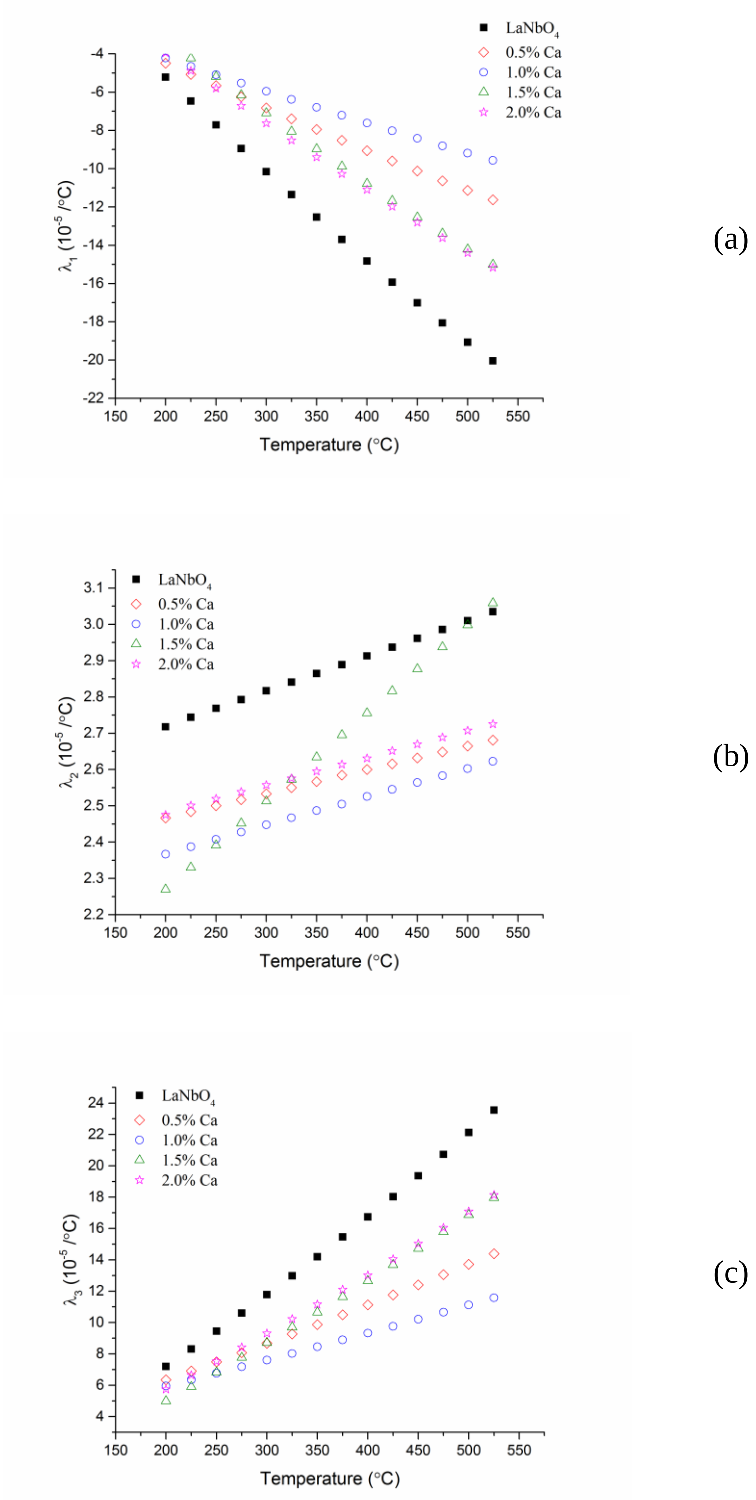

Figure 4-6: Eigenvalues of thermal expansion in the monoclinic phase for Ca^{2+} doped $LaNbO_4$.

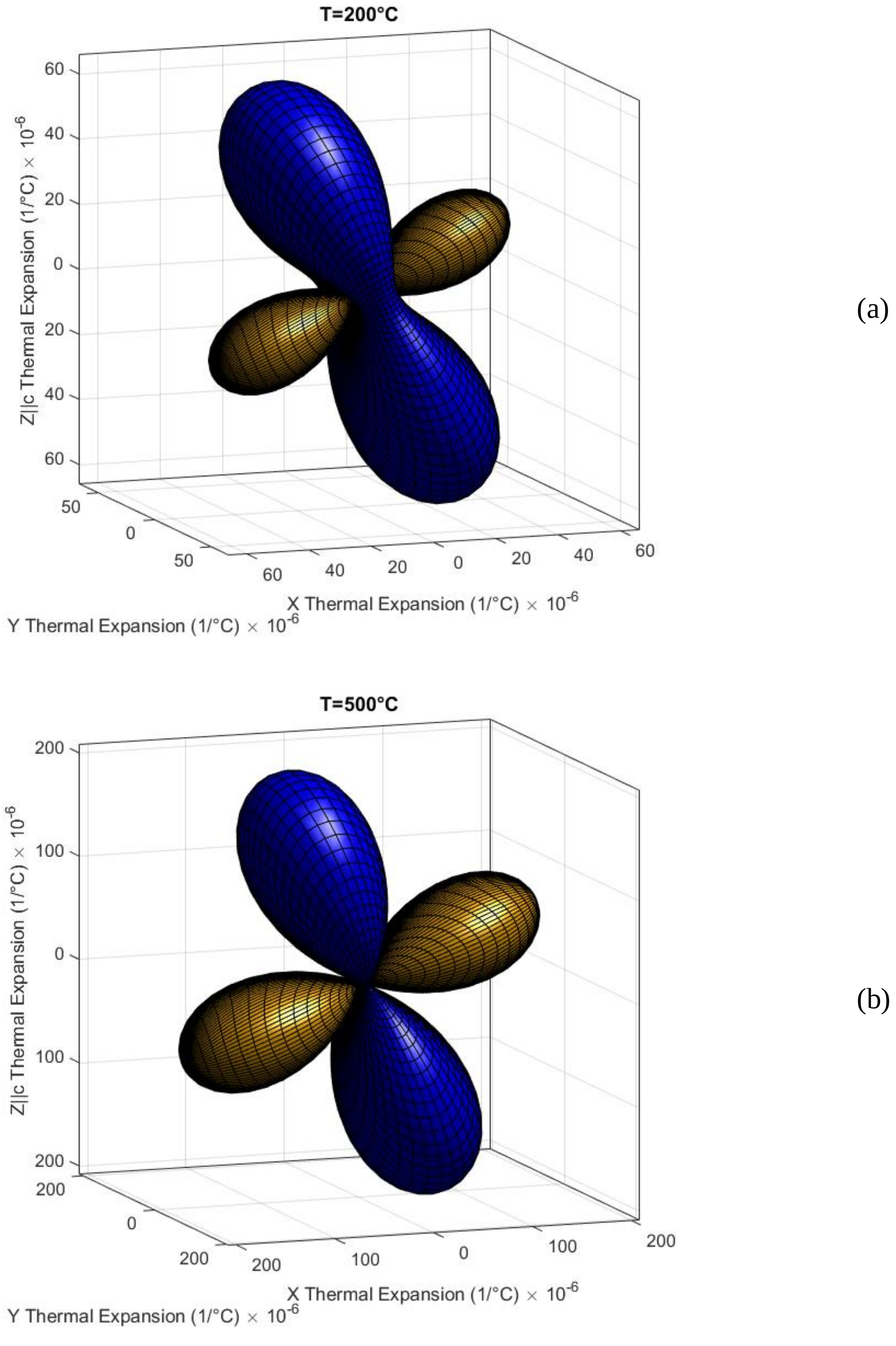

Figure 4-7: 3D CTE ellipsoid for *m*-$LaNbO_4$ at (a) 200°C and (b) 500°C.

Previously the differences in expansion eigenvalues were presented in table form and graphically as a comparison between compositions in response to increasing temperature.

Following a discussion of what the changes in eigenvalue magnitude represented in the crystal the 3D representation of the eigenvalue was introduced. However, the 3D representations for each composition are difficult to compare directly. Plotting the 2D cross sections simultaneously at selected temperatures allows for the comparison of the effect doping has on the thermal expansion characteristics. As expansion along the *b* axis, which corresponds to λ_2, is adequately represented by Figure 4-6(b) emphasis is directed to expansion of the *ac* plane. In Figure 4-8, the thermal expansion ellipsoid for the *ac* plane is presented along with the unit cell correspondence. By understanding where the crystallographic axis is in relation to the ellipsoid we reinforce that in non-orthogonal crystal systems the thermal expansion coordinate system does not align to the crystallographic coordinate system. This new representation serves to confirm what was discussed previously; at all temperatures the expansion of the pure system is greater in magnitude than any of the doped compositions. At the lowest temperature the sample with 1.5 mol% Ca^{2+} has the least amount of expansion in the plane followed by the sample with 2 mol% dopant, as temperature increases the magnitude of expansion for these compositions exceeds that of the 0.5 and 1.0 mol% samples until they become almost identical at 500°C.

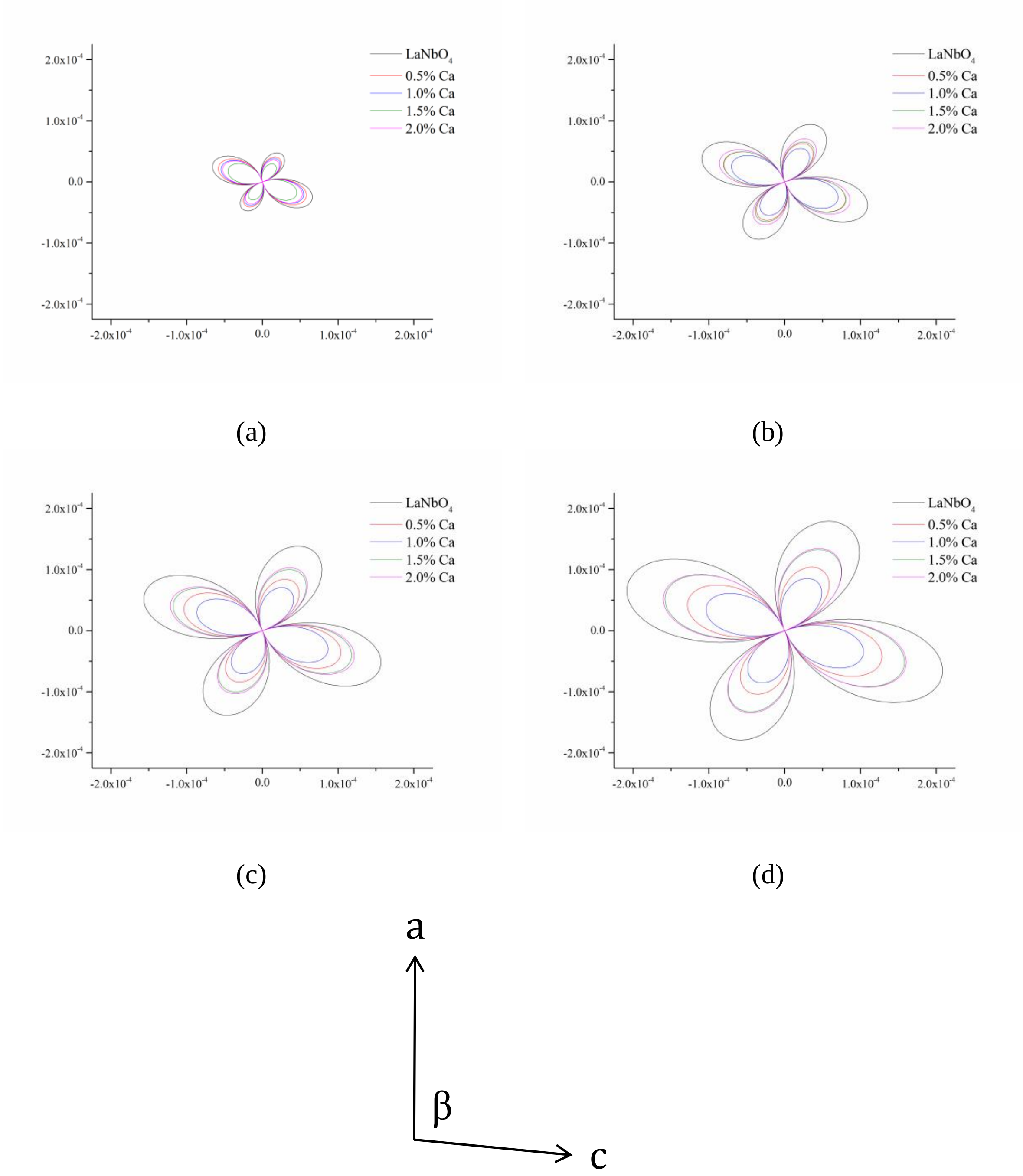

(a) (b)

(c) (d)

Figure 4-8: 2D thermal expansion ellipsoids for all compositions at temperatures (a) 200°C, (b) 300°C, (c) 400°C, and (d) 500°C.

4.3 Plane of zero CTE

The (*hkl*) indices of this plane for each composition were calculated from the eigenvalues, Table 4-4. Immediately apparent is the relatively minor variation between the different compositions. At 200°C the average indices that define the plane are (5.27 7.23 1.68) and at 500°C the plane is defined by (4.96 7.33 1.94). Comparison of the individual composition's miller indices to the average plane indices shows variation in the second decimal place which is negligible. As it relates to temperature we see the greatest variation corresponds to the *h* and *l* indices, while the smallest, variance relates to the *k* index. Plotting the ratio of the *h* to *l* indices with respect to the *k* index serves to demonstrate the relative invariance of this plane, Figure 4-9.

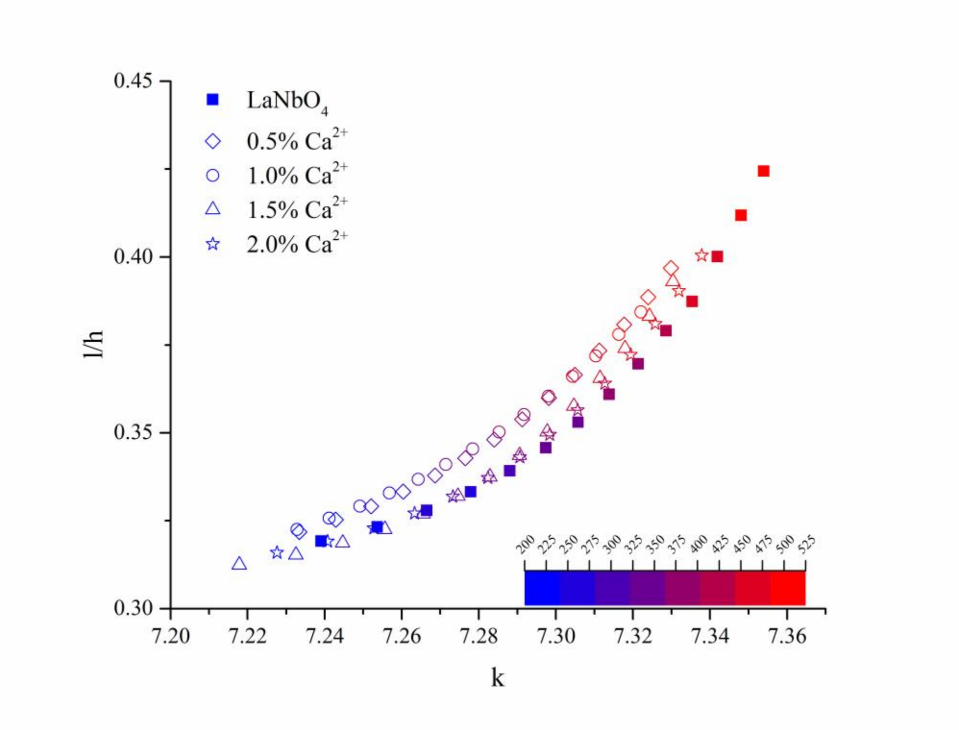

Figure 4-9: Plane of zero CTE miller indices in 25°C steps from 200°C to 525°C.

From this figure we see that the zero CTE plane for the pure, 1.5 mol% and 2.0 mol% doped compositions are quite similar, while the 0.5 mol% and 1.0 mol% samples have the least variance in plane indices. This finding is consistent with what was found from the thermal expansion eigenvalues.

4.4 Thermal expansion in *t*-$LaNbO_4$

Thermal expansion of the tetragonal phase of $LaNbO_4$ is greatly simplified compared to the monoclinic phase. This is due to the higher symmetry of the tetragonal phase which causes the thermal expansion tensor elements to align directly with the crystal axes. Additionally, due to crystal symmetry there are only 2 unique tensor elements, where α_{11} and α_{22} are equivalent and α_{33} is the other unique element. Another change in the thermal expansion behavior is that all eigenvalues are positive in nature indicating thermal expansion in all directions with no contraction, eigenvalues for each composition are presented in Table 4-5 and Figure 4-10.

The increase in symmetry changes the CTE ellipsoid appearance significantly; the overall shape now resembles a peanut, Figure 4-11. This is due to the isotropic expansion of the *ab* plane having a circular cross section since λ_1 and λ_2 are equivalent, while the ellipsoid expands parallel to the *c* axes due to λ_3 being a unique quantity. As the expansion in the *ab* plane is isotropic, the overall thermal expansion in the crystal becomes more isotropic.

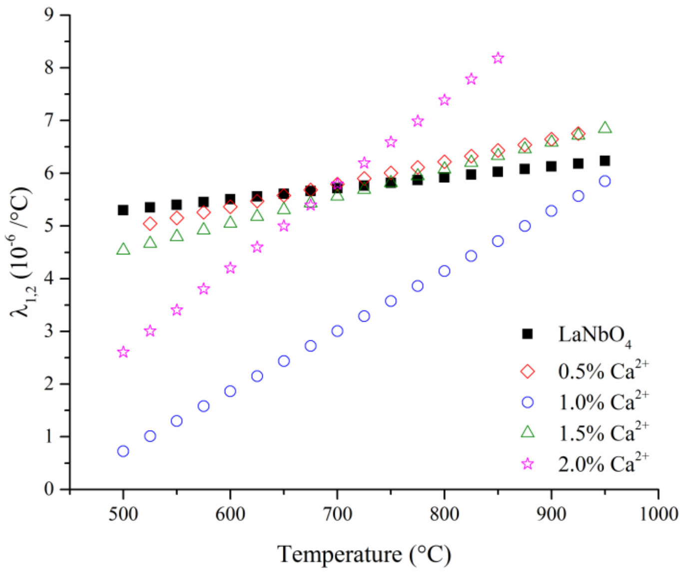

(a)

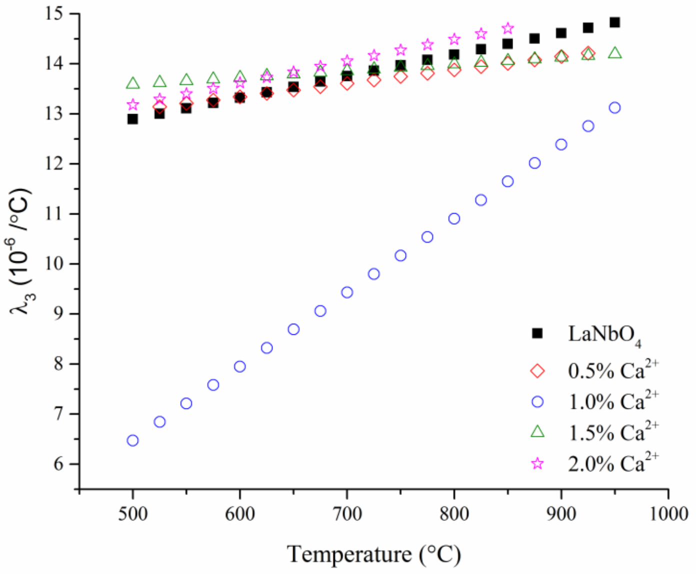

(b)

Figure 4-10: Eigenvalues of thermal expansion in the tetragonal phase for Ca^{2+} doped $LaNbO_4$.

T	**LaNbO$_4$**			**0.5 mol% Ca^{2+}**			**1.0 mol% Ca^{2+}**			**1.5 mol% Ca^{2+}**			**2.0 mol% Ca^{2+}**		
°C	**h**	**k**	**l**	**h**	**k**	**l**	**h**	**k**	**l**	**h**	**k**	**l**	**h**	**k**	**l**
200	5.27	7.24	1.68	5.26	7.23	1.69	5.25	7.23	1.69	5.30	7.22	1.66	5.28	7.23	1.67
225	5.25	7.25	1.70	5.24	7.24	1.70	5.24	7.24	1.71	5.29	7.23	1.67	5.27	7.24	1.68
250	5.23	7.27	1.71	5.22	7.25	1.72	5.22	7.25	1.72	5.27	7.24	1.68	5.25	7.25	1.69
275	5.20	7.28	1.73	5.20	7.26	1.73	5.21	7.26	1.73	5.25	7.26	1.69	5.23	7.26	1.71
300	5.18	7.29	1.76	5.18	7.27	1.75	5.19	7.26	1.75	5.23	7.27	1.71	5.21	7.27	1.73
325	5.15	7.30	1.78	5.16	7.28	1.77	5.17	7.27	1.76	5.21	7.27	1.73	5.18	7.28	1.75
350	5.12	7.31	1.81	5.14	7.28	1.79	5.15	7.28	1.78	5.18	7.28	1.75	5.16	7.29	1.77
375	5.08	7.31	1.83	5.12	7.29	1.81	5.13	7.29	1.80	5.16	7.29	1.77	5.13	7.30	1.79
400	5.05	7.32	1.87	5.09	7.30	1.83	5.11	7.29	1.82	5.13	7.30	1.80	5.10	7.31	1.82
425	5.01	7.33	1.90	5.06	7.30	1.86	5.09	7.30	1.83	5.10	7.30	1.82	5.07	7.31	1.85
450	4.97	7.34	1.92	5.04	7.31	1.88	5.07	7.30	1.85	5.07	7.31	1.85	5.04	7.32	1.87
475	4.92	7.34	1.97	5.01	7.32	1.91	5.04	7.31	1.88	5.03	7.32	1.88	5.00	7.33	1.91
500	4.87	7.35	2.01	4.97	7.32	1.93	5.02	7.32	1.90	4.99	7.32	1.91	4.96	7.33	1.94
525	4.83	7.35	2.05	4.94	7.33	1.96	4.99	7.32	1.92	4.95	7.33	1.95	4.92	7.34	1.97

Table 4-4: Miller indices for plane of zero CTE for each composition.

T	**LaNbO$_4$**				**0.5 mol% Ca^{2+}**				**1.0 mol% Ca^{2+}**				**1.5 mol% Ca^{2+}**				**2.0 mol% Ca^{2+}**			
	λ_1	**λ_2**	**λ_3**	**λ_{avg}**	**λ_1**	**λ_2**	**λ_3**	**λ_{avg}**	**λ_1**	**λ_2**	**λ_3**	**λ_{avg}**	**λ_1**	**λ_2**	**λ_3**	**λ_{avg}**	**λ_1**	**λ_2**	**λ_3**	**λ_{avg}**
°C	10^{-6} /°C				10^{-6} /°C				10^{-6} /°C				10^{-6} /°C				10^{-6} /°C			
525	5.35	5.35	13.00	7.90	5.05	5.05	13.14	7.74	1.01	1.01	6.84	2.96	4.67	4.67	13.62	7.65	3.00	3.00	13.29	6.43
550	5.40	5.40	13.11	7.97	5.15	5.15	13.21	7.84	1.30	1.30	7.21	3.27	4.79	4.79	13.66	7.75	3.40	3.40	13.40	6.74
575	5.45	5.45	13.22	8.04	5.26	5.26	13.28	7.93	1.58	1.58	7.58	3.58	4.92	4.92	13.69	7.84	3.80	3.80	13.51	7.04
600	5.51	5.51	13.32	8.11	5.37	5.37	13.34	8.02	1.87	1.87	7.95	3.89	5.05	5.05	13.72	7.94	4.20	4.20	13.62	7.34
625	5.56	5.56	13.43	8.18	5.47	5.47	13.41	8.12	2.15	2.15	8.32	4.21	5.18	5.18	13.76	8.04	4.60	4.60	13.73	7.64
650	5.61	5.61	13.54	8.25	5.58	5.58	13.48	8.21	2.43	2.43	8.69	4.52	5.31	5.31	13.79	8.13	5.00	5.00	13.84	7.94
675	5.66	5.66	13.64	8.32	5.69	5.69	13.54	8.30	2.72	2.72	9.06	4.83	5.43	5.43	13.82	8.23	5.40	5.40	13.95	8.25
700	5.71	5.71	13.75	8.39	5.79	5.79	13.61	8.40	3.00	3.00	9.43	5.15	5.56	5.56	13.86	8.33	5.79	5.79	14.05	8.55
725	5.77	5.77	13.86	8.46	5.90	5.90	13.68	8.49	3.29	3.29	9.80	5.46	5.69	5.69	13.89	8.42	6.19	6.19	14.16	8.85
750	5.82	5.82	13.97	8.53	6.01	6.01	13.74	8.58	3.57	3.57	10.17	5.77	5.82	5.82	13.93	8.52	6.59	6.59	14.27	9.15
775	5.87	5.87	14.07	8.60	6.11	6.11	13.81	8.68	3.86	3.86	10.54	6.09	5.95	5.95	13.96	8.62	6.99	6.99	14.38	9.45
800	5.92	5.92	14.18	8.67	6.22	6.22	13.88	8.77	4.14	4.14	10.91	6.40	6.07	6.07	13.99	8.71	7.39	7.39	14.49	9.75
825	5.97	5.97	14.29	8.74	6.33	6.33	13.94	8.87	4.43	4.43	11.28	6.71	6.20	6.20	14.03	8.81	7.78	7.78	14.60	10.06
850	6.03	6.03	14.40	8.82	6.43	6.43	14.01	8.96	4.71	4.71	11.65	7.02	6.33	6.33	14.06	8.91	8.18	8.18	14.70	10.36
875	6.08	6.08	14.50	8.89	6.54	6.54	14.08	9.05	5.00	5.00	12.02	7.34	6.46	6.46	14.09	9.00				
900	6.13	6.13	14.61	8.96	6.65	6.65	14.14	9.15	5.28	5.28	12.39	7.65	6.59	6.59	14.13	9.10				
925	6.18	6.18	14.72	9.03	6.75	6.75	14.21	9.24	5.57	5.57	12.76	7.96	6.71	6.71	14.16	9.20				
950	6.23	6.23	14.83	9.10					5.85	5.85	13.12	8.28	6.84	6.84	14.19	9.29				

Table 4-5: Eigenvalues of CTE for *t*-LaNbO$_4$.

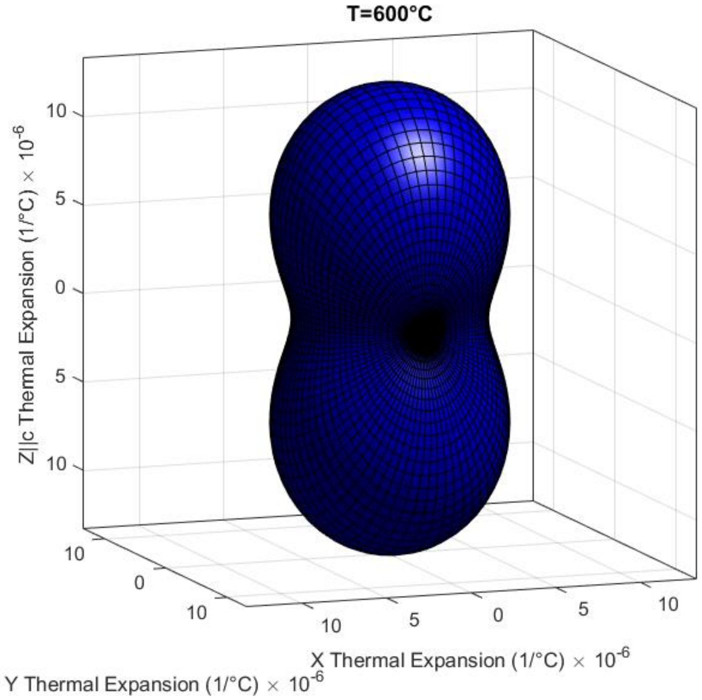

Figure 4-11: 3D CTE ellipsoid for t-$LaNbO_4$, shown at 600°C.

Determining the aspherism index for the tetragonal phase produces values between 0.5 and 0.1 for all compositions throughout the temperature range, *A* and β are presented in Table 4-6. From the aspherism index for pure $LaNbO_4$ it is immediately apparent that the thermal expansion behavior is much less anisotropic for the tetragonal phase, as seen in the decrease of *A* from 3.85 to 0.2153 at 525°C, Table 4-2 and Table 4-6. A significant change in *A* is expected with a phase transformation. We know that isotropic thermal expansion has an *A* value of zero.[65, 66] Aside from the order of magnitude drop in the aspherism index the trend for the index with temperature is also different in the tetragonal phase. In the monoclinic phase the CTE became more anisotropic with increasing temperature, however, for the tetragonal phase *A* decreases as the temperature increases,

Figure 4-12. From the phase diagram for La_2O_3 and Nb_2O_5 it is known that $LaNbO_4$ melts at approximately 1620°C. Extrapolation of the aspherism index should be possible to determine properties of this system outside the experimental constraints. However, the determination of the appropriate model for this extrapolation was not within the scope of this study. From the experimental data, the composition containing 2 mol% Ca^{2+} becomes the least anisotropic at elevated temperatures and that the sample with 1 mol% Ca^{2+} maintains the most anisotropy among the doped compositions.

As the CTE ellipsoid become more isotropic with increasing temperature the bulk thermal expansion continues to increase. The addition of calcium to the structure lowers the bulk thermal expansion for all compositions in the temperatures around transformation, however as the temperature is increased the only composition maintaining less bulk thermal expansion than the undoped sample is the sample with 1 mol% Ca^{2+}. While this sample shows a decrease in β throughout the entire temperature range it also demonstrates the greatest change in magnitude. With a nearly threefold increase in β this composition may pose new challenges as an electrolyte membrane. If the interconnect materials are not tailored to match the change in thermal expansion then the structural integrity of the device could be compromised during thermal cycling.

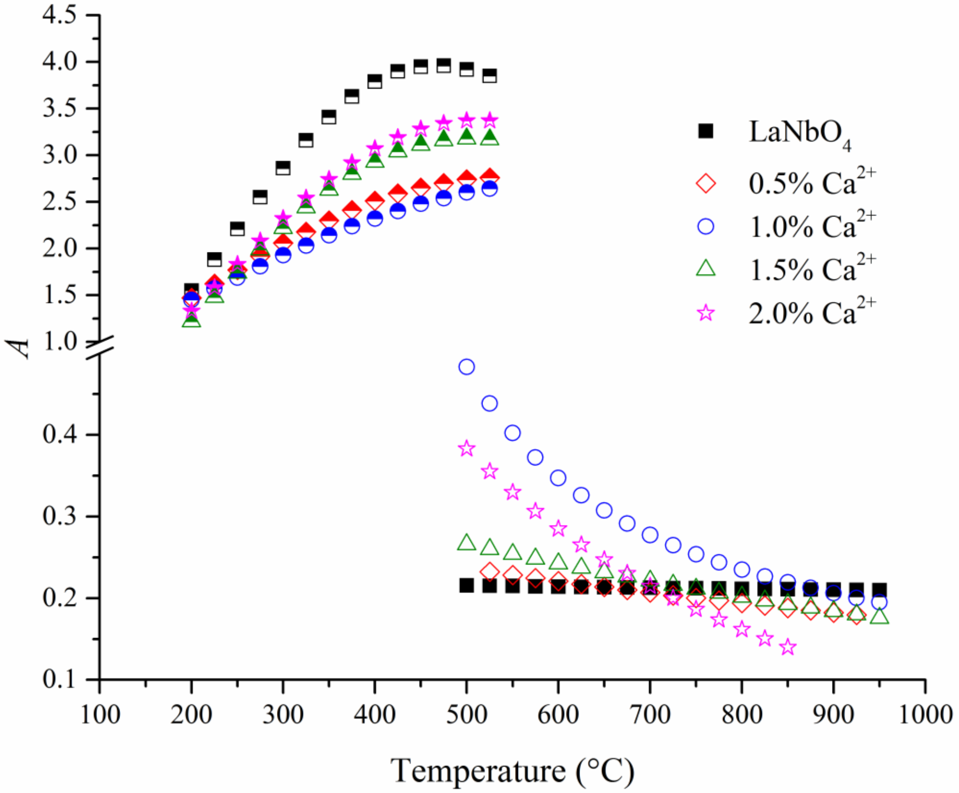

Figure 4-12: Aspherism index for *m- and t*-LaNbO$_4$, the half filled symbols represent *A* in the monoclinic phase.

.

T	**LaNbO$_4$**		**0.5 mol% Ca^{2+}**		**1.0 mol% Ca^{2+}**		**1.5 mol% Ca^{2+}**		**2.0 mol% Ca^{2+}**	
	A	**β**	**A**	**β**	**A**	**β**	**A**	**β**	**A**	**β**
°C	**10^{-1}**	**10^{-6} /°C**	**10^{-1}**	**10^{-6} /°C**	**10^{-1}**	**10^{-6} /°C**	**10^{-1}**	**10^{-6} /°C**	**10^{-1}**	**10^{-6} /°C**
525	2.153	23.70	2.323	23.23	4.386	8.87	2.601	22.95	3.553	19.30
550	2.149	23.91	2.284	23.51	4.023	9.81	2.542	23.24	3.298	20.21
575	2.145	24.12	2.246	23.79	3.724	10.74	2.484	23.53	3.065	21.11
600	2.142	24.33	2.209	24.07	3.473	11.68	2.427	23.82	2.851	22.02
625	2.138	24.55	2.173	24.35	3.260	12.62	2.372	24.11	2.655	22.93
650	2.135	24.76	2.137	24.63	3.076	13.56	2.318	24.40	2.473	23.83
675	2.132	24.97	2.103	24.91	2.915	14.50	2.265	24.69	2.304	24.74
700	2.128	25.18	2.069	25.19	2.775	15.44	2.214	24.98	2.148	25.64
725	2.125	25.39	2.036	25.47	2.650	16.38	2.164	25.27	2.002	26.55
750	2.122	25.60	2.003	25.75	2.539	17.32	2.114	25.56	1.865	27.45
775	2.119	25.81	1.971	26.04	2.439	18.26	2.066	25.85	1.738	28.36
800	2.116	26.02	1.940	26.32	2.349	19.19	2.019	26.14	1.618	29.26
825	2.113	26.23	1.910	26.60	2.268	20.13	1.973	26.43	1.505	30.17
850	2.110	26.45	1.880	26.88	2.194	21.07	1.929	26.72	1.399	31.07
875	2.107	26.66	1.851	27.16	2.126	22.01	1.885	27.01		
900	2.104	26.87	1.822	27.44	2.063	22.95	1.842	27.30		
925	2.102	27.08	1.794	27.72	2.006	23.89	1.799	27.59		
950	2.099	27.29			1.953	24.83	1.758	27.88		

Table 4-6: Aspherism index and volume CTE for all compositions.

4.5 Effect of Ca^{2+} concentration on the phase transformation temperature

The addition of Ca^{2+} to the $LaNbO_4$ lattice exhibited very little change on the phase transformation temperature when determined by specific heat measurement. The $m \rightarrow t$ transformation in $LaNbO_4$, which occurs at approximately 500°C,[31, 32, 33] is a second order transformation and as such is observable by a single step change in the specific heat capacity, Figure 4-13. The step change in the C_p plots appears to show an extended temperature range for the pre and post transformation C_p values; this is due to the characteristics of the sample. As the samples studied were pressed powder and not fully dense error was introduced to the measurement due to a range of particle sizes in the powder. In the case of doping the structure with Ca^{2+} ions the transformation temperature as determined from specific heat measurement was found to be 497.9°C for the pure $LaNbO_4$. The largest deviation from this was a decrease to 483.2°C for the sample doped with 2 mol% Ca^{2+}, all other compositions exhibited a transformation temperature between these values, Table 4-7. In the case of each sample the change in C_P was observed indicating that the inclusion of an aliovalent dopant cation did not change the nature of the transformation. The onset temperature of the change in C_P was used as the monoclinic to tetragonal transformation temperature.

Sample	$LaNbO_4$	0.5% Ca^{2+}	1.0% Ca^{2+}	1.5% Ca^{2+}	2.0% Ca^{2+}
T_{Tr} (°C)	497.9	495.7	488.7	483.0	483.2

Table 4-7: Monoclinic to tetragonal phase transformation temperature for Ca^{2+} doped $LaNbO_4$ determined by C_P measurement.

The effect of Ca^{2+} doping on the monoclinic to tetragonal transformation was also studied by HTXRD. Diffraction patterns were collected at discrete set point temperatures from 20°C to 1200°C in order to observe the phase composition and determine the lattice parameters for the monoclinic and tetragonal phases as a function of temperature. The HTXRD data sets were refined using the Rietveld method to determine the lattice parameters at each temperature; this is presented in Figure 4-4.

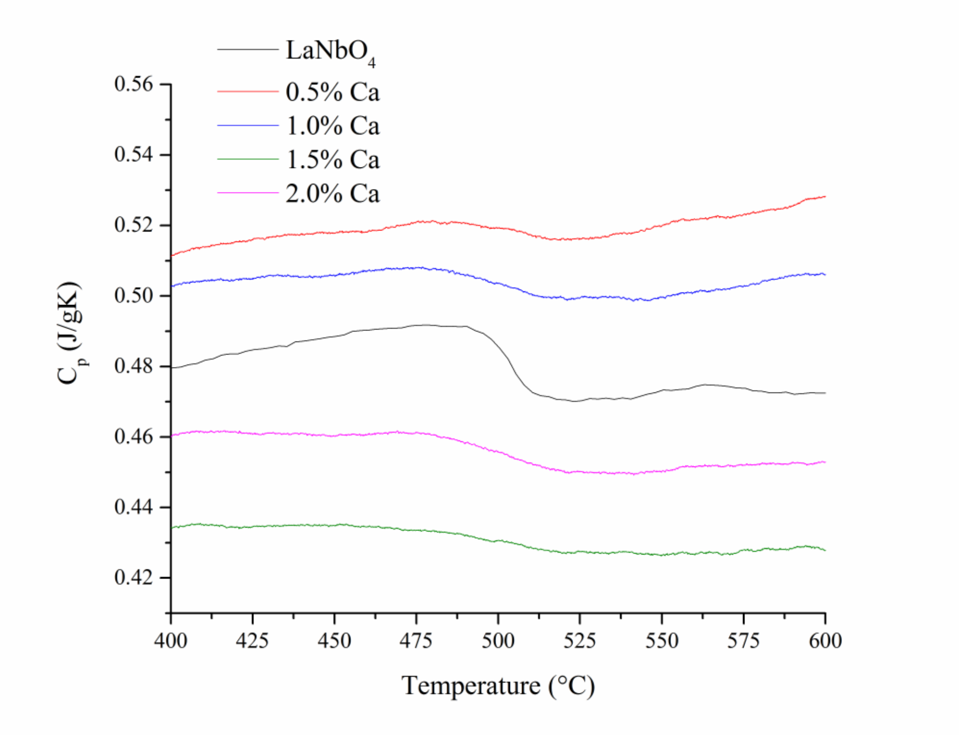

Figure 4-13: Specific heat data for pure and Ca^{2+} doped $LaNbO_4$ showing the change in specific heat due to the monoclinic to tetragonal phase transformation.

From the refined unit cell parameters, Figure 4-4, it was determined that Ca^{2+} doping had little influence on the structure of LaNbO$_4$, the room temperature lattice parameters are presented in Table 4-8.

		LaNbO$_4$	0.5% Ca^{2+}	1.0% Ca^{2+}	1.5% Ca^{2+}	2.0% Ca^{2+}
Space Group		I2/a	I2/a	I2/a	I2/a	I2/a
Lattice	a=	5.56(4)	5.56(1)	5.56(2)	5.56(3)	5.56(2)
Constants	b=	11.51(9)	11.52(1)	11.52(2)	11.51(8)	11.51(8)
(Å)	c=	5.20(1)	5.20(0)	5.20(1)	5.20(0)	5.20(0)
	β=	94.09(2)	94.06(4)	94.07(7)	94.09(6)	94.08(2)
$V_{\text{Unit Cell}}$ (Å^3)		332.5	332.3	332.5	332.0	332.3
Density (g/cm^3)		5.909	5.902	5.889	5.888	5.873

Table 4-8: Room temperature lattice parameters for pure and Ca^{2+} doped *m*-LaNbO$_4$.

From the room temperature lattice parameters of all compositions what stands out are the nearly identical lattice parameters. Regardless of the amount of calcium added to the structure the average volume was 332.3 Å^3 at room temperature. Changes in the lattice parameters for the calcium doped samples progressed in the same manner as for the pure LaNbO$_4$. Additionally, the unit cell volume for the monoclinic phase increased linearly until transformation and transitioned without discontinuity to the tetragonal unit cell which similarly demonstrates a linear increase. The continuous nature of the unit cell volume between the parent and product phases serves to reinforce that LaNbO$_4$ undergoes a displacive phase transformation. From Table 4-8 we know that the room temperature lattice parameters are largely identical, however from the HTXRD the changes in these values can be seen as a function of temperature. In Figure 4-14, the monoclinic *a*, *b*, and, *c* axes are plotted versus the sample temperature.

In these plots it is seen that doping with Ca^{2+} has a slight effect on how the unit cell evolves with temperature. For the monoclinic *a* and *c* axes the addition of calcium retards the convergence of these axes to what will be the tetragonal *a* axis. The slower rate of change in these parameters is not expected based on the specific heat data presented previously. Looking at the monoclinic *b* plot also shows an influence based on the Ca^{2+} doping, in this case we see a lower rate of change in the axis with heating, this is determined based on the smaller slopes of a line plotted through these points.

Taking into account the change in the thermal expansion and unit cell parameter changes in *m*-$LaNbO_4$ as a result of Ca^{2+} doping it becomes necessary to look into what effect this doping has on the phase transformation. The specific heat measurement does not indicate a change in the transformation temperature, but this could be due to how the samples were prepared for that measurement. The samples used were merely pressed into a pellet of similar dimension to the standard sample, as such they are not fully dense and this can contribute to error in the measurement. However, through HTXRD and Rietveld refinement the dimensions of the unit cell are known for discrete temperatures and this information can be used to calculate spontaneous strain in the material and further fit with the Landau 2nd order fitting parameter to determine the transformation temperature. This method has its own drawbacks; most important is that in this material, the monoclinic and tetragonal phases were present simultaneously in the diffraction patterns. Since this happens it is fair to say the transformation is not purely ferroelastic since in a ferroelastic transformation the phase change is instantaneous, an explanation for the presence of both phases is that in small enough particles transformation can occur locally before the entire sample transforms, this has been observed in nano powders.[67, 68, 69, 70] Determination of the spontaneous strain produces Figure 4-15, by fitting the data for each composition with equation (3.13) it is possible to determine the transformation temperature and the Landau critical exponent for each. The critical exponent is important in identifying what type of transformation mechanism is at play, in pure ferroelastic transformations this value is 0.5. In this study coupling between η and e^s is suggested but no direct correlation to dopant concentration was found. An increase in transformation temperature was observed for an increase in the dopant concentration; this is attributed to the creation of oxygen vacancies and will require further study to determine exactly how these defects are altering the transformation.

By fitting the spontaneous strain data, a change in transformation temperature is seen as the undoped composition transforms at 492°C and the composition with 1.5 mol% Ca^{2+} has an increased transformation temperature of 537°C. The transformation temperature, Landau exponent, and coupling coefficient for each composition are presented in Table 4-9. Although the inclusion of calcium causes an increase in the transformation temperature this is not detrimental to the use of this material for PC-SOFC devices since the current operating temperature for these devices is much higher at 900°C.[18, 23]

While the monoclinic lattice parameters show an influence based on the dopant concentration, the tetragonal lattice parameters display a more pronounced influence of calcium on the evolution of the unit cell. Figure 4-16**,** shows that the inclusion of calcium in the structure decreases the rates of change in the crystal axes compared to pure

$LaNbO_4$. For all axes we see that the sample doped with 1 mol% Ca^{2+} has the least amount of expansion, with the other concentrations being similar in expansion and less than what is observed for the pure $LaNbO_4$ structure. This is consistent with the thermal expansion behavior. Doping with 1 mol% Ca^{2+} decreases the magnitude of change in the unit cell while not decreasing amount of total amount of change in the material.

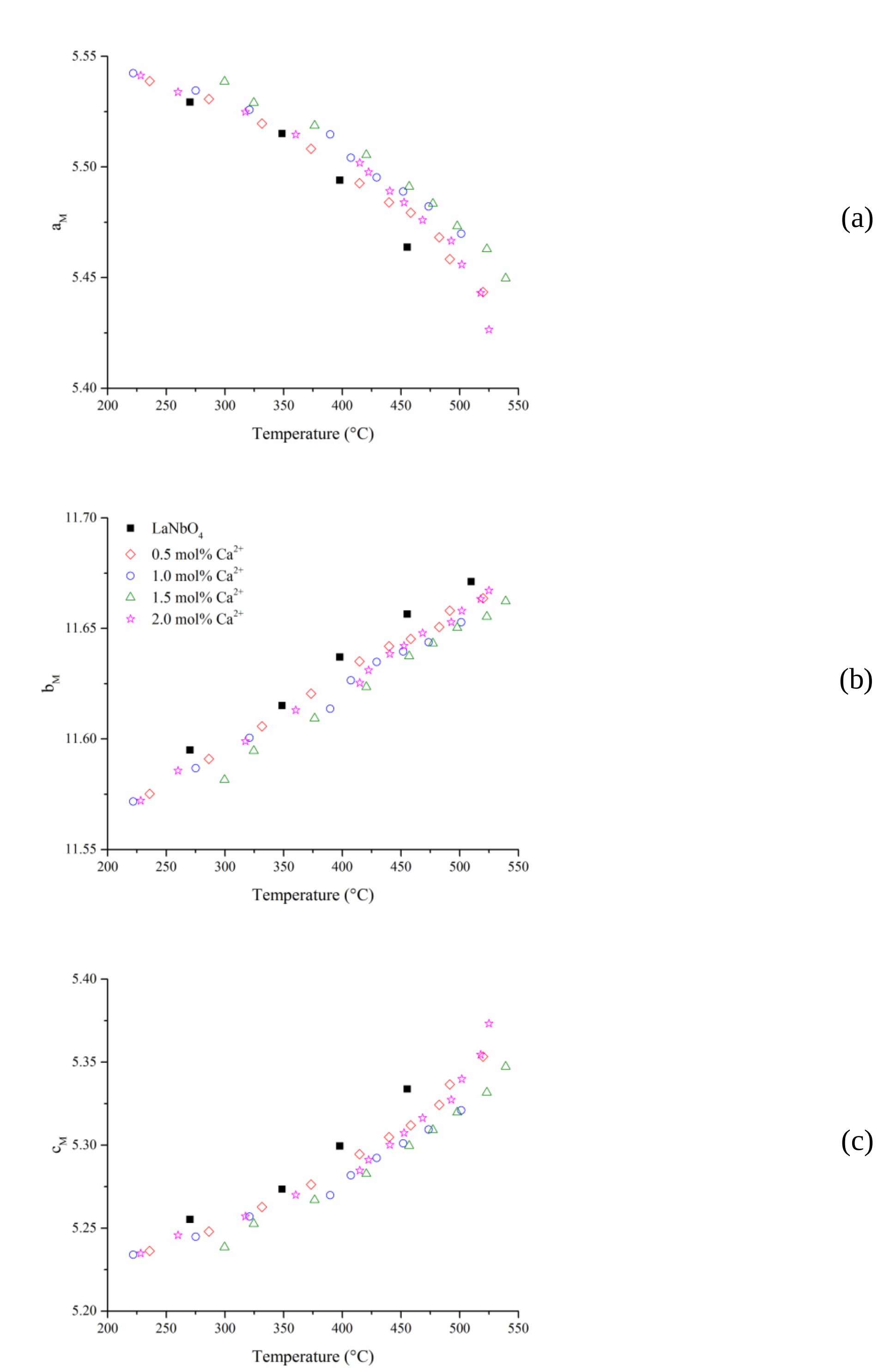

Figure 4-14: Lattice parameter change for Ca^{2+} doped *m*-LaNbO$_4$ shown as a direct comparison for each unit cell axis. (a) is the monoclinic *a* axis, (b) is the monoclinic *b* axis, and (c) is the monoclinic *c* axis.

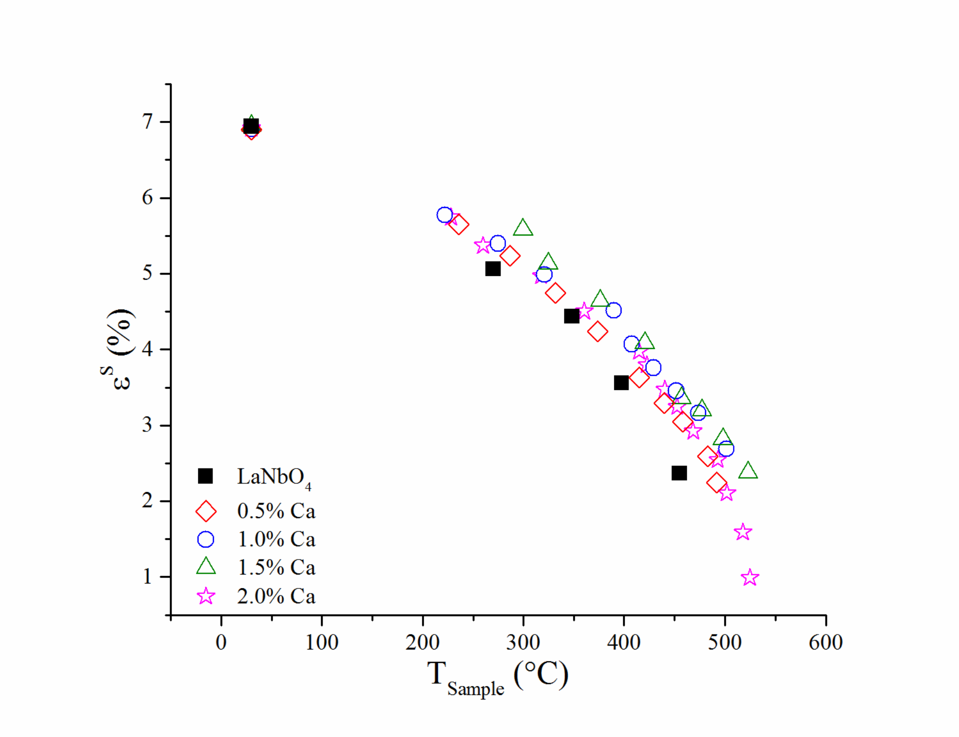

Figure 4-15: Evolution of spontaneous strain in Ca^{2+} doped *m*-$LaNbO_4$ plotted as a function of temperature.

Composition	e^s (%)	T_{Tr} (°C)	T_{Tr} std error (°C)	η	k
$LaNbO_4$	6.93	491.85	3.25	0.423	0.086
0.5 mol% Ca^{2+}	6.91	522.02	3.48	0.405	0.084
1.0 mol% Ca^{2+}	6.95	526.58	4.73	0.370	0.082
1.5 mol% Ca^{2+}	6.99	537.16	4.63	0.358	0.082
2.0 mol% Ca^{2+}	6.98	529.06	0.84	0.403	0.084

Table 4-9: Landau fitting parameters for spontaneous strain evolution in Ca^{2+} doped *m*-$LaNbO_4$.

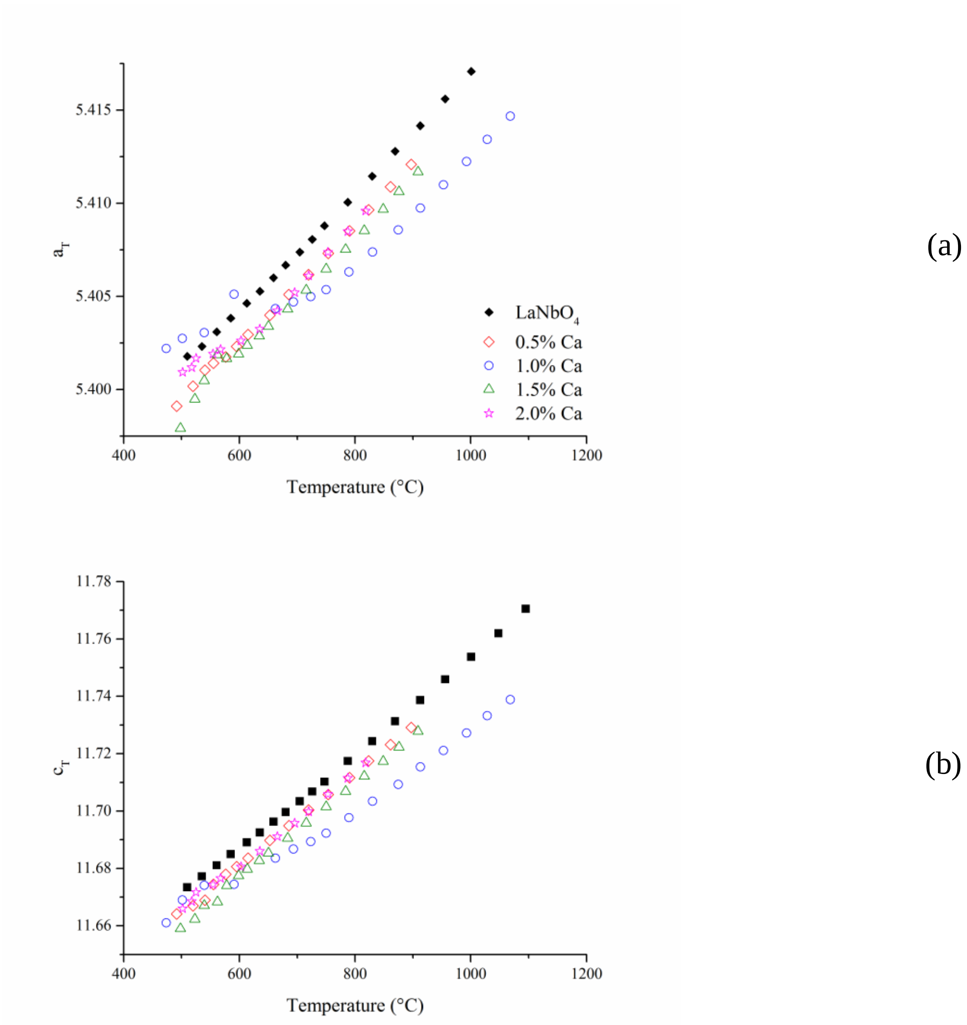

Figure 4-16: Lattice parameter change for Ca^{2+} doped *t*-LaNbO$_4$ shown as a direct comparison for each unique unit cell axis. (a) is the tetragonal *a* or *b* axis, and (b) is the tetragonal *c* axis.

4.6 Summary

Through synthesis using the stearic entrapment method compositions with dopant concentration greater than 1 mol% was achieved. The presence of a single phase was confirmed by high resolution XRD and elemental analysis using EDS. Achieving higher dopant concentrations than 1% is significant in that these compositions have the potential to further increase the proton conductivity of $LaNbO_4$ and make this system even more intriguing as a PC-SOFC material.

The monoclinic to tetragonal transformation temperature was found to increase due to calcium inclusion This occurs even though at room temperature each composition is essentially identical with negligible change in the unit cell parameters. The room temperature spontaneous strain for the pure and doped compositions with increasing dopant amount was found to be 6.93%, 6.91%, 6.95%, 6.99% and 6.98% respectively. This spontaneous strain is in agreement with literature values for $LaNbO_4$. As increasing the dopant concentration increased the transformation temperature, no change in transformation mechanism was observed based on the HTXRD datasets and the single step change in specific heat capacity at transformation.

Analysis of the thermal expansion tensor matrix and the diagonalized eigenvalues for Ca^{2+} doped $LaNbO_4$ produced new understanding about how this dopant influences the thermal expansion behavior. This was identified as a key area for this study since the change in thermal expansion coefficient between the tetragonal and monoclinic phase leads to difficulty in identifying acceptable interconnect materials. From the linear coefficient of thermal expansion determined from the average of the eigenvalues the key observation was that the 1% doped composition has the least change in linear CTE below the transformation temperature while in the tetragonal phase this same composition has the largest change in linear CTE. As the large change in the CTE between the two phases has been identified as a processing challenge for PC-SOFC devices the extreme change in CTE of 1% Ca^{2+} *t*-$LaNbO_4$ could be a limiting factor in the identification of interconnect materials.

CHAPTER 5.

EFFECT OF Zr^{4+} ON THE $LaNbO_4$ PHASE TRANSFORMATION

5.1 Introduction

The objective of this study was to investigate the effect of zirconium doping on the thermo-physical properties of $LaNbO_4$. The primary focus was on evaluating the influence of dopant ion concentration on the crystal structure and phase transformation characteristics of $LaNbO_4$. In addition, any change in thermal expansion property and anisotropy was also examined. The changes in ionic radii for the cations involved in this study are important to notice as the change in size will determine how the dopant can be accommodated in the $LaNbO_4$ lattice. Zirconium is expected to substitute equally across both the La^{3+} and Nb^{5+} sites and as a result the doped compositon maintains charge balance. In $LaNbO_4$, lanthanum is understood to assume a VIII fold coordination, while niobium is in IV fold coordination.[71] In the similar $YTaO_4$ system yttrium is in VIII fold coordination and tantalum is in IV fold coordination. Zirconium prefers to be in a VIII fold coordination,[72] which should allow for direct substitution on the rare earth site, however, with the Nb^{5+} and Ta^{5+} sites in IV fold coordination it will be important to consider the effects of different coordination preferences at this position. The size of the cation ionic radius is also important, accordingly these values are; 1.160, 1.019, 0.84, 0.48, and 0.74 Å respectively for La^{3+}, Y^{3+}, Ta^{5+}, Nb^{5+}, and Zr^{4+} in the stated coordination configurations.[72] For $YTaO_4$ this means the average cation radius is 0.87 Å where in $LaNbO_4$ the average radius is 0.82 Å, in both cases the Zr^{4+} ionic radius is smaller than the average. In order to accommodate the Zr^{4+} ion there must be an VIII fold coordination site available, in the case of Nb^{5+} and Ta^{5+} distortion in the lattice is necessary to substitute on this position.

5.2 Effect of Zr^{4+} on $m \leftrightarrow t$ phase transformation

The addition of Zr^{4+} to the $LaNbO_4$ lattice demonstrated negligible effect on the T_{tr} as determined by specific heat measurements, Figure 5-1. The T_{tr} values determined from specific heat measurements show, that regardless of the amount of dopant in the lattice the average transformation temperature was 500.4°C. Temperatures corresponding to the onset of the thermodynamic event while heating, were recorded as T_{tr}, and were 497.9°C, 497.9°C, 504.0°C, 498.9°C, 503.5°C, and 500.2°C for doped compositions with increasing Zr^{4+} content. The specific heat capacity experiments used a sapphire standard disc of similar dimensions to the pressed pellets of the synthesized powders. The small changes in the transformation temperatures are attributed to instrumental error, but imply that structural changes in the crystal are similar for each composition.

The effect of Zr^{4+} dopant ion on the $m \rightarrow t$ transformation in $LaNbO_4$ was investigated by HTXRD. Diffraction patterns were acquired at discrete temperature steps while heating each powder sample from room temperature to around 1050°C. Each HTXRD pattern was subsequently analyzed to determine the crystalline phase composition and crystal structure of present phases at that temperature. The crystal structure was characterized using the Rietveld method, for this ICSD#262599, ICSD#81618, and ICSD#18109 were used for *m*-, *t*-$LaNbO_4$, and *m*-ZrO_2 respectively. The $LaNbO_4$ phases were refined as pure phases. The unit cell parameters for the Zr^{4+} doped $LaNbO_4$ samples are plotted as a function of temperature in Figure 5-2. In the monoclinic phase, the lattice parameter a (denoted as 'a_M') decreases and c (denoted as 'c_M') increases nonlinearly with temperature converging into the lattice parameter a (denoted as 'a_T') of the tetragonal phase at the T_{tr}. Following transformation, the a_T parameter increases linearly with temperature. The monoclinic b (denoted as 'b_M') lattice parameter, on the other hand increases linearly to coincide with the tetragonal c (denoted as 'c_T') lattice parameter at transition. The difference in the rate of increase of b_M and c_T with temperature is distinct. The unit cell volume (i.e. $V_{Unit\ Cell}$) increases linearly with temperature, for both the monoclinic and the tetragonal phases for pure and doped $LaNbO_4$ samples. More importantly, the transition occurs without any discontinuity in $V_{\mathrm{Unit\ Cell}}$ and is therefore understood to be continuous. A change in the slope of the $V_{Unit\ Cell}$ with temperature is however, observed across the transition from the monoclinic to the tetragonal phase. These observations are consistent with earlier reports.[29, 33]

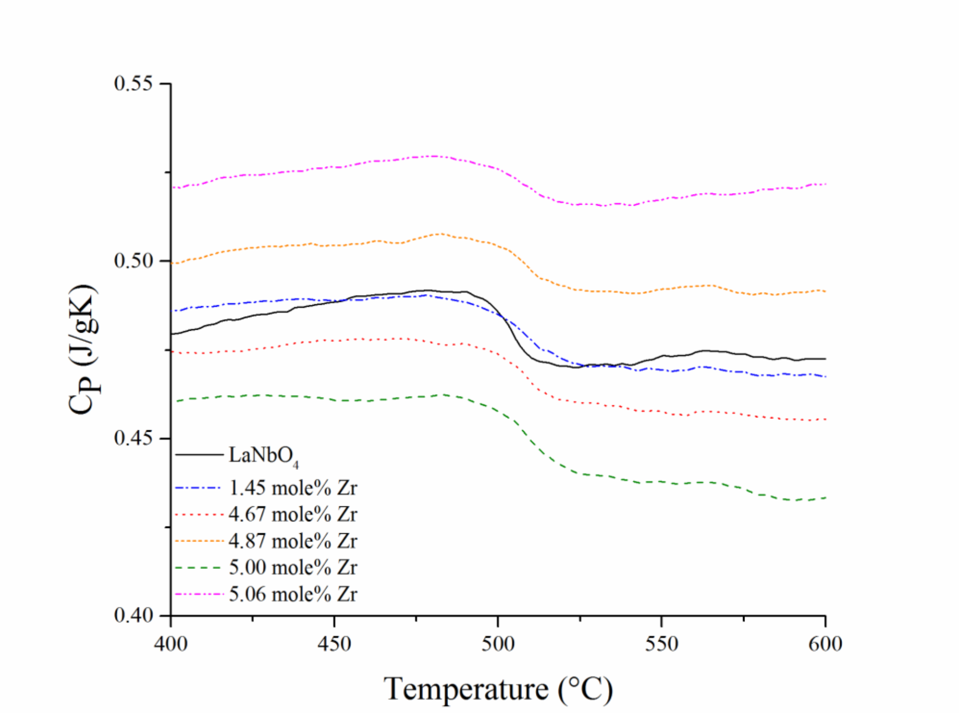

Figure 5-1: Specific heat data for pure and Zr^{4+} doped $LaNbO_4$ showing the change in specific heat due to the monoclinic to tetragonal phase transformation.

Sarin *et al.* (2014) had highlighted the limitations in determining the T_{tr} of rare-earth niobate systems by HTXRD.[33] As Landau theory can accurately describe the primary physical features of ferroelastic transformation, it is possible to determine the T_{tr} by fitting the expression for the Landau order parameter, which is a function of T_{tr}, to an independently determined physical property. Spontaneous strain (ε^s) is one such property,[59] and is essentially a measure of strain in the lattice of the transformed phase (*m*-$LaNbO_4$) when compared to the hypothetical parent phase (*t*-$LaNbO_4$) at the same temperature. The procedure to determine ε^s in crystal structure has been detailed in the literature.[33, 47, 59, 73] The ε^s for each synthesized composition were determined to be 6.93%, 6.99%, 6.92%, 6.91%, 6.92%, and, 6.92% at room temperature, for samples with

0, 1.45, 4.67, 4.87, 5.00, and, 5.06 mol% Zr^{4+} ion concentrations, respectively. Inclusion of Zr^{4+} in the $LaNbO_4$ structure did not influence the spontaneous strain in the *m*-$LaNbO_4$ phase at room temperatures. Figure 5-3 presents the change in ε^s with temperature (T) for all compositions. The T_{tr} was determined for each composition by equation (3.13).

The resulting values for k, T_{tr}, and η are given in Table 5-1. The T_{tr} values determined by the Landau order parameter fitting approach are consistent with those measured by the specific heat capacity (C_p) method. Notable is the value of the Landau critical exponent η which is characteristically ½ for pure ferroelastic transformations. The η values determined for all the $LaNbO_4$ compositions in this study suggest coupling between the Landau order parameter and the spontaneous strain ε^s, although no trend with increasing Zr^{4+} ion concentration in the $LaNbO_4$ structure was evident.

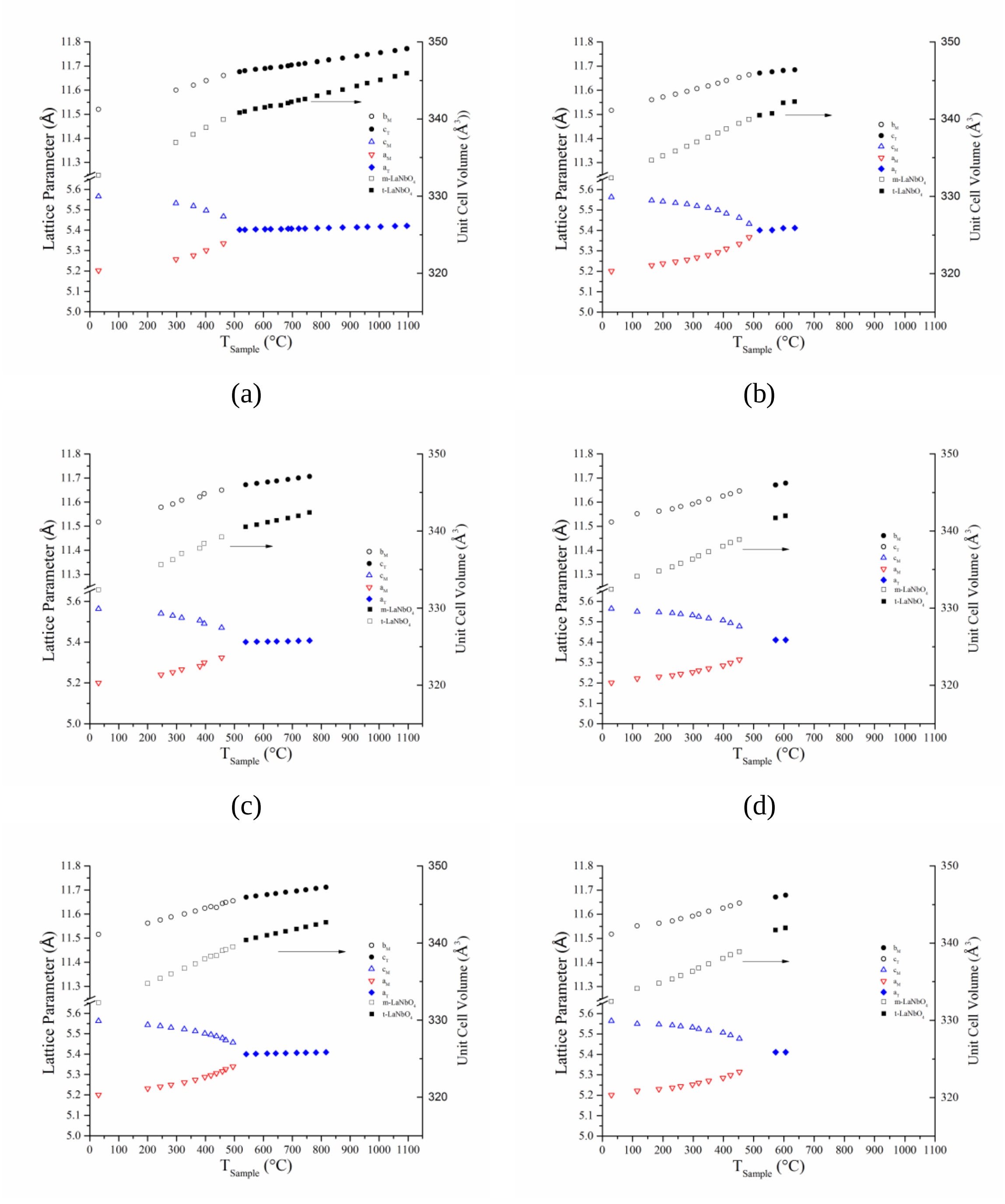

(a) (b) (c) (d) (e) (f)

Figure 5-2: Evolution of unit cell parameters for monoclinic and tetragonal $LaNbO_4$ doped with (a) pure $LaNbO_4$, (b) 1.45 mol%, (c) 4.67 mol%, (d) 4.87 mol%, (e) 5.0 mol%, and (f) 5.06 mol% Zr^{4+}.

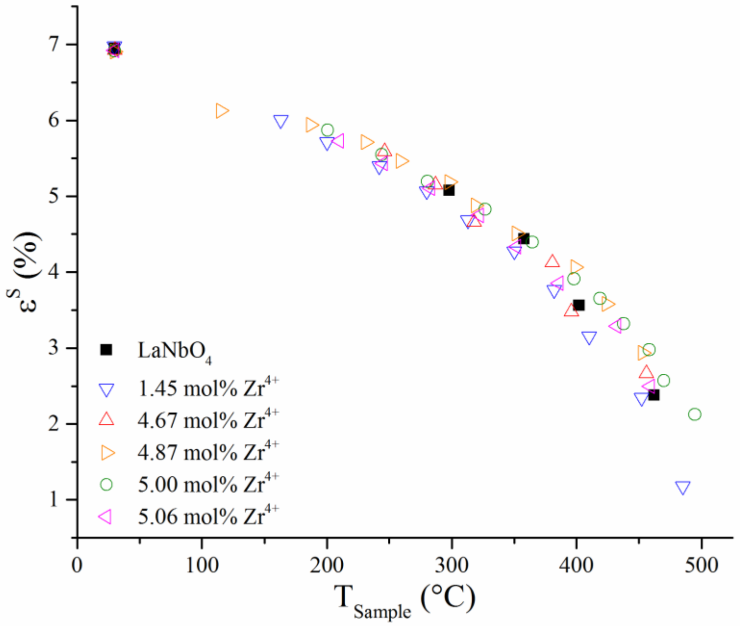

Figure 5-3: Evolution of spontaneous strain in Zr^{4+} doped *m*-LaNbO4 plotted as a function of temperature.

Composition	e^s (%)	T_{Tr} (°C)	T_{Tr} std error (°C)	η	k
$LaNbO_4$	6.93	491.85	3.25	0.423	0.086
1.45 mol% Zr^{4+}	6.99	492.40	1.27	0.435	0.087
4.67 mol% Zr^{4+}	6.92	485.72	4.11	0.352	0.083
4.87 mol% Zr^{4+}	6.91	492.43	5.77	0.344	0.082
5.00 mol% Zr^{4+}	6.92	509.94	4.47	0.385	0.084
5.06 mol% Zr^{4+}	6.92	492.39	2.99	0.391	0.085

Table 5-1: Landau fitting parameters for spontaneous strain evolution in Zr^{4+} doped *m*-$LaNbO_4$.

As stabilization of *t*-$LaNbO_4$ phase at a lower temperature was one of the primary motivations for this study, it is important to understand why inclusion of Zr^{4+} ion in the $LaNbO_4$ structure did not alter the T_{tr}. In the rare-earth ortho-niobates and -tantalates, the T_{tr} increases with a decrease in the ionic radii of the rare-earth cation, or $V_{Unit\ Cell}$ of the crystal structure.[30, 74] In a recent study, Sarin *et al.* have concluded that the size of the rare-earth cation is the key parameter which determines the T_{tr} in rare-earth niobates, while the Nb^{5+} cation defines the mechanism of the ferroelastic transition which involves distortion of the NbO_4 tetrahedron. Accordingly, partial substitution of the rare earth cation with an isovalent cation of different ionic size may allow control of the T_{tr} by modifying the effective radii at the rare-earth cation site in the structure. When doping with an aliovalent cation such as Zr^{4+}, the outcome may be very different. As seen in the case of $YTaO_4$, the dopant cation Zr^{4+} was distributed equally between the rare-earth cation and Ta^{5+} sites. The $V_{Unit\ Cell}$ decreased with increasing Zr^{4+} content, but the T_{tr} was also seen to decrease dramatically from above 1400°C to around 800°C. Inclusion of Zr^{4+} cation at the Y^{3+} site would have certainly decreased the average size of the Y^{3+} site, however the decrease in T_{tr} was most likely due to the incorporation of Zr^{4+} at the Ta site. In the present study, inclusion of Zr^{4+} ion in the $LaNbO_4$ structure had no impact on either the T_{tr} or on the $V_{Unit\ Cell}$. While substitution of La^{3+} by Zr^{4+} in the structure may not be limited by size constraints, Zr^{4+} most likely cannot replace Nb^{5+} at a tetrahedral site. Charge balance requirements may mandate positioning of the dopant Zr^{4+} ion at interstitial sites, if structural rearrangements to form an eight/seven-fold coordination site is not possible (e.g. pairing of two adjacent Nb tetrahedral). One important condition that appears to be paramount is the availability of eight-fold coordination sites for Zr^{4+} to be accommodated in the crystal structure.

5.3 Effect of Zr^{4+} on thermal expansion behavior of *m*-$LaNbO_4$

Due to the orthogonality of the crystallographic axes in the tetragonal system, the α_{11}, α_{22}, and α_{33} are also the principal coefficients (λ_i) of the CTE tensor. However, for the monoclinic structures, the CTE tensor has to be diagonalized to yield the eigenvalues or principal coefficients λ_1, λ_2 and λ_3, which represent the thermal expansion coefficient values in three mutually perpendicular directions. All eigenvalues for the *t*-$LaNbO_4$ phases were positive, thereby indicating expansion in all directions. In contrast, one of the eigenvalues was always negative for the *m*-$LaNbO_4$ phases, Figure 5-4. Therefore, the monoclinic structure expands in two directions and contracts along the third direction upon heating. The directions of maximum thermal expansion and contraction (i.e. negative value of principal coefficient) were confined in the *ac* plane of the *m*-phase, and were not oriented along either *a* or *c* crystallographic axes. The monoclinic structure expanded linearly along the *b* direction and in volume. Increasing the Zr^{4+} dopant ion concentration did lower the α_{avg} values for the *m*–$LaNbO_4$ phase, particularly closer to the T_{tr}. For example, α_{avg} measured for the *m*–$LaNbO_4$ phase in the 5.06 mol% doped sample at 500°C is 1.95 x 10^{-5} /°C, which is ~13% smaller than the α_{avg} for the pure m–$LaNbO_4$ phase at the same temperature. Generally, the α_{avg} and *A* increased with temperature, Table 5-2, for all the *m*-$LaNbO_4$ phases until the structure transformed to the t- phase. In comparison, the *t*-$LaNbO_4$ phases had significantly lower α_{avg} and *A* coefficient values, and both these parameters decreased further with increase in temperature beyond T_{tr}. As α_{avg} is the principal coefficients (λ_i) mean of the CTE tensor, and with no observable trends in λ_i with dopant ion concentration, α_{avg} was not considered as a fundamental parameter to gauge the effect of Zr^{4+} doping on thermal expansion properties of $LaNbO_4$.

From the orientation relationship between the crystallographic axes as well as the CTE tensor, the indices for the ZTE plane were determined. The results for *m*-$LaNbO_4$ are presented in Figure 5-5, which shows that the ZTE plane largely independent of Zr^{4+} concentration. Although the miller indices are irrational, the relative invariance in the ZTE plane, both across compositions as well as with temperature, is an interesting observation, and could be a useful method for comparing related crystal structures. Based on the findings in this study, it was concluded that overall, inclusion of Zr^{4+} in the $LaNbO_4$ structure did not have a significant effect on the thermal expansion properties.

T	**1.45% Zr^{4+}**			**4.67% Zr^{4+}**			**4.87% Zr^{4+}**			**5.00% Zr^{4+}**			**5.06% Zr^{4+}**		
°C	**A**	**α_{avg}** (10^{-5} /°C)	**β** (10^{-5} /°C)	**A**	**α_{avg}** (10^{-5} /°C)	**β** (10^{-5} /°C)	**A**	**α_{avg}** (10^{-5} /°C)	**β** (10^{-5} /°C)	**A**	**α_{avg}** (10^{-5} /°C)	**β** (10^{-5} /°C)	**A**	**α_{avg}** (10^{-5} /°C)	**β** (10^{-5} /°C)
200	1.59	1.59	4.78	1.60	1.48	4.44	1.40	1.24	3.73	1.55	1.44	4.33	1.32	1.51	4.53
225	1.83	1.58	4.73	1.78	1.47	4.41	1.28	0.46	1.37	1.69	1.46	4.38	1.58	1.43	4.28
250	2.07	1.56	4.69	1.96	1.47	4.41	1.39	1.02	3.06	1.82	1.48	4.44	1.65	1.54	4.61
275	2.30	1.56	4.68	2.13	1.47	4.40	1.55	0.99	2.96	1.95	1.51	4.52	1.86	1.51	4.54
300	2.52	1.56	4.69	2.30	1.47	4.40	1.37	0.95	2.84	2.07	1.54	4.62	2.09	1.46	4.38
325	2.72	1.58	4.73	2.45	1.48	4.43	1.05	0.85	2.55	2.18	1.57	4.72	2.23	1.45	4.36
350	2.90	1.60	4.79	2.59	1.49	4.48	0.66	0.66	1.97	2.26	1.62	4.85	2.43	1.53	4.59
375	3.05	1.63	4.89	2.71	1.52	4.55	0.74	0.50	1.49	2.36	1.65	4.94	2.52	1.60	4.81
400	3.17	1.68	5.03	2.82	1.55	4.65	0.65	0.56	1.68	2.35	1.70	5.10	2.62	1.64	4.93
425	3.27	1.73	5.20	2.91	1.59	4.76	1.02	0.75	2.26	2.43	1.75	5.26	2.72	1.68	5.04
450	3.33	1.80	5.41	2.98	1.63	4.90	1.54	1.00	2.99	2.50	1.84	5.51	2.80	1.73	5.19
475	3.37	1.89	5.67	3.02	1.69	5.07				2.52	1.88	5.65	2.87	1.79	5.38
500	3.37	1.99	5.97	3.05	1.75	5.26				2.54	1.95	5.86	2.91	1.86	5.59

Table 5-2: Aspherism index, average thermal expansion and bulk thermal expansion values for Zr^{4+} doped $LaNbO_4$.

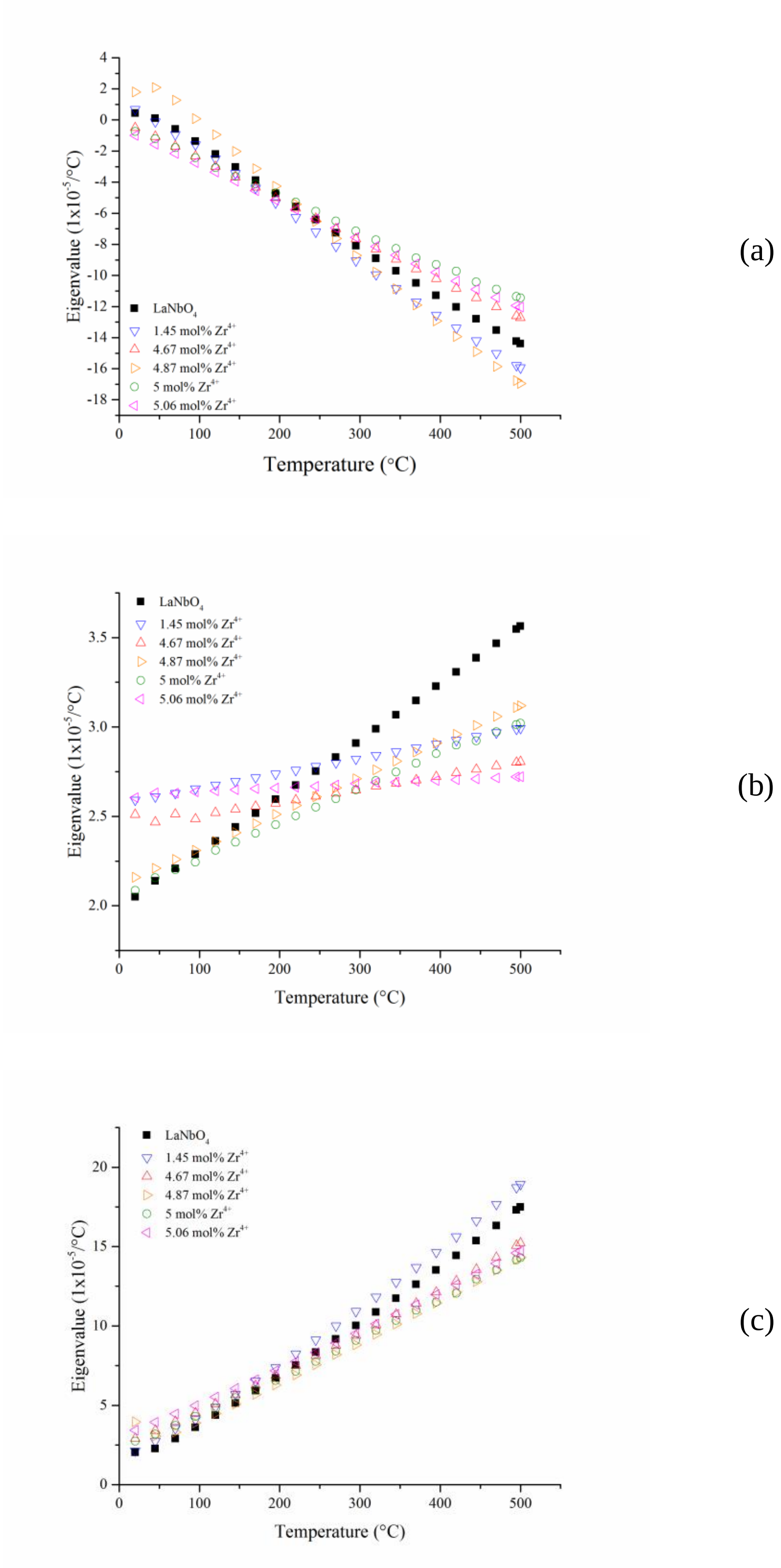

Figure 5-4: Eigenvalues of thermal expansion in the monoclinic phase for Zr^{4+} doped $LaNbO_4$.

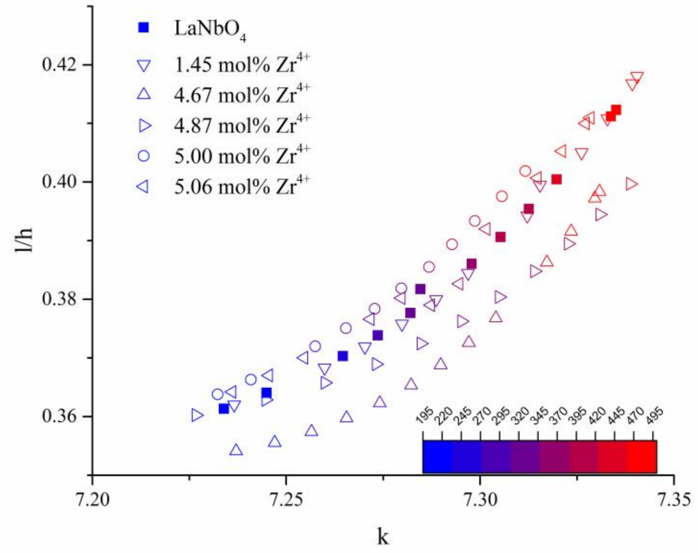

Figure 5-5: Plane of zero CTE miller indices in 25°C steps from 195°C to 495°C.

5.4 Solubility of Zr^{4+} in $LaNbO_4$

From analysis of the phase transformation by specific heat and through Landau fitting of the HTXRD data and of the thermal expansion behavior of the Zr^{4+} doped materials the solubility of Zr^{4+} in $LaNbO_4$ must be questioned. The phase diagram, Figure 5-6, for this system indicates that ZrO_2 is soluble in $LaNbO_4$. However, in this study it was determined that a limit of approximately 5 mol% exists, with compositions doped with larger amounts of Zr^{4+} exhibiting large amounts of ZrO_2 phase in the XRD datasets collected at synchrotron facilities, Figure 5-7. It should be noted that the composition with 5 mol% Zr^{4+} did not show a separate ZrO_2 phase in the diffraction data. The absence of a ZrO_2 phase in these data sets is unlikely to be attributed to the detection limit since synchrotron sources are known to have sufficient sensitivity to detect much lower phase fractions than 5% and as such the approach taken to determine composition by mass balance is justified.[75]

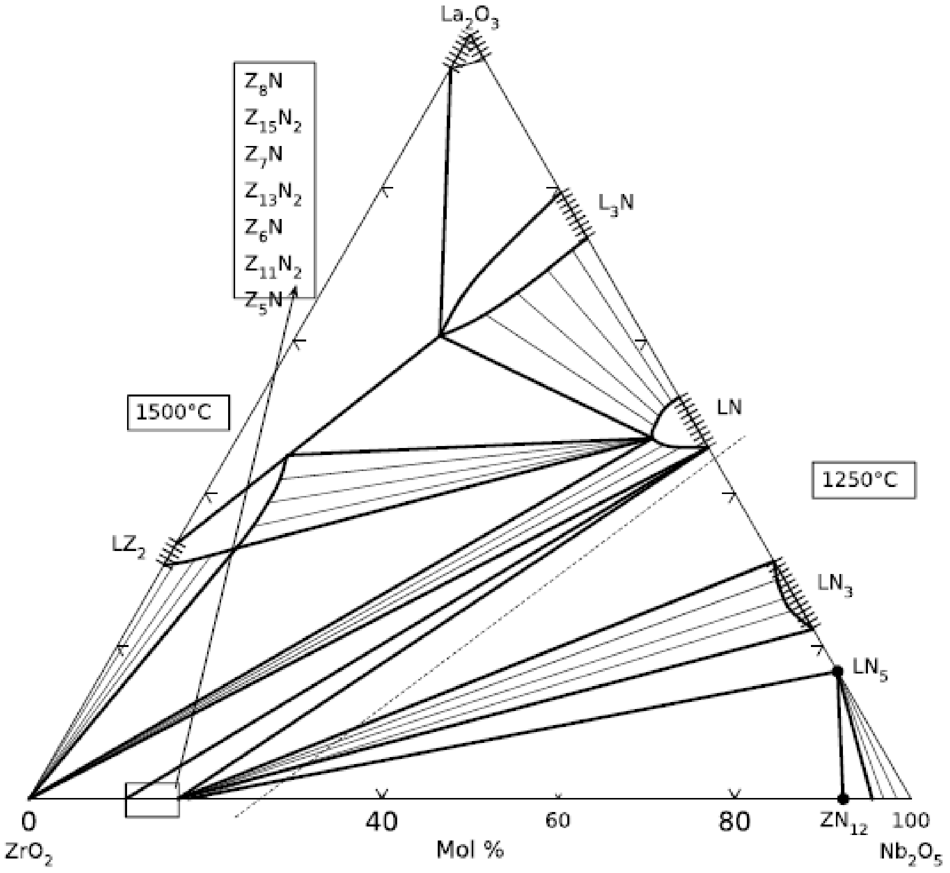

Figure 5-6: Phase diagram for ZrO_2-La_2O_3-Nb_2O_5 indicating solubility of ZrO_2 in the $LaNbO_4$ phase.[76]

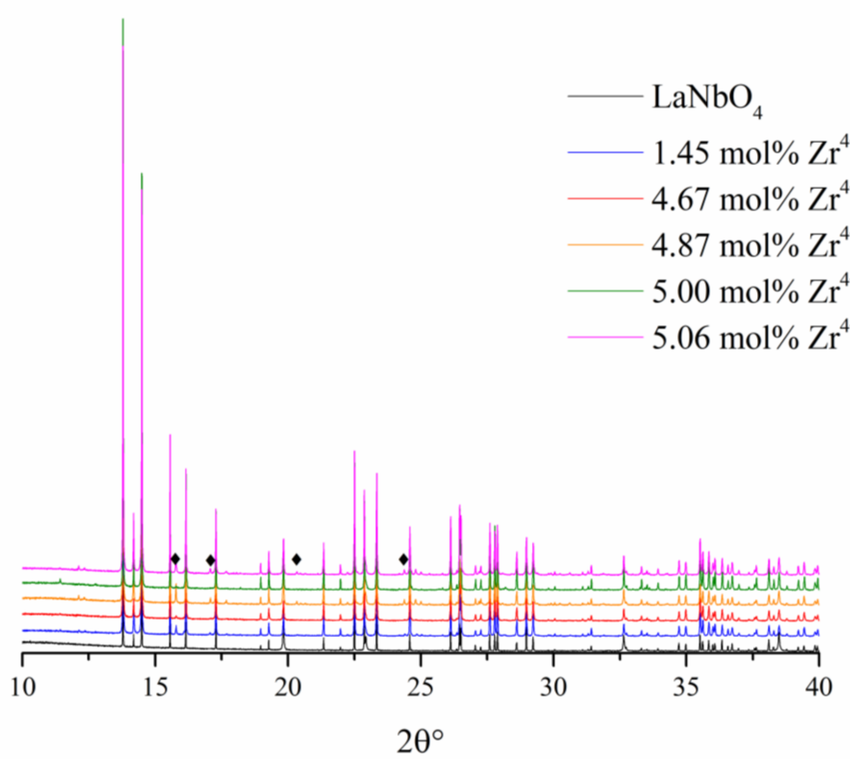

Figure 5-7: Room temperature XRD datasets for Zr^{4+} doped $LaNbO_4$, ♦ indicates major peaks for ZrO_2.

Since this phase diagram indicates ZrO_2 solubility it is important to look at how these samples were synthesized. The stearic entrapment method has been used to produce high quality single phase powders due to atomic level mixing of the precursor materials rather than solid state diffusion of mixed oxides. The above phase diagram was produced mixing proportional amounts of the three oxides and sintering pressed pellets then grinding the pellets to produce the powders. In that approach diffusion is the mechanism at work and could lead to inhomogeneous phase powders. Stearic entrapment is known to prevent inhomogeneity in the produced powders; however, if the precursor materials are not sufficiently soluble then it is not possible to guarantee a phase pure final powder. In this study the Zr^{4+} precursor of $ZrO(NO_3)_2$ was not highly soluble in ethanol which was chosen for the high solubility of $NbCl_5$. As such $ZrO(NO_3)_2$ was first dissolved in DI water before being added to the synthesis solution. With the required extra processing it is possible that Zr^{4+} ions separated from the rest of the solute and in turn lead to the secondary ZrO_2 phase in the final powders. As more and more zirconium was added to the solute with the low solubility it is logical that a greater portion of final powder would be ZrO_2 as was seen in the refined phase fractions of the room temperature XRD datasets. The presence of ZrO_2 in the microstructure was not excessive as confirmed by EDS. Two pellets of the 5 mol% doped powder were pressed and sintered for the EDS analysis, one pellet was made from powder that had been calcined at 1200°C while the second pellet was made from powder calcined at 1500°C. Significant differences in the pellets were observed regarding grain size as the pellet made from the 1500°C powder demonstrated much larger grains, Figure 5-8.

Also of importance is the presence of Zr^{4+} rich regions in the map of the pellet made from powder calcined at the higher temperature. This indicates that while the powder was held at 1500°C for an extended amount of time Zr^{4+} could diffuse to localized regions resulting in the formation of ZrO_2 in the powder. The formation of ZrO_2 has been attributed to the thermal processing of the powders and not to the stearic entrapment method of synthesis, further study investigation to optimization of the thermal processing and source of Zr^{4+} are needed to fully understand this system.

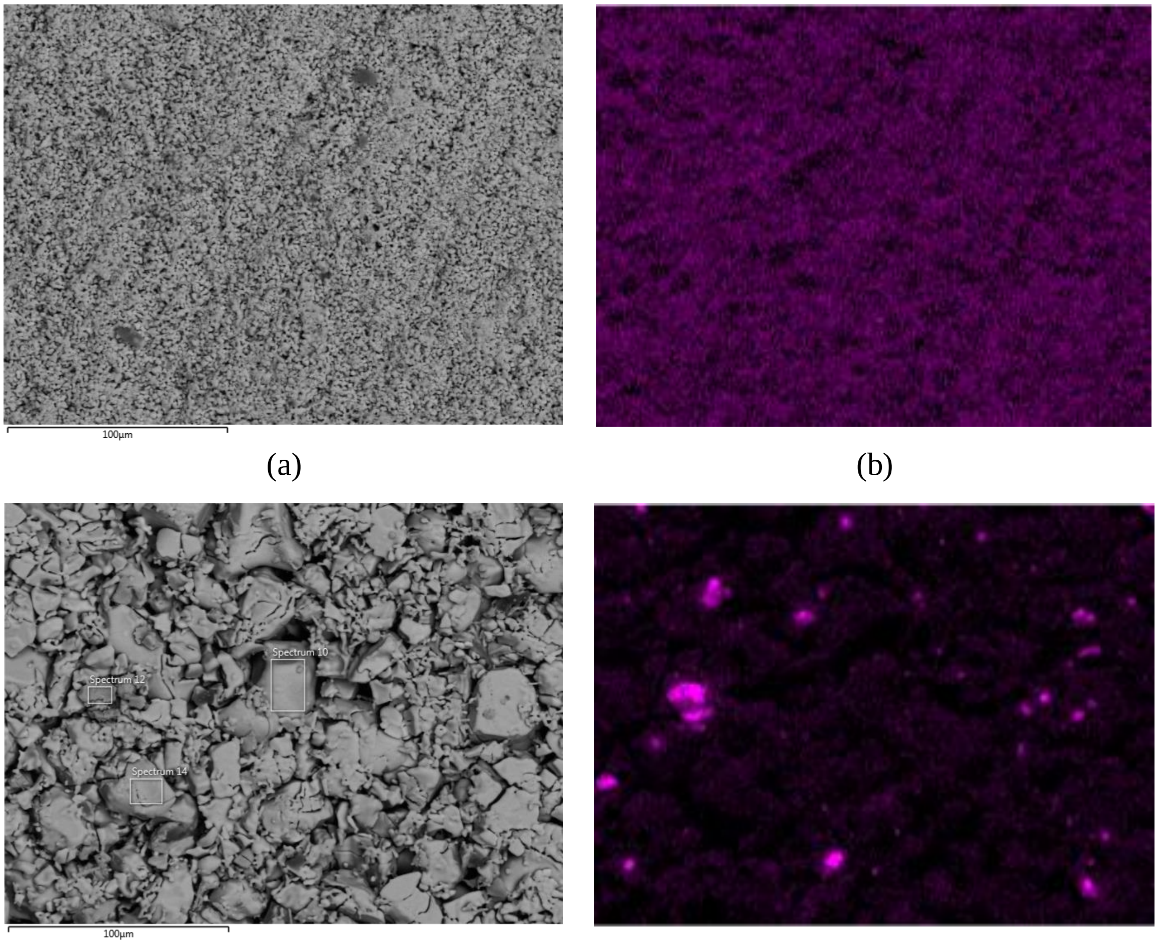

(a) (b)

(c) (d)

Figure 5-8: Zr^{4+} elemental map for 5mol% doped $LaNbO_4$ on sintered pellets at 500x magnification, scale bar is 100μm. Micrographs (a) and (b) are for 1200°C calcined powder, (c) and (d) are for 1500°C calcined powder.

The observation of *m*-ZrO_2 phase in the sample powders doped for greater than 5 mol% Zr^{4+} can be explained by either insolubility or partial solubility of the Zr^{4+} ion in $LaNbO_4$ structure. To resolve this, the XRD patterns collected at room temperatures were quantitatively analyzed for crystalline phase composition by the Rietveld method.[55] The crystal structures of the component phases, i.e. *m*-ZrO_2 and *m*-$LaNbO_4$ were also refined. The dopant ion concentration in $LaNbO_4$ was calculated by subtracting the experimentally measured weight percent of the *m*-ZrO_2 from the expected weight percent of ZrO_2 if no Zr^{4+} was dissolved in the $LaNbO_4$ structure. The difference was then converted into mol% of Zr^{4+} ion that dissolved in the $LaNbO_4$ phase. Following this procedure, the Zr^{4+} ion concentration in the doped $LaNbO_4$ samples was determined as 1.45, 4.67, 4.87, 5.00, and, 5.06 mol% Zr^{4+} for initially targeted compositions with 20, 10, 30, 5, and, 40 mol% Zr^{4+} in $LaNbO_4$, respectively. The difference in the target and actual compositions, and the observation that values leveled off around 5 mol% is indicative of reaching a solubility limit of Zr^{4+} in the $LaNbO_4$ structure. Shian *et al.* had shown that $YTaO_4$, an isostructural compound, could be doped with 20 mol% Zr^{4+} ion concentrations,[47] which is significantly higher than the 5 mol% solubility limit for Zr^{4+} ion in $LaNbO_4$ structure. Our conclusions are based on the observation that the unit cell parameters of *m*-$LaNbO_4$ phase at room temperature are not altered by the dopant Zr^{4+} ion, however, a factor of four in solubility difference of Zr^{4+} between the two isostructural compounds $YTaO_4$ and $LaNbO_4$ is very significant. Furthermore, the unit cell volume for *m*-$LaNbO_4$ is ~332 $Å^3$, which is approximately 14% larger than $YTaO_4$ (292 $Å^3$). Lattice constants of the pure and the doped $LaNbO_4$ compositions at room temperature are included in Table 5-3**.** Increasing the concentration of Zr^{4+} ion in the $LaNbO_4$ structure, from 0 mol% to 5 mol% resulted in negligible change in unit cell volume and lattice parameters. This is also in contrast to the findings for $YTaO_4$ where lattice constants *'a'*, *'b'* and *'β'*, and unit cell volume had all decreased with increasing concentration of dopant Zr^{4+} ion in the structure.[47]

		$LaNbO_4$	1.45% Zr^4	4.67% Zr^{4+}	4.87% Zr^{4+}	5.00% Zr^{4+}	5.06% Zr^{4+}
Space Group		I2/a	I2/a	I2/a	I2/a	I2/a	I2/a
Lattice	a=	5.20(2)	5.20(1)	5.20(1)	5.20(1)	5.20(0)	5.20(1)
Constants	b=	11.52(0)	11.51(7)	11.51(7)	11.51(8)	11.51(6)	11.51(8)
(Å)	c=	5.56(5)	5.56(3)	5.56(3)	5.56(3)	5.56(2)	5.56(3)
	β=	94.09(3)	94.08(9)	94.08(8)	94.09(4)	94.08(5)	94.09(2)
$V_{\text{Unit Cell}}$ (Å^3)		332.7	332.4	332.4	332.4	332.3	332.4

Table 5-3: Room temperature unit cell parameters for Zr^{4+} doped $LaNbO_4$.

A possible explanation for the above observations lies in the coordination preferences of the dopant cation, and the ability of the host structure to meet them. The Zr^{4+} ion usually prefers eight-fold coordination as it does in cubic and tetragonal zirconia[77] but it can also adopt a seven-fold coordination as it does in monoclinic zirconia,[78] for instance. It is not reported to adopt a tetrahedral coordination. In scheelite as well as in fergusonite structures of rare-earth ortho-niobates and -tantalates, the trivalent rare-earth ions have an eight-fold coordination in a deformed polyhedron and the pentavalent ions, Nb^{5+} and Ta^{5+}, have tetrahedral coordination.[24] One important difference between the rare earth ortho-niobates and -tantalates is that the Ta atoms are essentially tetrahedrally coordinated with a second, relatively larger tetrahedron in the immediate vicinity, forming a distorted cube.[24] According to Shian *et al.* (2014), it is likely that Zr^{4+} ions are substituted in pairs for both Y and Ta ions within the $YTaO_4$ unit cell.[47] While the Y site has eight-fold coordination, the Ta site can also present an eight-fold coordination for Zr^{4+} dopant cation by pairing two adjacent tetragonal sites. This may explain the unusually high solubility of Zr^{4+} in $YTaO_4$. Such structural readjustment may not be possible around the Nb cation in the $LaNbO_4$, thereby resulting in very low solubility of Zr^{4+} ion in the structure, perhaps with the Zr^{4+} dopant ion located at an interstitial site.

The above explanation is also consistent with the observed decrease in the lattice constants and unit cell volume in $YTaO_4$ with incremental substitution by Zr^{4+} ions. The ionic radii of Y^{3+}, Zr^{4+} and Ta^{5+} are reported to be 1.019, 0.84 and 0.74 Å, respectively.[77] Since the average of the ionic radii of Y^{3+} and Ta^{5+} is 0.87 Å and differs by only 3.5% from that of the Zr^{4+} ion, the substitution of both Y^{3+} and Ta^{5+} sites by a pair of Zr^{4+} ions was expected to decrease the unit cell volume.[47] In the case of $LaNbO_4$, the absence of any structural rearrangements to accommodate the dopant Zr^{4+} ion can explain the negligible change in lattice constants of the unit cell observed in this study. From the lack of structural rearrangement due to Zr^{4+} doping in $LaNbO_4$ serious questions arise. First, is the phase diagram correct? If the reality is that ZrO_2 is insoluble in $LaNbO_4$ then the phase diagram needs to be revisited however, this is a significant undertaking and outside the scope of this study. However, it is possible that ZrO_2 is soluble and that the $LaNbO_4$ lattice is able to accommodate a certain level of doping without lattice rearrangement. This theory is supported by the changes in thermal expansion due to Zr^{4+} doping and Rietveld refinement of the HTXRD datasets using the pure $LaNbO_4$ structure. Additionally, in the preceding chapter concerning doping of $LaNbO_4$ with Ca^{2+} there was no change in the room temperature lattice parameters yet it is known that the structure can accommodate this dopant.

5.5 Summary

The $m \rightarrow t$ ferroelastic phase transformation in $LaNbO_4$ was independent of Zr^{4+} dopant concentration. The solubility of Zr^{4+} in $LaNbO_4$ as well as the effect of Zr^{4+} on the phase transformation and thermal expansion properties were studied using high temperature X-ray diffraction and specific heat methods. Unlike the case of $YTaO_4$, an isostructural compound, the Zr^{4+} ion was relatively insoluble in $LaNbO_4$ and a solubility limit of ~5 mol% was determined in this study. The crystal structures of both the *m*- and *t*- $LaNbO_4$ phases were unaffected by the inclusion of Zr^{4+} over the entire temperature range investigated in this work. Consequently, the spontaneous strain in the room temperature *m*-$LaNbO_4$ phase was invariant and determined as 6.93%, 6.99%, 6.92%, 6.91%, 6.92%, and, 6.92% for 0, 1.45, 4.67, 4.87, 5.0, and, 5.06 mol% Zr^{4+} dopant concentrations. Doping with Zr^{4+} had negligible effect on the phase transformation and thermal expansion properties of $LaNbO_4$. Specific heat measurement experiments showed a step change in the specific heat capacity, characteristic of a second order phase transition, within a narrow temperature range (±3°C) for all compositions. Based on careful analysis of the CTE tensor elements and the relative invariance of plane of zero thermal expansion, it was concluded that inclusion of Zr^{4+} in the $LaNbO_4$ structure did not have a significant effect on the thermal expansion properties. The presence of Zr^{4+} was not confirmed in this study, however based on the analysis and the phase diagram it is believed to have been incorporated into the lattice.

CHAPTER 6.

CONCLUSIONS AND RECOMMENDATIONS

6.1 Effect of Ca^{2+} doping

Through synthesis using the stearic entrapment method compositions with dopant concentration greater than 1 mol% was achieved. The presence of a single phase was confirmed by high resolution XRD and elemental analysis using EDS. Achieving higher dopant concentrations than 1% is significant in that these compositions have the potential to further increase the proton conductivity of $LaNbO_4$ and make this system even more intriguing as a PC-SOFC material.

Through rigorous study of how calcium doping alters and influences microstructure changes in $LaNbO_4$ we have concluded that this dopant does influence the thermophysical properties of this material. The monoclinic to tetragonal transformation was found to increase due to calcium inclusion as is attributed to the creation of oxygen vacancies in the crystal lattice. How these vacancies caused the increase in transformation temperature was not determined in this study. This occurs even though at room temperature each composition is essentially identical with negligible change in the unit cell parameters. The room temperature spontaneous strain for the pure and doped compositions with increasing dopant amount was found to be 6.93%, 6.91%, 6.95%, 6.99% and 6.98% respectively. This spontaneous strain is in agreement with literature values for $LaNbO_4$. As increasing the dopant concentration increased the transformation temperature, no change in transformation mechanism was observed based on the HTXRD datasets and the single step change in specific heat capacity at transformation.

Analysis of the thermal expansion tensor for Ca^{2+} doped $LaNbO_4$ produced new understanding about how this dopant influences the thermal expansion behavior. This was identified as a key area for this study since the change in thermal expansion coefficient between the tetragonal and monoclinic phase leads to difficulty in identifying acceptable interconnect materials. From the linear coefficient of thermal expansion determined from the average of the eigenvalues the key observation was that the 1% doped composition has the least change in linear CTE below the transformation temperature while in the tetragonal phase this same composition has the largest change in linear CTE. As the large change in the CTE between the two phases has been identified as a processing challenge for PC-SOFC devices the extreme change in CTE of 1 mol% Ca^{2+} *t*-$LaNbO_4$ has been identified as a limiting factor in this application. However, the 1.5 mol% doped composition demonstrated more favorable CTE values and further investigation into this composition and even high dopant concentrations should be pursued.

6.2 Effect of Zr^{4+} doping

The $m \rightarrow t$ ferroelastic phase transformation in $LaNbO_4$ was independent of Zr^{4+} dopant concentration. The solubility of Zr^{4+} in $LaNbO_4$ as well as the effect of Zr^{4+} on the phase transformation and thermal expansion properties were studied using high temperature X-ray diffraction and specific heat methods. Unlike the case of $YTaO_4$, an isostructural compound, the Zr^{4+} ion was relatively insoluble in $LaNbO_4$ and a solubility limit of ~5 mol% was determined in this study. The crystal structures of both the *m*- and *t*- $LaNbO_4$ phases were unaffected by the inclusion of Zr^{4+} over the entire temperature range investigated in this work. Consequently, the spontaneous strain in the room temperature *m*-$LaNbO_4$ phase was invariant and determined as 6.93%, 6.99%, 6.92%, 6.91%, 6.92%, and, 6.92% for 0, 1.45, 4.67, 4.87, 5.0, and, 5.06 mol% Zr^{4+} dopant concentrations. Doping with Zr^{4+} had negligible effect on the phase transformation and thermal expansion properties of $LaNbO_4$. Specific heat measurement experiments showed a step change in the specific heat capacity, characteristic of a second order phase transition, within a narrow temperature range (±3°C) for all compositions. Based on careful analysis of the CTE tensor elements and the relative invariance of plane of zero thermal expansion, it was concluded that inclusion of Zr^{4+} in the $LaNbO_4$ structure did not have a significant effect on the thermal expansion properties. The presence of Zr^{4+} was not confirmed in this study, however based on the analysis and the phase diagram it is believed to have been incorporated into the lattice. The ability of the $LaNbO_4$ structure to accommodate dopant ions without any structural rearrangements may be unique to this system and due to the large ionic radius of La^{3+}. Verification of this hypothesis, however, is a subject of another study, and was considered beyond the scope of this investigation.

6.3 Recommendations for further investigations

As a result of the insights and observations made through the study of Ca^{2+} and Zr^{4+} doping of $LaNbO_4$ some recommended areas of future study are:

- As it was possible to determine a plane of zero thermal expansion in the monoclinic phase future efforts could be directed to match the plane with CTE to match the interconnect material. By matching these two CTE advanced processing methods could be employed to produce a layer of material with minimized grain boundaries and the preferred orientation.
- Identify the corresponding plane in the tetragonal phase to the plane of zero thermal expansion in the monoclinic phase and understand what happens to this unique plane after transformation.
- It was observed that $LaNbO_4$ was able to accommodate both Ca^{2+} and Zr^{4+} into the lattice without alteration to the lattice parameters. As this was unexpected it leads to questioning why this is possible. Further investigation should be taken to understand how this is possible and is it a unique phenomenon in $LaNbO_4$ due to the large ionic radius of La^{3+} or is similar behavior observed in the other rare earth orthoniobates.
- It has been reported that 3:1 rare earth niobate materials have similar proton conductivity to the orthoniobates. Due to this, future efforts will be defined to determine the proton conductivity of select 3:1 systems where the crystal structure is either cubic or orthorhombic. In either system the hypothesis is that the increased symmetry will relate to higher conductivity. Additionally, these materials do not experience a phase transformation in the temperature range of interest making them interesting candidates for PC-SOFC application.

- In addition to investigation of the intrinsic conductivity of the 3:1 niobates the effect of acceptor doping should be studied. As the dopant size, type, and concentration has been studied in $LaNbO_4$, similar understanding should be achieved for the 3:1 system with the goal to improve conductivity by an order of magnitude.

REFERENCES

1. E. Mertens and L. Hellinckx, "Mechanism of carbon combustion," *Symposium on Combustion and Flame, and Explosion Phenomena,* 3[1] 474-75 (1948).
2. C. Duan, J. Tong, M. Shang, S. Nikodemski, M. Sanders, S. Ricote, A. Almansoori, and R. O’Hayre, "Readily processed protonic ceramic fuel cells with high performance at low temperatures," *Science* (2015).
3. K. D. Kreuer, "Proton-Conducting Oxides," *Annual Review of Materials Research,* 33[1] 333-59 (2003).
4. N. Yan, X.-Z. Fu, K. T. Chuang, and J.-L. Luo, "Insights into CO poisoning in high performance proton-conducting solid oxide fuel cells," *Journal of Power Sources,* 254[0] 48-54 (2014).
5. T. Yajima, H. Suzuki, T. Yogo, and H. Iwahara, "Protonic Conduction In $SrZrO_3$-Based Oxides," *Solid State Ionics,* 51[1-2] 101-07 (1992).
6. T. Yajima, H. Kazeoka, T. Yogo, and H. Iwahara, "Proton Conduction in Sintered Oxides Based on $CaZrO_3$," *Solid State Ionics,* 47[3-4] 271-75 (1991).

7. H. Iwahara, H. Uchida, K. Ono, and K. Ogaki, "Proton Conduction in Sintered Oxides Based on $BaCeO_3$," *Journal of the Electrochemical Society,* 135[2] 529-33 (1988).

8. H. Iwahara, "Proton conducting ceramics and their applications," *Solid State Ionics,* 86-8 9-15 (1996).

9. H. Iwahara, T. Yajima, T. Hibino, K. Ozaki, and H. Suzuki, "Protonic Conduction In Calcium, Strontium and Barium Zirconates," *Solid State Ionics,* 61[1-3] 65-69 (1993).

10. H. Iwahara, "Oxide-Ionic and Protonic Conductors Based on Perovskite-Type Oxides and Their Possible Applications," *Solid State Ionics,* 52[1-3] 99-104 (1992).

11. H. Iwahara, "High-Temperature Proton Conducting Oxides and Their Applications to Solid Electrolyte Fuel-Cells and Steam Electrolyzer for Hydrogen-Production," *Solid State Ionics,* 28 573-78 (1988).

12. K. Katahira, Y. Kohchi, T. Shimura, and H. Iwahara, "Protonic conduction in Zr-substituted $BaCeO_3$," *Solid State Ionics,* 138[1-2] 91-98 (2000).

13. A. R. Akbarzadeh, I. Kornev, C. Malibert, L. Bellaiche, and J. M. Kiat, "Combined theoretical and experimental study of the low-temperature properties of $BaZrO_3$," *Physical Review B,* 72[20] (2005).

14. P. Babilo and S. M. Haile, "Enhanced sintering of yttrium-doped barium zirconate by addition of ZnO," *Journal of the American Ceramic Society,* 88[9] 2362-68 (2005).

15. K. H. Ryu and S. M. Haile, "Chemical stability and proton conductivity of doped $BaCeO_3$-$BaZrO_3$ solid solutions," *Solid State Ionics,* 125[1-4] 355-67 (1999).

16. A. Bilic and J. D. Gale, "Ground state structure of $BaZrO_3$: A comparative first-principles study," *Physical Review B,* 79[17] (2009).

17. M. E. Bjorketun, P. G. Sundell, and G. Wahnstrom, "Effect of acceptor dopants on the proton mobility in $BaZrO_3$: A density functional investigation," *Physical Review B,* 76[5] (2007).

18. R. Haugsrud and T. Norby, "Proton conduction in rare-earth ortho-niobates and ortho-tantalates," *Nat. Mater.,* 5[3] 193-96 (2006).

19. H. Fjeld, K. Toyoura, R. Haugsrud, and T. Norby, "Proton mobility through a second order phase transition: theoretical and experimental study of $LaNbO_4$," *Physical chemistry chemical physics : PCCP,* 12[35] 10313-9 (2010).

20. K. Hadidi, R. Hancke, T. Norby, A. E. Gunnæs, and O. M. Løvvik, "Atomistic study of $LaNbO_4$; surface properties and hydrogen adsorption," *International Journal of Hydrogen Energy,* 37[8] 6674-85 (2012).

21. M. Huse, A. W. B. Skilbred, M. Karlsson, S. G. Eriksson, T. Norby, R. Haugsrud, and C. S. Knee, "Neutron diffraction study of the monoclinic to tetragonal structural transition in $LaNbO_4$ and its relation to proton mobility," *J. Solid State Chem.,* 187 27-34 (2012).

22. M. Ivanova, S. Ricote, W. A. Meulenberg, R. Haugsrud, and M. Ziegner, "Effects of A- and B-site (co-)acceptor doping on the structure and proton conductivity of $LaNbO_4$," *Solid State Ionics,* 213[0] 45-52 (2012).

23. R. Haugsrud and T. Norby, "High-temperature proton conductivity in acceptor-doped $LaNbO_4$," *Solid State Ionics,* 177[13-14] 1129-35 (2006).

24. L. H. Brixner, J. F. Whitney, F. C. Zumsteg, and G. A. Jones, "Ferroelasticity in the $LnNbO_4$-type rare earth niobates," *Materials Research Bulletin,* 12[1] 17-24 (1977).

25. K. A. Gingerich and H. E. Bair, "Relation between ionic radii and transformation temperature in rare earth niobates," *Advances in X-Ray Analysis,* 7 22-30 (1964).

26. A. I. Komkov, "The structure of natural fergusonite, and of a polymorphic modification," *Kristallografiya,* 4[6] 836-41 (1959).

27. L. L. Kukueva, L. A. Ivanova, and Y. N. Venevtsev, "Ferroelastics with the fergusonite type structure," *Ferroelectrics*, 55[1-4] 797-801 (1983).

28. G. J. McCarthy, "X-ray studies of RE NbO_4 compounds," *Acta Crystallographica, Section B: Structural Science,* 27[11] 2285-86 (1971).

29. H. P. Rooksby and E. A. D. White, "The structures of 1:1 compounds of rare earth oxides with niobia and tantala," *Acta Crystallographica,* 16[9] 888-90 (1963).

30. V. S. Stubican, "High-Temperature Transitions in Rare-Earth Niobates and TantaIates," *Journal of the American Ceramic Society,* 47[2] 55-58 (1964).

31. L. Jian and C. M. Wayman, "Monoclinic-to-tetragonal phase transformation in a ceramic rare-earth orthoniobate, $LaNbO_4$," *J Am Ceram Soc,* 80[3] 803-06 (1997).

32. T. Mokkelbost, H. L. Lein, P. E. Vullum, R. Holmestad, T. Grande, and M.-A. Einarsrud, "Thermal and mechanical properties of $LaNbO_4$-based ceramics," *Ceramics International,* 35[7] 2877-83 (2009).

33. P. Sarin, R. W. Hughes, D. R. Lowry, Z. D. Apostolov, and W. M. Kriven, "High-Temperature Properties and Ferroelastic Phase Transitions in Rare-Earth Niobates ($LnNbO_4$)," *J. Am. Ceram. Soc.,* 97[10] 3307-19 (2014).

34. I. Lifshitz, "Kinetics of ordering during second-order phase transitions," *Sov. Phys. JETP,* 15 939 (1962).

35. W. D. Kingery, H. K. Bowen, and D. R. Uhlmann, "Introduction to ceramics.*"* Wiley, (1976).

36. W. Kriven, M., "Displacive Transformations and their Applications in Structural Ceramics," *J. Phys. IV France,* 05[C8] C8-101-C8-10 (1995).

37. J. W. E. Mariathasan, L. W. Finger, and R. M. Hazen, "High-pressure behavior of $LaNbO_4$," *Acta Crystallographica, Section B: Structural Science,* 41[3] 179-84 (1985).

38. W. I. F. David, "The high-temperature paraelastic structure of $LaNbO_4$," *Materials Research Bulletin,* 18[6] 749-56 (1983).

39. K. Momma and F. Izumi, "VESTA 3 for three-dimensional visualization of crystal, volumetric and morphology data," *Journal of Applied Crystallography,* 44[6] 1272-76 (2011).

40. A. Kuwabara, R. Haugsrud, S. Stolen, and T. Norby, "Local condensation around oxygen vacancies in t-$LaNbO_4$ from first principles calculations," *Physical Chemistry Chemical Physics,* 11[27] 5550-53 (2009).

41. G. C. Mather, C. A. J. Fisher, and M. S. Islam, "Defects, Dopants, and Protons in $LaNbO_4$," *Chemistry of Materials,* 22[21] 5912-17 (2010).

42. T. Norby and A. Magrasó, "On the development of proton ceramic fuel cells based on Ca-doped $LaNbO_4$ as electrolyte," *Journal of Power Sources,* 282[0] 28-33 (2015).

43. N. Kitamura, K. Amezawa, Y. Tomii, N. Yamamoto, and T. Hanada, "Protonic conduction in Sr-doped $(La_{1-x}Sm_x)PO_4$," *Solid State Ionics*, 175[1–4] 563-67 (2004).

44. M. Li, M. Ni, F. Su, and C. Xia, "Proton conducting intermediate-temperature solid oxide fuel cells using new perovskite type cathodes," *Journal of Power Sources,* 260[0] 197-204 (2014).

45. J. R. Tolchard, H. L. Lein, and T. Grande, "Chemical compatibility of proton conducting $LaNbO_4$ electrolyte with potential oxide cathodes," *Journal of the European Ceramic Society*, 29[13] 2823-30 (2009).

46. W. Munch, K. D. Kreuer, S. Adams, G. Seifert, and J. Maier, "The relation between crystal structure and the formation and mobility of protonic charge carriers in perovskite-type oxides: A case study of Y-doped $BaCeO_3$ and $SrCeO_3$," *Phase Transitions,* 68[3] 567-86 (1999).

47. S. Shian, P. Sarin, M. Gurak, M. Baram, W. M. Kriven, and D. R. Clarke, "The tetragonal–monoclinic, ferroelastic transformation in yttrium tantalate and effect of zirconia alloying," *Acta Materialia,* 69[0] 196-202 (2014).

48. R. Haugsrud and T. Risberg, "Protons in Acceptor-Doped La_3NbO_7 and La_3TaO_7," *Journal of The Electrochemical Society*, 156[4] B425-B28 (2009).

49. A. M. George and A. N. Virkar, "Mixed iono-electronic conduction in β-$LaNb_3O_9$," *Journal of Physics and Chemistry of Solids*, 49[7] 743-51 (1988).

50. E. P. Savchenko, N. A. Godina, and E. K. Keler, "Solid-Phase Reactions Between Pentoxides of Niobium and Tantalum and Oxides of the Rare-Earth Elements," *Chemistry of High-Temperature Materials* (1969).

51. T. Mokkelbost, H. L. Lein, P. E. Vullum, R. Holmestad, T. Grande, and M. A. Einarsrud, "Thermal and mechanical properties of $LaNbO_4$-based ceramics," *Ceram Int,* 35[7] 2877-83 (2009).

52. A. W. B. Skilbred and R. Haugsrud, "Sandvik Sanergy HT – A potential interconnect material for $LaNbO_4$-based proton ceramic fuel cells," *Journal of Power Sources,* 206 70-76 (2012).

53. M. H. Nguyen, S.-J. Lee, and W. M. Kriven, "Synthesis of oxide powders by way of a polymeric steric entrapment precursor route," *Journal of Materials Research,* 14[08] 3417-26 (1999).

54. P. Sarin, W. Yoon, K. Jurkschat, P. Zschack, and W. M. Kriven, "Quadrupole lamp furnace for high temperature (up to 2050 K) synchrotron powder x-ray diffraction studies in air in reflection geometry," *Review of Scientific Instruments,* 77[9] 093906-06-9 (2006).

55. H. Rietveld, "A profile refinement method for nuclear and magnetic structures," *Journal of Applied Crystallography,* 2[2] 65-71 (1969).

56. A. C. Larson and R. B. Von Dreele, "General Structure Analysis System (GSAS)," *Los Alamos National Laboratory Report LAUR* 86-748 (2000).

57. B. H. Toby, "EXPGUI, a graphical user interface for GSAS," *Journal of Applied Crystallography,* 34 210-13 (2001).

58. Y. S. K. Touloukian, R K ; Taylor, R E ; Desai, P D, " Thermal Expansion Metallic Elements and Alloys." in Thermophysical Properties of Matter - the TPRC Data Series. , Vol. 12**.** 1975.

59. K. Aizu, "Determination of the State Parameters and Formulation of Spontaneous Strain for Ferroelastics," *Journal of the Physical Society of Japan,* 28[3] 706-16 (1970).

60. J. L. Schlenker, G. V. Gibbs, and M. B. Boisen, Jnr, "Strain-tensor components expressed in terms of lattice parameters," *Acta Crystallographica Section A,* 34[1] 52-54 (1978).

61. E. K. H. Salje, "Phase Transitions in Ferroelastic and Co-elastic Crystals." Cambridge University Press, (1991).

62. Z. A. Jones, P. Sarin, R. P. Haggerty, and W. M. Kriven, "CTEAS: a graphical-user-interface-based program to determine thermal expansion from high-temperature X-ray diffraction," *Journal of Applied Crystallography,* 46[2] 550-53 (2013).

63. R. E. Newnham, "Properties of Materials : Anisotropy, Symmetry, Structure: Anisotropy, Symmetry, Structure." OUP Oxford, (2004).

64. B. D. Cullity, "Elements of X-ray diffraction." Addison-Wesley Pub. Co.: Reading, Mass., (1956).

65. D. Weigel, T. Beguemsi, P. Garnier, and J. F. Berar, "Evolution des tenseurs de dilatation thermique en fonction de la temperature. I. Loi generale d'evolution de la symetrie du tenseur," *Journal of Solid State Chemistry,* 23[3-4] 241-51 (1978).

66. D. E. Sands, "Vectors and Tensors in Crystallography." Dover, (2002).

67. R. C. Garvie, "The Occurrence of Metastable Tetragonal Zirconia as a Crystallite Size Effect," *The Journal of Physical Chemistry,* 69[4] 1238-43 (1965).

68. R. C. Garvie, "Stabilization of the tetragonal structure in zirconia microcrystals," *The Journal of Physical Chemistry,* 82[2] 218-24 (1978).

69. N. A. Pertsev and E. K. H. Salje, "Thermodynamics of pseudoproper and improper ferroelastic inclusions and polycrystals: Effect of elastic clamping on phase transitions," *Physical Review B,* 61[2] 902-08 (2000).

70. T. Chraska, A. H. King, and C. C. Berndt, "On the size-dependent phase transformation in nanoparticulate zirconia," *Materials Science and Engineering: A*, 286[1] 169-78 (2000).

71. L. H. Brixner and H. y. Chen, "On the Structural and Luminescent Properties of the M′ LnTaO4 Rare Earth Tantalates," *Journal of The Electrochemical Society,* 130[12] 2435-43 (1983).

72. R. D. Shannon, "Revised effective ionic radii and systematic studies of interatomic distances in halides and chalcogenides," *Acta Crystallographica, Section A: Foundations of Crystallography,* 32[5] 751-67 (1976).

73. A. Mielewczyk-Gryn, K. Gdula-Kasica, B. Kusz, and M. Gazda, "High temperature monoclinic-to-tetragonal phase transition in magnesium doped lanthanum ortho-niobate," *Ceramics International,* 39[4] 4239-44 (2013).

74. K. A. Gingerich and H. E. Bair, "Relation between ionic radii and transformation temperature in rare earth niobates," *Adv. X-Ray Anal.*, 7 22-30 (1964).

75. P. Sarin, R. P. Haggerty, W. Yoon, M. Knapp, A. Berghaeuser, P. Zschack, E. Karapetrova, N. Yang, and W. M. Kriven, "A curved image-plate detector system for high-resolution synchrotron X-ray diffraction," *Journal of Synchrotron Radiation*, 16[2] 273-82 (2009).

76. C. G. Zheng and A. R. West, *Br. Ceram. Trans. J.,* 89[4] 138-41 (1990).

77. R. D. Shannon, "Revised effective ionic radii and systematic studies of interatomic distances in halides and chalcogenides," *Acta Crystallographica Section A: Crystal Physics, Diffraction, Theoretical and General Crystallography*, 32[5] 751-67 (1976).

78. D. J. Green, R. H. Hannink, and M. V. Swain, "Transformation toughening of ceramics," (1989).

VITA

Daniel Robert Lowry

Candidate for the Degree of

Master of Science

Thesis: EFFECTS OF Ca^{2+} AND Zr^{4+} DOPING ON THE THERMOPHYSICAL PROPERTIES OF $LaNbO_4$

Major Field: Materials Science and Engineering

Biographical

Education:

Completed the requirements for the Master of Science/Arts in your major at Oklahoma State University, Stillwater, Oklahoma in December, 2015.

Completed the requirements for the Bachelor of Science in Materials Science and Engineering at The University of Illinois Urbana-Champaign, Urbana, IL, USA in 2009.

Experience:
Research Assistant, Oklahoma State University, Tulsa, OK (2013-2015)
Chemist I, Sigma-Aldrich, Urbana, IL (2011-2013)
Research Assistant, University of Illinois, Urbana, IL (2008-2011)
Teaching Assistant, University of Illinois, Urbana, IL (2010-2011)

Professional Memberships:
Phi Kappa Phi honorary society
Material Advantage